Copyright Undertaking

ENERGIZING FUEL CELLS WITH AN ELECTRICALLY RECHARGEABLE LIQUID FUEL

SHI XINGYI

PhD

The Hong Kong Polytechnic University

2022

The Hong Kong Polytechnic University

Department of Mechanical Engineering

Energizing fuel cells with an electrically rechargeable liquid fuel

Shi Xingyi

A thesis submitted in partial fulfilment of the requirements for the degree of Doctor of Philosophy

May 2022

CERTIFICATE OF ORIGINALITY

I hereby declare that this thesis is my own work and that, to the best of my knowledge and belief, it reproduces no material previously published or written, nor material that has been accepted for the award of any other degree or diploma, except where due acknowledgement has been made in the text.

Xingyi SHI

Acknowledgements

The last four years I spent at the Hong Kong Polytechnic University is a true treasure to me. I would like to first express my thankfulness to all who have helped and taught me during my study.

I'm extremely grateful to my chief supervisor, Prof. Liang An, as without the support and nurturing from him the completion of my thesis would not have been possible. I'm very grateful to him for showing me this exciting and challenging fuel cell field. His patience, enthusiasm, and continuous support helped me throughout my whole study period. It was with his tireless teachings aid me to gain a comprehensive understanding of my work, his strict requirements built me with a good manner, his novel ideas enlightened me with a broad vision. I would like to extend my sincere thanks to my co-supervisor Prof. Haihui Ruan, who has helped me a lot during my study at PolyU. I'm also deeply indebted to Prof. Tianshou Zhao (Department of Mechanical and Aerospace Engineering, HKUST), who has greatly helped to improve the quality of my work. Special thanks go to Prof. Zhengtang LUO (Department of Chemical and Biological Engineering, HKUST) and Prof. Jiyun ZHAO (Department of Mechanical Engineering, CityU) for reviewing my thesis and serving as a member of my thesis examination committee.

Thanks should also be expressed to technical supporting and administrative staff, i.e., Mr. LEUNG Chi-kuen, for their unparalleled help during my study. I’d also like to extend my gratitude to all the group members from the An’s research group for their continuous help, and unwavering support. They are Prof. Bin HUANG, Prof. Yaoguang YU, Dr. Zhefei PAN, Dr. Xiangyu SU, Dr. Guangzhe LI, Dr. He LIN, Mr. Oladapo Christopher ESAN, Miss. Xiaoyu HUO, Mr. Yun LIU, and all the students worked in our lab. Especially, I very much appreciate Mr. Oladapo Christopher ESAN and Miss. Xiaoyu HUO for their great help and efforts on improving the quality of my work.

Finally, I cannot begin to convey my gratitude to my families, and my girlfriend, Miss. Yining Ma, for their unwavering support and unconditional love. I wish them health and happiness in the future and it is their support encourage me to get through all the hard times.

In summary, I wish everyone who have helped me a joyful life in the future.

Abstract

Direct liquid fuel cells, attributed to their high energy density and ease of fuel handling, have been regarded as a promising technology for power generation and thus attracted world-wide attentions in the last decades. However, due to the sluggish reaction kinetics of the conventional liquid fuels even with the use of noble metal catalysts, the commercialization progress of the direct liquid fuel cells is still being greatly hampered. To address this issue, a novel system using an electrically rechargeable liquid fuel (e-fuel) for energy storage and power generation has been recently proposed and demonstrated. The liquid e-fuel is stated to be attainable from diverse kinds of materials such as inorganic materials, organic materials, and suspensions of particles. Furthermore, it is reported that, in comparison to conventional alcoholic liquid fuels, the liquid e-fuel possesses a lot of advantages such as: i) superior reactivity even on carbon-based materials, which thereby eliminates the usage of any noble metal catalysts; ii) low freezing point, which hence allows the operation of the cell at wide temperature range; and iii) rechargeability, which therefore enables the e-fuel to be used for more than 100 cycles, greatly reducing the fuel production cost. Hence, attracted by the superiorities of the e-fuel, the objective of this thesis is aimed at examining the performance of a direct liquid fuel cell using an e-fuel containing vanadium ions through experimental and numerical approaches. To begin with, an active liquid e-

fuel cell was developed to experimentally study the effects of various structural parameters and operating conditions on the cell performance. It is found that the direct liquid fuel cell using e-fuel demonstrated an impressive performance with an open-circuit voltage of 1.15 V, a maximum current density of 1980 mA cm^{-2}, a peak power density of 857.0 mW cm^{-2} and an energy efficiency of 41.6 %. Secondly, to enable the application of this liquid fuel cell in mobile devices, a passive fuel cell using the e-fuel, free from any auxiliary equipment, is designed and fabricated. The passive cell was refuelled 25 times and achieved a stable operation for over 350 hours, presenting its capability for long-term operation. Furthermore, using a transparent cell, a side reaction, found at the anode side of cell, was also examined and proved to be hydrogen evolution reaction. Thirdly, to demonstrate the wide applicability of the e-fuel under diverse kinds of environment, an all-climate liquid fuel cell is designed, fabricated, and tested, which demonstrated the operation capability of the liquid e-fuel under sub-zero environment. Fourthly, apart from the experimental works, a numerical study is also carried out to provide a deep understanding to the complex physical and chemical processes within this passive fuel cell. Lastly, to present the capability of this fuel cell for large-scale application, a liquid fuel cell stack is designed, fabricated, and studied, which is also demonstrated to be capable of powering a toy car stably and thus justifies its great potential for achieving commercial applications in the future.

Table of Contents

List of Figures

List of Tables

Abbreviations

BEV	Battery electric vehicle
CC	Current collector
CCL	Cathode catalyst layer
CDL	Cathode diffusion layer
CV	Cyclic voltammetry
DEFC	Direct ethanol fuel cell
DFAFC	Direct formic acid fuel cell
DLFC	Direct liquid fuel cell
DMFC	Direct methanol fuel cell
EE	Energy efficiency
E-fuel	Electrically rechargeable liquid fuel
EIS	Electrochemical impedance spectroscopy
FCEV	Fuel cell electric vehicle
FE	Faradic efficiency
HER	Hydrogen evolution reaction
IEM	Ion exchange membrane
MEA	Membrane electrode assembly
OCV	Open-circuit voltage
OR	Open ratio
ORR	Oxygen reduction reaction
PEMFC	Proton exchange membrane fuel cell

PID	Proportional-integral-derivative
PTFE	Polytetrafluoroethylene
SCCM	Standard cubic centimetre per minute
SCE	Saturated calomel electrode
SEM	Scanning electron microscope
VE	Voltage efficiency
XRD	X-ray diffraction

Nomenclature

List of Symbols

a_v	Specific area, m^{-1}
C	Species concentration, mol m^{-3}
D	Diffusion coefficient, m^2 s^{-1}
E	Potential/voltage, V
E^0	Equilibrium potential, V
F	Faradic constant, A s mol^{-1}
G	Cell constant
h	Cell height, m
i	Current density
i_0	Reference exchange current density, A m^{-2}
k	Reaction rate constant, m s^{-1}
$\vec{N}$	Flux, mol m^{-2} s^{-1}
n	Number of participating electrons
$\vec{n}$	Normal vector
R	Universal gas constant, J mol^{-1} K^{-1}
S	Source term
T	Operating temperature, K
t	Time, s
u	Mobility, mol s kg^{-1}

V	Volume, L
v	Stoichiometric coefficient
w	Cell width, m
z	Valence of ion

Greek

α	Charge transfer coefficient
γ	Reaction order
δ	Thickness, m
ε	Porosity
ξ	Voltage efficiency, %
η	Faradic efficiency, %
σ	Conductivity, S m^{-1}
$\emptyset$	Potential, V
φ	Energy efficiency, %

Superscripts

0	Initial
ccl	Cathode catalyst layer
eff	Effective
ref	Reference

Subscripts

a	Anode
aver	Average
c	Cathode
e	E-fuel
ccl	Cathode catalyst layer
cdl	Catalyst diffusion layer
$\mathbf{H^+}$	Proton
i	Species
init	Initial
KCl	Potassium chloride
l	liquid
m	Membrane
O_2	Oxygen
s	Solid
theo	Theoretical
SO_4^{2-}	Sulphate ion
$\mathbf{V^{2+}}$	Vanadium (II) ion
$\mathbf{V^{3+}}$	Vanadium (III) ion

Chapter 1 Introduction

1.1 Background

To date, with the advancement of technology and the rapid development of human society, the fast growth of energy consumption has drawn more and more attention across the globe. According to the World Energy Statistical Review, the global energy demand has been growing continuously at an annual growth rate of around 3% during the past decades. [1] Therefore, more and more efforts have been dedicated to the realization of stable and sustainable power supply world-wide. At present, the energy supply around the world majorly relies on the usage of fossil fuels including petroleum, coal, and natural gas. [2] It has been reported that, in 2018, over 70% of the global energy demand depended on oil, natural gas and coal. However, the large-scale utilization of conventional fossil fuels has caused many problems and resulted in increasing concerns. On the one hand, the overexploitation of the fossil fuel resources accelerated their depletion, which is expected that if the consumption rate of fossil fuels keeps rising, the storage of current natural gas and coal is expected to be exhausted by 2060. [3] On the other hand, the usage of fossil fuels, which is the major origin source of global greenhouse gases, has led to an unignorable negative impact on the ecological environment and further triggered climate problems all over the world. [4] Therefore, it is an imperative task to reduce the utilization of fossil fuels so that the emissions of carbon dioxide can be reduced, and the resource shortages can be prevented.

To this end, more and more efforts have been made on the development of novel power generation systems so as to produce energy in a clean, efficient and environmental-friendly way and thereby achieve the sustainable development. Among all types of the power generation systems, the fuel cell is considered to be one of the most promising technologies and has received great interest.

1.2 Fuel cells

The fuel cell generates power by directly converting the chemical energy stored in the fuels into electricity via the electrochemical reactions. To date, a wide range of fuel cell systems using different types of fuels has been developed, such as the hydrogen-oxygen fuel cells, and direct liquid fuel cells. [5,6] Out of all types of fuel cells, the hydrogen-oxygen fuel cells are the most well-studied fuel cell technology, which attracted great attentions over the years. [7] The major advantages of hydrogen-oxygen fuel cells include high power density, low emissions, high efficiency, silent operation and low cost, all of which thereby make them the potential power generation system for future applications. However, the major limitations for hydrogen-oxygen fuel cells arise from the intrinsic nature of the gaseous hydrogen used. [8] Due to its low flammability limit, hydrogen is highly explosive even at room temperature, making it dangerous for numerous applications in daily life. Such potential risk thereby leads to strict safety standards for the storage, transportation, and production of large amounts of hydrogen gas, which consequently results in high technical requirements and costs. Therefore, the widespread commercialization of hydrogen-oxygen fuel cells is still being greatly hindered. To this end, in an attempt to enable the ease of fuel handling, the direct liquid fuel cells using liquid fuels have been extensively studied in the past decades. [9]

1.3 Direct liquid fuel cells

1.3.1 Features

Utilizing the liquid fuels, the direct liquid fuel cell (DLFC) has received ever-increasing attention world-wide. The conventional direct liquid fuel cell is typically fed with alcoholic liquid fuels such as ethanol and methanol, which thereby greatly eased the fuel handling, storage, and transportation in comparison to the gaseous hydrogen, making it to be a candidate with great potential for commercialization. [10] However, due to the poor reaction kinetics of liquid fuels, the DLFC is still not able to provide satisfactory power density and energy efficiency. Furthermore, the performance of DLFC also shows strong temperature dependence, which thereby greatly impeded the further improvement of its system efficiency as it always requires auxiliary heating system to boost its performance while resulting in undesired extra energy loss.

1.3.2 Research and development

In the recent decades, considerable research efforts have been made on the development of DLFCs. Up till now, various types of liquid fuels such as methanol, ethanol, formic acid, dimethyl ether and sodium borohydride have been used and studied for their application in the DLFCs. To begin with, the earliest type of DLFC, the direct methanol fuel cells (DMFCs) have been most intensively studied due to the relatively high electrochemical activity of methanol. For example, Baronia *et al.* developed an active DMFC, which achieved a peak power density of 118.4 mW cm^{-2} at 100 ˚C with the PtCo/rGO being used as anode. [11] In another work, Zou *et al.* used the unsupported Pt-Ru catalyst for passive DMFC and demonstrated a peak power density of 47.18 mW cm^{-2}. [12] Moreover, to alleviate the methanol crossover problem, Yang *et al.* synthesized a composite Nafion®/SBA-15 membrane for DMFC and achieved a power density of 117 mW cm^{-2} at 60˚C, which is 80 % higher than the cell using recast Nafion while is 23 % higher than that with commercial Nafion 117. [13]

While exhibiting superior performance, the methanol with its toxic nature restricted the practical applications of DMFCs. Ethanol, as an alternative, therefore, has attracted much attention due to its safety and higher energy density. [6] Furthermore, the ethanol is a promising renewable fuel source which can be obtained from biomass fermentation process. However, due to the strong C-C bond inside the ethanol structure, its reaction kinetics is relatively sluggish, therefore leading to a low cell voltage and efficiencies. To address this issue, previous works have tried to increase the operating temperature for the direct ethanol fuel cells (DEFCs). Kumar Choudhary *et al.* analyzed the effects of the operating temperature on the DEFC and found that the cell performance is able to be enhanced from 9.15 to 16.23 mW cm^{-2} as the temperature raised from 40 to 80 ˚C. [14] However, on the other hand, the elevated temperature not only may trigger the membrane dehydration issue, but also can result in reduced system efficiency. Thus, using another strategy, Yoon. *et al.* have fabricated a novel nanosized GaPtMnP alloy anchored on N-doped multiwall carbon nanotubes anodic catalyst to enhance the reaction kinetics, through which the cell is found to achieve a peak power density of 86.64 mW cm^{-2} at 70 ˚C. [15] However, up till now, even though tremendous efforts have been made on the performance advancement of DEFCs, the current performances of DEFCs are still far from the requirement for large-scale application.

Another promising alternative, formic acid, has also been widely studied due to its low toxicity. Compared with methanol, the formic acid exhibits advantages including non-flammability, obtainability and less crossover issue. [10,16] However, it also possesses many disadvantages such as the high market price and low volumetric energy density. Furthermore, the oxidation of formic acid may form undesired CO intermediate, which may poison the cathode catalyst and thereby deteriorate the cell efficiency and durability. [17] To address this issue, Yang *et al.* synthesized a heat-treated Pd-based bimetallic anodic catalyst, which is found to greatly improve the resistance to CO poisoning and thereby allows the cell to achieve a maximum power density of 137 mW cm^{-2}. [18] Nevertheless, currently, the durability of direct formic acid fuel cells (DFAFCs) is still limited by the deactivation of Pd-based catalyst especially under high formic acid concentration, which therefore makes the development of cheap and stable catalysts still in an urgent need. [19]

In summary, up till now, though lots of efforts have been made on the development DLFCs, their performances are still far from expectation, which thus greatly restricted their commercialization progress. The major challenges arouse from the sluggish liquid fuel oxidization reaction kinetics, the high costs and scarcity of noble metals catalyst, as well as the poor long-term stability and durability. Therefore, the screening of novel liquid fuels with cost-effectiveness and superior reactivity is an essential requirement to boost the performance of the DLFC and further realize its future practical applications.

1.3.3 Electrically rechargeable liquid fuel (E-fuel)

Recently, a novel fuel named the electrically rechargeable liquid fuel (e-fuel) has been proposed and attracted increasing attention worldwide. Radically different from the liquid alcohol fuels utilized by the conventional liquid fuel cellls such as methanol and ethanol, the liquid e-fuel owns a lot of advantages. [20] Firstly, it possesses wide material selectivity, as it can be made of various electroactive species including inorganic materials (*e.g.,* metal ions), organic materials (*e.g.,* alloxazines) and suspension of particles (*e.g.,* polysulphide-based nanofluid). Secondly, this liquid e-fuel is electrically rechargeable, where it can be recycled and then recharged using an e-fuel charger through a simple electrochemical reaction and thus greatly reducing the e-fuel production cost. Thirdly, this liquid e-fuel is found to exhibit good electrochemical reactivity even on carbon-based materials, which thereby not only could eliminate the usage of noble metal catalyst during the fuel cell fabrication and significantly reduce the cell manufacture cost, but also could dramatically improve the fuel cell durability. In addition, compared to the conventional liquid fuels such as ethanol that contain strong carbon-carbon bonds in their chemical structures, the e-fuel with rapid reaction kinetics is believed could considerably boost the power density and energy efficiency of the fuel cell.

Inspired by the superiorities of the liquid e-fuel, a direct liquid fuel cell fed with the e-fuel containing vanadium ions as fuel and oxygen/air as oxidant is proposed and developed. The advantages of using this vanadium-based e-fuel have mainly three folds: i) it allows a low cell fabrication cost as it can be used without any catalysts; ii) it ensures a low fuel fabrication cost as it is electrically rechargeable; and iii) it can be charged through a mature technology named all-vanadium redox flow battery. Furthermore, by utilizing the novel e-fuel, this liquid fuel cell is still allowed to be capable of altering its storage capacity and output power independently. Its storage capacity is controlled via changing the e-fuel volume and concentration, while its output power can be adjusted by altering the electrode size so as to meet the application requirement. Moreover, this liquid fuel cell can also be refueled by simply replacing the exhausted e-fuel with the fresh/recharged liquid e-fuel just as the conventional alcoholic liquid fuel cells, which therefore can enable almost indefinite consistent operation. With the above-mentioned advantages, it is thus believed the novel e-fuel to be a promising alternative fuel and could at last enable the liquid fuel cell to be a promising power generation system for future practical applications.

1.3.4 Working principle

The structure of the fuel cell utilizing liquid e-fuel is depicted in Figure 1.1. Similar to the conventional liquid fuel cells, it contains a membrane electrode assembly (MEA), which is comprised of a catalyst-free graphite-felt anode, a conventional oxygen cathode, and a proton exchange membrane. The MEA is clamped by a pair of graphite flow fields engraved with a serpentine flow field, a pair of current collectors and a pair of endplates. In addition, the fuel cell system also includes a peristaltic pump for the e-fuel delivery, a gas cylinder and mass flow meter to control the oxidant delivery and other external accessories.

During the operation of this liquid fuel cell, the oxygen is supplied to the cathode side to meet the protons and electrons and then produce water following the equation as shown below:

$$O_2 + 4H^+ + 4e^- \leftrightarrow 2H_2O \qquad E^0 = +\,1.23V \qquad (1)$$

In the meanwhile, at the anode side, the liquid e-fuel containing vanadium ions is delivered into the cell, where the V^{2+} ions are oxidized to V^{3+} ions and the electrons released are then transported to the cathode through the external circuit:

$$4V^{2+} \leftrightarrow 4V^{3+} + 4e^- \qquad E^0 = -\,0.26V \qquad (2)$$

Inside the cell, the protons are transported from the anode to the cathode side through the proton exchange membrane to balance the charge, where the overall reaction can therefore be described as follows: [21]

$$4V^{2+} + O_2 + 4H^+ \leftrightarrow 4V^{3+} + 2H_2O \qquad \Delta E^0 = 1.49V \qquad (3)$$

Compared to the conventional liquid fuel cells utilizing alcohol liquid fuels, such as ethanol (1.14 V), methanol (1.21 V) and ethylene glycol (1.09 V), this liquid e-fuel is able to provide a theoretical voltage as high as 1.49 V, therefore making it a more promising candidate for real application.

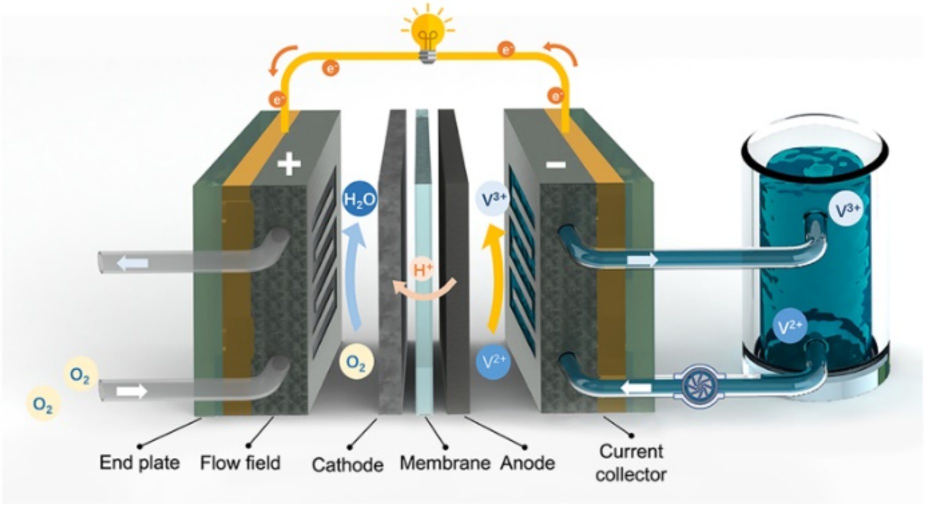

Figure 1.1 Working principle of a direct liquid fuel cell fed with the e-fuel.

1.3.5 State-of-the-art performance

As discussed in section 1.3.2, to date, various kinds of liquid fuels have been used for powering the DLFCs. However, though lots of efforts have been made on improving the cell performance, they are still far from the commercialization requirement. For example, as the most common type of DLFCs, the current DMFCs can only achieve a peak power density of around 100~180 mW cm^{-2} under an operating temperature of 60~100˚C. While in most cases, the DEFCs, as for another type of DLFCs, can only reach a peak power density lower than 50 mW cm^{-2} under room temperature. The DFAFCs, in contrast, can deliver a peak power density of 30 to 200 mW cm^{-2} at the room temperature depending on the different cell configurations. The reasons for the performance differences demonstrated between the DLFCs using various liquid fuels mainly include: i) different reaction kinetics of the liquid fuels used; ii) different cell configurations; and iii) different catalysts and membrane used during cell assembly.

1.3.6 Remaining challenges and issues

Despite the fact that the DLFCs have made tremendous progress, they still face some obstacles and challenges. Firstly, the conventional liquid fuels such as methanol and ethanol can only be used once, which therefore greatly increased the fuel fabrication cost. Secondly, due to the sluggish reaction kinetics of the current liquid fuels, the usage of expensive noble metal catalysts is unavoidable, which thereby results in both high cell fabrication cost and limited cell performance. In addition, to enable a better performance, the conventional DLFC systems always require a high operating temperature, which therefore leads to both increased system complexity and degraded system efficiency. Therefore, it is of significant importance to identify a novel liquid fuel to resolve these problems and develop a powerful, efficient, cost-effective and durable direct liquid fuel cell system.

1.4 Objectives of this thesis

The primary objective of this thesis is to develop a direct liquid fuel cell employing the novel liquid e-fuel containing vanadium ions and oxygen/air as reactants and study the system performance through experimental and numerical approaches. Firstly, an active liquid fuel cell utilizing peristaltic pump for e-fuel delivery is designed and fabricated with extensive studies carried out to comprehensively examine its power generation potential under different operating parameters. To demonstrate the superior reactivity of the proposed liquid e-fuel, the reaction kinetics of liquid e-fuel oxidation reaction on the carbon-based electrode without any noble metal catalyst is first examined. Meanwhile, a comprehensive performance characteristic of this fuel cell on the effects of catalyst loading, membrane thickness, and operating temperature are also conducted so as to attain the best system performance. With a higher cathode catalyst loading, the sluggish reaction kinetics of oxygen reduction reaction is found to be greatly enhanced and enabled the cell to achieve an unprecedented peak power density of over 800 mW cm^{-2} at 60 °C. Secondly, in order to enable the application of the proposed liquid fuel cell in portable electronic devices such as mobile phones and laptops, a passive liquid fuel cell using diffusion and natural convection for fuel delivery without any auxiliary equipment is designed and fabricated. The effects of current collector designs and e-fuel compositions on the mass transport behavior and further the cell performances are studied. Moreover, the long-term operation behavior of the passive fuel cell is also investigated. Eventually, a passive fuel cell with a peak power density of 116.2 mW cm^{-2} and capable of operating stably for over 350 hours is demonstrated, which therefore revealed its great prospect for future applications. In addition, the hydrogen evolution, which is an unexpected side-reaction in the fuel cell, is also identified, studied, and visualized using a transparent fuel cell. Thereafter, to enable the application of the designed liquid fuel cell under all-climate conditions especially under sub-zero environment, the fuel cell performance at -20 to 20 °C is examined. By optimizing the operation parameters, the cell is demonstrated to be capable of running stably at -20 °C without any internal or external heating systems. Using the liquid e-fuel, the fuel cell is found to achieve a peak power density of 76.8 mW cm^{-2} and an energy efficiency of 25.2% at 30 mA cm^{-2} at -20 °C, outperforming all the conventional direct liquid alcohol fuel cells operating under sub-zero environment and even at room temperatures. Such a superior performance as a result of the fast reaction kinetics of liquid e-fuel and its low freezing point makes this developed liquid fuel cell to be a hopeful candidate with wide applicability under all-climate conditions. Fourthly, to gain an in-depth understanding of the underlying mechanisms of this direct liquid fuel cell using e-fuel and provide more insights for its future performance advancement, a transient model is developed. The numerical data shows a superior agreement with experimental results, which not only demonstrates its accuracy but also helps to analyze the concentration distribution of reactive species within the cell, showing the limited mass transport of e-fuel to be the major reason restricting the cell performance. In addition, various structural parameters such as the anode thickness, anode porosity, and CCL thickness are also studied, where their increment are all found to improve the cell performance.

Meanwhile, the effect of oxygen concentration is also examined, where the usage of oxidant with a higher oxygen concentration is found to be able of achieving a higher cell voltage while the predominant reason limiting the operational current density range is found to be arising from the anode side due to the slow e-fuel transport. Furthermore, the anodic and cathodic exchange current densities are also demonstrated to influence the cell performance due to the significant roles of electrodes catalytic reactivity in influencing the anode and cathode overpotential. Finally, during the operation of the fuel cell, it is found that, the water generated at the cathode following the oxygen reduction reaction could lead to water flooding problem and further limit the cell performance. To address this issue, in this work, by manipulating the cathode composition, a blended binder cathode using both Nafion and polytetrafluoroethylene (PTFE) as binding agents is fabricated and studied. The effects of the cathode composition on its water removal ability are examined using a transparent flow field, while the influences on the cell performance are also analyzed. Utilizing the optimized blended binder cathode, a fuel cell stack is designed and fabricated, which is demonstrated to be capable of powering a 3D-printed toy car running stably showing great potential for achieving future commercial applications.

1.5 References

1. K. R. Abbasi, M. Shahbaz, J. Zhang, M. Irfan and K. Lv, Analyze the environmental sustainability factors of China: The role of fossil fuel energy and renewable energy, Renewable Energy, 2022.

2. A. Pareek, R. Dom, J. Gupta, J. Chandran, V. Adepu and P. H. Borse, Insights into renewable hydrogen energy: Recent advances and prospects, Materials Science for Energy Technologies, 2020, 3, 319-327.

3. J. Howarth, When will fossil fuels run out?, https://octopus.energy/blog/when-will-fossil-fuels-run-out/, (accessed May 7th, 2022).

4. A. K. Karmaker, M. M. Rahman, M. A. Hossain and M. R. Ahmed, Exploration and corrective measures of greenhouse gas emission from fossil fuel power stations for Bangladesh, Journal of Cleaner Production, 2020, 244, 118645.

5. S. Mekhilef, R. Saidur and A. Safari, Comparative study of different fuel cell technologies, Renewable and Sustainable Energy Reviews, 2012, 16, 981-989.

6. S. Giddey, S. Badwal, A. Kulkarni and C. Munnings, A comprehensive review of direct carbon fuel cell technology, Progress in Energy and Combustion Science, 2012, 38, 360-399.

7. J. Zhang, Z. Xie, J. Zhang, Y. Tang, C. Song, T. Navessin, Z. Shi, D. Song, H. Wang and D. P. Wilkinson, High temperature PEM fuel cells,

Journal of power Sources, 2006, 160, 872-891.

8. M. E. Scofield, H. Liu and S. S. Wong, A concise guide to sustainable PEMFCs: recent advances in improving both oxygen reduction catalysts and proton exchange membranes, Chemical Society Reviews, 2015, 44, 5836-5860.

9. W. Huang, H. Wang, J. Zhou, J. Wang, P. N. Duchesne, D. Muir, P. Zhang, N. Han, F. Zhao and M. Zeng, Highly active and durable methanol oxidation electrocatalyst based on the synergy of platinum–nickel hydroxide–graphene, Nature communications, 2015, 6, 1-8.

10. N. Shaari, S. K. Kamarudin, R. Bahru, S. H. Osman and N. A. I. Md Ishak, Progress and challenges: Review for direct liquid fuel cell, International Journal of Energy Research, 2021, 45, 6644-6688.

11. R. Baronia, J. Goel, S. Tiwari, P. Singh, D. Singh, S. P. Singh and S. Singhal, Efficient electro-oxidation of methanol using PtCo nanocatalysts supported reduced graphene oxide matrix as anode for DMFC, International Journal of Hydrogen Energy, 2017, 42, 10238-10247.

12. L. Zou, J. Guo, J. Liu, Z. Zou, D. L. Akins and H. Yang, Highly alloyed PtRu black electrocatalysts for methanol oxidation prepared using magnesia nanoparticles as sacrificial templates, Journal of Power Sources, 2014, 248, 356-362.

13. C.-W. Yang, C.-C. Chen, K.-H. Chen and S. Cheng, Effect of pore-directing agents in SBA-15 nanoparticles on the performance of

Nafion®/SBA-15n composite membranes for DMFC, Journal of Membrane Science, 2017, 526, 106-117.

14. A. K. Choudhary and H. Pramanik, Enhancement of ethanol electrooxidation in half cell and single direct ethanol fuel cell (DEFC) using post-treated polyol synthesized Pt-Ru nano electrocatalysts supported on HNO3-functionalized acetylene black carbon, International Journal of Hydrogen Energy, 2020, 45, 574-594.

15. Y. S. Yoon, P. Basumatary, M. E. Kilic, Y. L. Cha, K. R. Lee, D. J. Kim and D. Konwar, Novel GaPtMnP Alloy Based Anodic Electrocatalyst with Excellent Catalytic Features for Direct Ethanol Fuel Cells, Advanced Functional Materials, 2022, 2111272.

16. S. K. Suraparaju, S. K. Natarajan and P. Karthikeyan, 2019.

17. B. Ong, S. Kamarudin and S. Basri, Direct liquid fuel cells: A review, International journal of hydrogen energy, 2017, 42, 10142-10157.

18. S. Yang, Y. Chung, K.-S. Lee and Y. Kwon, Enhancements in catalytic activity and duration of PdFe bimetallic catalysts and their use in direct formic acid fuel cells, Journal of Industrial and Engineering Chemistry, 2020, 90, 351-357.

19. X. Yu and P. G. Pickup, Recent advances in direct formic acid fuel cells (DFAFC), Journal of Power Sources, 2008, 182, 124-132.

20. H. Jiang, L. Wei, X. Fan, J. Xu, W. Shyy and T. Zhao, A novel energy storage system incorporating electrically rechargeable liquid fuels as the

storage medium, Science Bulletin, 2019, 64, 270-280.

21. X. Shi, X. Huo, Y. Ma, Z. Pan and L. An, Energizing fuel cells with an electrically rechargeable liquid fuel, Cell Reports Physical Science, 2020, 1, 100102.

Chapter 2 Single cell fabrications and characterizations

2.1 Introduction

The procedures for the fabrications and characterizations of the fuel cell and its key components are introduced in this chapter. Section 2.2 introduces the design and preparation procedures of the fuel cell, which includes the fixture, the MEA, and the e-fuel solution. Sections 2.3, 2.4 and 2.5 introduce the characterization methods for the electrode, the membrane and the liquid e-fuel, respectively. In addition, section 2.6 introduces the performance evaluation methods of the fuel cell, such as polarization curve test, constant-current discharging behavior test and the electrochemical impedance spectroscopy test.

2.2 Fuel cell fabrication and assembly

To evaluate the fuel cell performance, a home-made fuel cell fixture is designed and fabricated, as shown in Figures 2.1 and 2.2. At each side of the MEA, a plastic endplate, an aluminum heating plate, a gold-coated copper current collector and a graphite flow field engraved with serpentine flow channel are used.

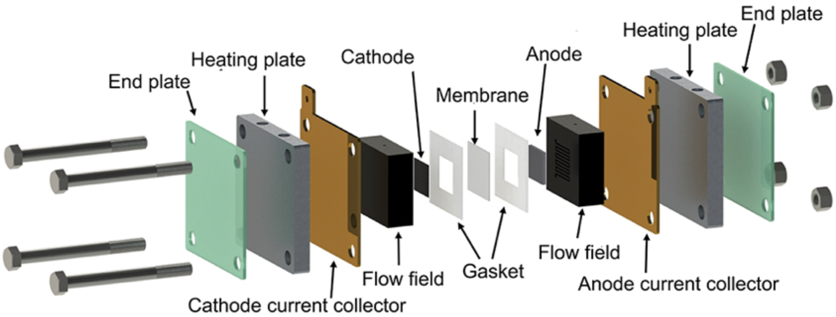

Figure 2.1 Design of a direct liquid fuel cell fixture using the e-fuel.

Furthermore, to avoid the leakage of gas and liquid fuel, several pieces of polytetrafluoroethylene (PTFE) gaskets are placed among the components. The whole configuration is fixed tightly by four bolts and nuts.

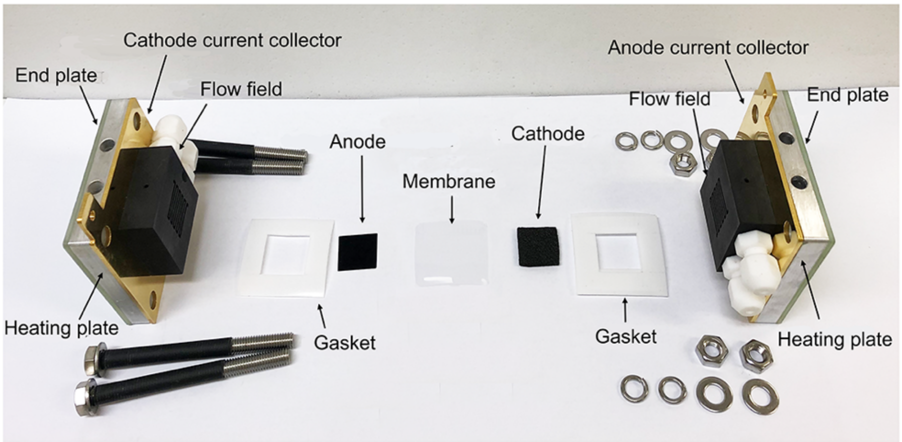

Figure 2.2 Fabrication of a direct liquid fuel cell fixture using the e-fuel.

2.2.1 Flow field and heating plates

A serpentine flow field is engraved on the graphite plate to provide the e-fuel/oxygen delivery passages. The flow channels are designed to be 1.0 mm deep and 1.0 mm wide. Meanwhile, on the top of the aluminum heating plate, there are two holes opened for placing the electrical heating rod.

2.2.2 Preparation of MEA

The MEA with an active area of 2.0 cm × 2.0 cm is prepared and placed in the middle of the cell, which is consisted of a commercial proton exchange membrane sandwiched by a catalyst-free graphite felt anode and a conventional Pt/C coated carbon paper cathode. The procedures to fabricate each component are presented in the following sections.

2.2.2.1 Preparation of anode

The procedures for the fabrication of the thermally treated graphite felt anode are given as follows:

1) A large piece of graphite felt (AvCarb G100, Fuel Cell Store) is cut off with a size of 10.0 cm × 10.0 cm.
2) The graphite felt is put into a muffle furnace and then heated at 500˚C in air for 5 hours to improve its wettability and electrochemical reactivity.
3) After naturally cooled down inside the muffle furnace, the thermally treated graphite felt is taken out and then cut into small pieces (2.0 cm × 2.0 cm) before being used for the fabrication of MEA.

2.2.2.2 Preparation of cathode

The procedures for the fabrication of the home-made Pt/C coated carbon paper cathode are given as follows:

1) Appropriate amount of 60 wt. % Pt/C powder (Johnson Matthey Co., USA), 5 wt. % Nafion (Fuel Cell Store, USA) and ethanol are blended to obtain a mixed solution.
2) The mixed solution is put into an ultrasonic bath for 30 mins to ensure its uniformity and obtain the final catalyst ink.
3) The carbon paper is cut into a size of 5.0 cm × 4.0 cm and then fixed on a heating plate using the tape with an exposing area of 4.0 cm × 4.0 cm.
4) A spray gun is used to uniformly spray the prepared ink onto the carbon

paper.

5) Wait for the catalyst layer to be dried.
6) Repeat the procedures 4) and 5) until the carbon paper reaches the desired catalyst loading.
7) The coated carbon paper is cut into four pieces each with a size of 2.0 cm × 2.0 cm before use.

2.2.2.2 Preparation of membrane

Nafion series membranes are employed as the proton exchange membrane, which are pretreated following the standard procedures:

1) The as-received Nafion membrane is immersed into 3.0 wt.% H_2O_2 solution and boiled in the water bath for 1 hour.
2) The membrane is taken out from the 3.0 wt.% H_2O_2 solution and then immersed into the deionized water and boiled in the water bath for 1 hour.
3) The membrane is taken out from the deionized water and then immersed into 1.0 M H_2SO_4 to be boiled in the water bath for 1 hour.
4) The membrane is taken out from the 1.0 M H_2SO_4 and again immersed into the deionized water and boiled in the water bath for 1 hour.
5) The membrane is cut into a size of 3.0 cm × 3.0 cm and stored in the deionized water before being used for the MEA fabrication.

2.2.3 Preparation of fuel

The liquid e-fuel is prepared with the procedures as follows:

1) Appropriate amount of vanadyl sulfate powder and sulfuric acid (98%) are added into the deionized water.
2) The mixed solution is kept stirring until a uniform solution is obtained.
3) After cooled down to room temperature, the mixed solution is transferred into a volumetric flask and then added with the deionized water until it reaches the line marked on the volumetric flask.
4) The mixed solution is fed into a typical flow cell to obtain the final liquid e-fuel, where the charge duration was changed in accordance with the e-fuel concentration needed.

2.3 Characterizations of electrodes

2.3.1 Material characterization

The X-ray diffraction (XRD) is a common technique that is used for the composition analysis. During the test, it generates the X-ray directed to the sample and then records the sample rotated angles and the intensity of reflected X-ray, which thereafter can be used to compare with the standard X- ray diffraction pattern for analysis. Using this technique, the XRD (D/max 2500PC) with Cu Kα radiation ($\lambda = 0.15406$ nm) is used to examine the compositions of the electrodes.

2.3.2 Surface morphology characterization

The scanning electron microscope is a common equipment that is used to characterize the morphology of a sample. It scans the surface of the sample using a focused beam of electrons, which then produces various signals that contain information about the surface topography. Using the field emission scanning electron microscope (SEM) (Tescan MAIA3, Japan), here, the morphology of the electrode including the pore size, the catalyst distribution, and the fiber alignment of the electrode are characterized.

2.3.3 Electrochemical performance characterization

The method used for examining the electrochemical performance of the electrode is named cyclic voltammetry, which has been used widely. The cyclic voltammetry test is conducted with a three-electrode electrochemical cell, in which the anode, platinum mesh and saturated calomel electrode (SCE) is used as working electrode, counter electrode and reference electrode, respectively. During the CV tests, the e-fuel containing 0.1 M V^{2+} ions in 1.5 M H_2SO_4 is used, while the voltage range is set to be between 0.1 and -1.0 V.

2.4 Characterizations of membranes

The electrochemical impedance spectroscopy (EIS) is a common method that is used to measure the impedance of a system by altering the current signal. Here, using this technique, to examine the ionic conductivity of the membrane, a home-made cell is designed and fabricated. The membrane is placed between two pieces of stainless-steel plate and then tested through conducting the EIS via the electrochemical workstation (Autolab PGSTAT 302 N, Netherlands) at a frequency range from 0.01 to 10^5 Hz. The resistance of the membrane is recorded, and its ionic conductivity is then calculated following the equation as shown below: [1]

$$\sigma_{\mathrm{m}}\ (\mathrm{S\ cm^{-1}}) = \frac{\delta_{\mathrm{m}}}{R_m a_{v,m}} \qquad (1)$$

where $\boldsymbol{\delta}_{\mathrm{m}}$ and $a_{v,m}$ represent the thickness and the effective area of the membrane sample, respectively. $\mathrm{R_m}$ represents the ohmic resistance of the membrane, which is obtained through the real-axis intercepts of the Nyquist plots, resulting from the contact resistance and ion-conducting resistance of the membrane. The test is conducted for three times to ensure the repeatability.

2.5 Characterizations of e-fuel solution

2.5.1 Electrochemical performance characterization

In order to determine the ionic conductivity (σ_{e}) of the liquid e-fuel, the EIS tests are also conducted for the liquid e-fuel in an electrochemical cell using the electrochemical workstation (CHI-660e, CH Instruments, China). The ionic conductivity is calculated according to:

$$\sigma_{\mathrm{e}}\ (\mathrm{S\ cm^{-1}}) = \frac{\sigma_{\mathrm{KCl}} \times \mathrm{R_{KCl}}}{\mathrm{R_e}} = \mathrm{G} \times \frac{1}{\mathrm{R_e}} \qquad (2)$$

Where σ_{KCl} represents the ionic conductivity of KCl standard solution. $\mathrm{R_{KCl}}$ and $\mathrm{R_e}$ represent the overall resistance (including contact resistance and ion-conducting resistance) of the KCl standard solution and the liquid e-fuel, respectively. [2] G represents the cell constant, which is first calibrated using 1.0 D KCl standard solution at 25 °C. [2,3]

2.5.2 Viscosity measurement

The Ubbelohde viscometer is a common instrument that has been used for measuring the liquid viscosity for decades. [4] It uses a capillary-based method for measuring the viscosity and is capable to be used under various temperature conditions and withstand the corrosive environment. Here, using the Ubbelohde viscometer, the viscosity of the liquid e-fuel is measured under various operating temperatures. [4]

2.6 Characterizations of fuel cells

2.6.1 Testing system

The setup for performance test of the fuel cell is shown in Figure 2.3, which mainly includes the liquid fuel cell, the fuel cell testing system, and the liquid e-fuel and oxidant supply system. The Arbin BT2000 is used to carry out the polarization curve test, constant-current discharging behavior test as well as the long-term discharging behavior test.

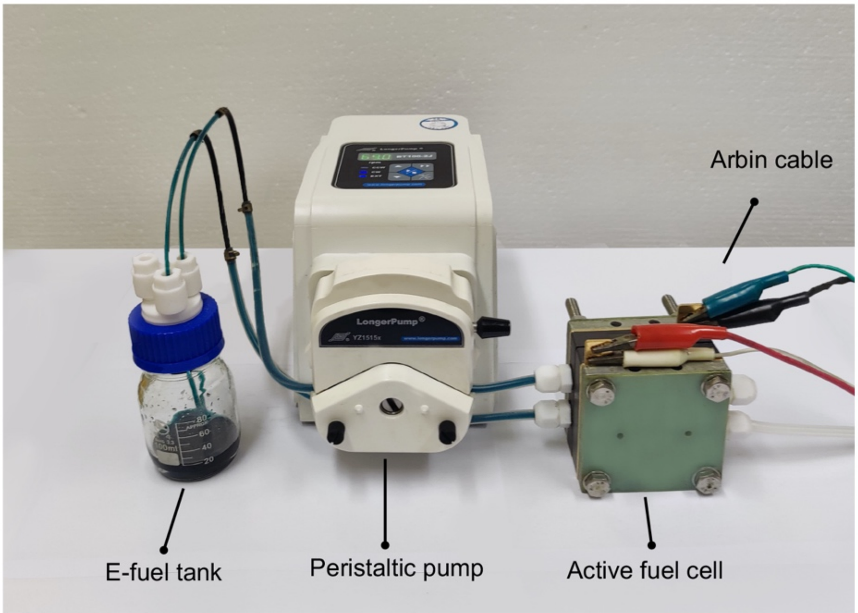

Figure 2.3 Experiment set-up of a direct liquid fuel cell using the e-fuel.

2.6.2 Fuel and oxidant supply system

The peristaltic pump is used to feed the liquid e-fuel stored in the tank to the anode side of the fuel cell. Meanwhile, an oxygen cylinder is connected to a mass flowmeter (Cole-Parmer, USA) to control the oxygen flow rate feeding into the cathode side of the fuel cell.

2.6.3 Temperature controlling system

A proportional-integral-derivative (PID) temperature controller (Anthone Electronic Co. Ltd., China) is used to heat the fuel cell. It is consisted of a pair of heating rods and a pair of K-typed thermocouples for heating and temperature monitoring, respectively. During the tests, the heating rods and the thermocouples are inserted into the heating plates of the fuel cell to heat the cell to desired operating temperature.

2.6.4 Polarization curves

The polarization test can provide the relationship between the voltage output and the applied current density loading. It can be used to analyze the contribution of different polarization losses including the activation loss, ohmic loss, and mass transport loss. The activation loss, dominant at low current density region, is majorly influenced by the activation energy required to initiate the electrochemical reaction. The ohmic loss is attributed to the ohmic resistance of the cell components. The mass transport loss results from the consumed reactive species near the electrode surface, which is dominant at the high current density region where reactants are depleted.

During the test, the discharging current density of the fuel cell started from 0 mA cm^{-2} kept increasing while the cell voltage is being recorded. The polarization curve can be obtained when the cell voltage drops below the cut-off voltage, from which the open-circuit voltage (OCV), peak power density, and maximum current density of the cell could be obtained.

2.6.5 Constant-current discharging behavior

The constant-current discharging test is an efficient approach to determine the operating behavior of the fuel cell during its real application, which not only accurately reveals the real performance of the system, but also measures its efficiencies and further evaluates its capability for practical applications. During the constant-current discharging test, the cell is operated under a constant current load while the voltage response being recorded.

2.6.6 Long-term operation behavior

The long-term operation behavior test is first conducted following the same method as the constant-current discharging behavior test. Afterwards, when the e-fuel is exhausted, the used e-fuel is first taken out from the tank. Then, the fresh liquid e-fuel is added into the tank to conduct the test again. The test will be conducted repeatedly to examine its long-term stability.

2.6.7 Faradic, voltage and energy efficiencies

In addition to the constant-current discharging behavior, the Faradic, voltage, and energy efficiencies are also essential on evaluating the performance of a fuel cell. To begin with, the Faradic efficiency η, which is also known as the fuel utilization efficiency, can be obtained with Eq. (4): [5]

$$\eta = \frac{\int i(t)dt}{c_{init}VF} \tag{3}$$

where t is the duration of the discharging process; $i(t)$ is the discharging current; c_{init} represents the initial concentration of V^{2+} ions in the e-fuel solution, V is the volume of the e-fuel solution and F is the Faraday constant. The energy efficiency (ξ), as one significant indicator in evaluating the capability of the fuel cell to efficiently convert chemical energy to electricity, is calculated based on the product of the voltage efficiency ($\varphi = \frac{E_{aver}}{E_{theo}}$) and Faradic efficiency (η): [5]

$$\xi = \varphi \times \eta = \frac{E_{aver}}{E_{theo}} \times \eta \tag{4}$$

Where E_{aver} is the average discharging voltage, while E_{theo} is the theoretical average voltage. ΔE is the theoretical voltage which is calculated based on the Nernst equation as: [6]

$$\mathrm{E_{theo}} = \frac{\int_0^{c_{init}} \Delta E dc}{c_{init}} = \frac{\int_0^{c_{init}} [E^0 + \frac{RT}{F} \ln(\frac{c_{V^{2+}}}{c_{V^{3+}}})] dc}{c_{init}} \tag{5}$$

where R is the universal gas constant and T is the absolute temperature.

2.6.8 Electrochemical impedance spectroscopy

The EIS test, as discussed above, is a powerful tool in the diagnosis and characterization of fuel cell performance. [7] To examine the resistance of the system, the electrochemical workstation (CHI-605C, CH Instruments, China) is used to conduct the EIS test for the fuel cell. During the test, the cell is first operated under the same condition as the polarization curve test, except being placed under the open circuit condition where no discharging current is applied. Afterwards, the EIS test is being conducted at a frequency range between 0.01 to 10^5 Hz for analyze the resistance.

2.7 Summary

In this chapter, the fabrications of the direct liquid fuel cell including the preparation method of MEA are introduced. Moreover, the characterization techniques for the electrode, the membrane, the e-fuel solution and the fuel cell are described detailly.

2.8 References

1. X. Shi, X. Huo, O. C. Esan, Y. Ma, L. An and T. Zhao, A liquid e-fuel cell operating at− 20° C, Journal of Power Sources, 2021, 506, 230198.

2. F. Azeez and P. S. Fedkiw, Conductivity of libob-based electrolyte for lithium-ion batteries, Journal of Power Sources, 2010, 195, 7627-7633.

3. D. Feng and L. Holland, A dc Method for the Absolute Determination of Conductivities of the Primary Standard KCl Solutions from 0^ C to 50" C, Journal of Research of the National Institute of Standards and Technology, 1994, 99.

4. S. Zhang, B. Zhang, G. Zhao and X. Jian, Anion exchange membranes from brominated poly (aryl ether ketone) containing 3, 5-dimethyl phthalazinone moieties for vanadium redox flow batteries, Journal of Materials Chemistry A, 2014, 2, 3083-3091.

5. J. Liu, T.-S. Zhao, R. Chen and C. W. Wong, Effect of methanol concentration on passive DMFC performance, Fuel Cells Bulletin, 2005, 2005, 12-17.

6. K. Knehr and E. Kumbur, Open circuit voltage of vanadium redox flow batteries: Discrepancy between models and experiments, Electrochemistry Communications, 2011, 13, 342-345.

7. Z. Tang, Q.-A. Huang, Y.-J. Wang, F. Zhang, W. Li, A. Li, L. Zhang and J. Zhang, Recent progress in the use of electrochemical impedance spectroscopy for the measurement, monitoring, diagnosis and optimization

of proton exchange membrane fuel cell performance, Journal of Power Sources, 2020, 468, 228361.

Chapter 3 Performance characteristics of an active fuel cell

3.1 Introduction

In an attempt to reduce environmental pollutions and achieve sustainable energy development, more and more efforts have been devoted to develop alternative technologies for power generation in the last decades. [1] Fuel cells, as an advanced energy conversion system, which can continuously convert chemical energy into electricity, have therefore been extensively studied since its first invention in the middle of the 19th century. [2-4] After decades of research, hydrogen fuel cells, which utilize hydrogen as fuel with its fast reaction kinetics on the Pt catalysts and the zero-emission feature, are regarded as the most promising fuel cell system. [5-7] However, up till now, the real application of hydrogen fuel cells is still being constrained by some challenges mostly associated with the hydrogen production, storage and transportation. Therefore, liquid fuel cells, utilizing alcohol fuels towards achieving higher energy density and easier fuel handling, have been proposed and deeply investigated especially in recent years. [8,9] Nonetheless, due to the sluggish reaction kinetics of alcohol liquid fuels, even on noble metal catalysts, [10,11] the performances of conventional liquid fuel cells are still limited, which has greatly restricted their application scenarios. It is therefore of paramount importance to propose other potential fuels suitable for the operation of liquid fuel cells towards achieving a better performance.

Recently, a novel electrically rechargeable liquid fuel (e-fuel) has been proposed and attracted worldwide attention. [12,13] Radically different from conventional liquid fuels, such as methanol and ethanol, this e-fuel is typically made of various electroactive species including inorganic materials (*e.g.,* metal ions), organic materials (*e.g.,* alloxazines) and suspension of particles (*e.g.,* polysulphide-based nanofluid). Comparing to conventional liquid fuels, this e-fuel offers three major advantages. [12] Firstly, this e-fuel can be recharged and recycled by a simple electrochemical reaction, greatly reducing the e-fuel production cost of the system. It was reported that the e-fuel solution can be used for over 100 cycles, showing a coulombic efficiency of around 98% and a capacity decay rate of 0.1% per cycle and thus proving its excellent rechargeability. [12] Secondly, this e-fuel shows a high electrochemical reactivity even on carbon-based materials, thereby eliminating the use of any noble metal catalysts, which not only thus dramatically reduces the cell fabrication cost, but also greatly improves the fuel cell durability. Thirdly, many liquid fuels (*e.g.,* ethanol) suffer from the difficulty of breaking strong carbon-carbon bonds on the existing electrocatalysts, seriously limiting the fuel cell power density and energy efficiency, while this e-fuel exhibits super faster kinetics and complete oxidation (typically one-electron transfer process), dramatically boosting the fuel cell performance and in turn reducing the fuel cell system cost per unit power.

Although the lithium-ion battery technology has achieved great success during its commercialization process and becomes the most widely used power source in battery electric vehicles (BEV), [14-16] its low energy capacity, as well as long recharging duration, seriously restrict the travel distance of BEV and their market penetration. [17-19] In comparison, the fuel cell using e-fuel can independently alter its storage capacity (via changing the e-fuel volume and concentration) and power (via changing the electrode size), respectively. Meanwhile, the e-fuel cell can be recharged by simply replacing the exhausted e-fuel solution with a fresh one, like refueling gasoline, which greatly shortens the recharging time.

Inspired by the e-fuel concept, herein, we demonstrate a direct liquid fuel cell fed with the e-fuel solution as fuel and the pure oxygen as oxidant. Like conventional fuel cells, this e-fuel cell has a sandwich-like structure consisting of a catalyst-free graphite-felt anode and a conventional oxygen cathode separated by a proton exchange membrane. In addition, the e-fuel cell system also includes an e-fuel/oxygen delivery system and other external accessories. It is experimentally found that this fabricated e-fuel cell achieved an extraordinarily high peak power density of 857.0 mW cm^{-2} and a maximum current density of 1980 mA cm^{-2} at 60 °C. Hence, the above-mentioned advantages make the present e-fuel cell system a promising candidate for powering fuel cell electric vehicles (FCEVs) in the future.

3.2 Working Principle

The structure of the liquid fuel cell including a membrane electrode assembly (MEA), which is sequentially clamped by flow fields, heating plates, and current collectors is shown in Figure 3.1. It employs the oxygen reduction reaction (ORR) at its cathode side, while using a liquid e-fuel containing vanadium ions at its anode side. The overall reaction inside the cell is given as:

$$V^{2+} + \frac{1}{4}O_2 + H^+ \rightarrow V^{3+} + \frac{1}{2}H_2O \qquad E^0 = 1.49\text{V} \qquad (1)$$

By utilizing this liquid e-fuel, the cell achieves a high theoretical voltage of 1.49 V under standard state condition, which exceeds those of hydrogen fuel cells (1.23 V) [21] and other common alcohol fuel cells.

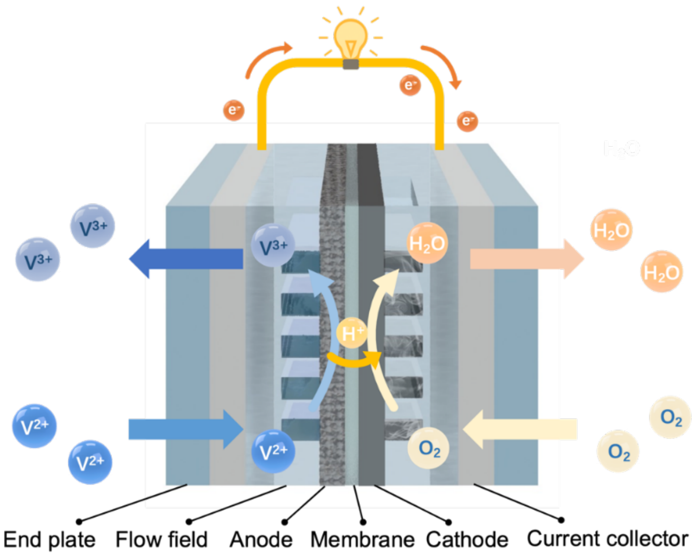

Figure 3.1 Working principle of a liquid fuel cell using e-fuel.

3.3 Experiments

3.3.1 E-fuel cell

The MEA with an active area of 2.0 × 2.0 cm^2 was prepared using the method as discussed before. [20] Four different kinds of cathode with various Pt/C catalyst loadings of 0.5, 1.0, 2.0 and 4.0 mg cm^{-2} were prepared. While four commercial membranes including Nafion 211 (25.4 μm), Nafion 212 (50.8 μm), Nafion 115 (127.0 μm) and Nafion 117 membranes (183.0 μm) with different thicknesses were pre-treated for further investigation. The graphite felt (AvCarb G100, Fuel Cell Store, USA) used as the anode was thermally treated in the air at 500˚C for 5 hours. The MEAs were assembled into the homemade fixture as reported before to fabricate the liquid e-fuel cell. [20]

3.3.2 Experimental apparatus and test conditions

The experimental setup contains a liquid e-fuel cell, a proportional-integral-derivative (PID) temperature controller (Anthone Electronic Co. Ltd., China) and other relevant accessories. The PID temperature controller consists of a pair of heating rods and a pair of K-typed thermocouples for heating and temperature monitoring, respectively. During the experiment, the cell was first heated while being fed with deionized water at anode and humidified oxygen with a flow rate of 250 sccm at cathode. When the cell reached the targeted operating temperatures, the deionized water was replaced by the e-fuel to conduct further tests. The e-fuel was first prepared by dissolving $VOSO_4$ powder into sulfuric acid and then charged using a flow cell. [20] The charged e-fuel was purged with nitrogen consistently during the whole experiment in order to prevent oxidation by the air. The polarization and constant-current discharging tests were conducted and recorded with a fuel cell testing system (Arbin BT2000, Arbin instrument Inc.). The electrochemical impedance spectroscopy (EIS) of the cell (from 0.01Hz to 100 kHz) was conducted by an electrochemical workstation (CHI-605C, CH Instruments, China). The X-ray diffraction (XRD) (Rint-2000, Rigaku, Japan) with Cu Kα radiation (λ = 0.15406 nm) and the scanning electron microscope (SEM) (SU5000, Hitachi, Japan) were used to examine the composition and morphology of the cathode, respectively, both before and after the long-term operation. The morphology of the anode was also characterized using the SEM. An electrochemical workstation (CHI-605C, CH Instruments, China) was used to conduct the electrochemical impedance spectroscopy (EIS) and cyclic voltammetry (CV) tests. The EIS tests were conducted with a frequency range between 0.01 to 10^5 Hz. The CV tests were conducted by a three-electrode electrochemical cell, in which the graphite felt (both of pristine graphite felt and thermally treated graphite felt), platinum mesh and saturated calomel electrode (SCE) were used as working electrode, counter electrode and reference electrode, respectively. The e-fuel solution for CV tests is an aqueous solution containing 0.1 M V^{2+} ions and 1.5 M H_2SO_4, and the voltage range was 0.1 to -1.0 V.

3.4 Results and discussion

3.4.1 General performance

In this work, a liquid e-fuel cell assembled with the cathode of 4.0 mg cm^{-2}

Pt working at 60 ˚C was examined. As shown in Figure 3.2 (a), the cell presents an open-circuit voltage of 1.15 V and demonstrates a peak power density of 857.0 mW cm^{-2}, which indicated that the performance was effectively enhanced. Such a superior peak power density not only substantially surpasses conventional liquid fuel cells, but also comparable to the hydrogen-oxygen fuel cells. [22-25] In addition, the cell further achieves an energy efficiency of 41.8 % at 200 mA cm^{-2} (Figure 3.2 (b)), demonstrating a much higher efficiency in comparison to the conventional alcohol fuel cells. [26-30] These results prove that increasing the operating temperature and the cathode catalyst loading are effective methods to overcome the major performance limitation of the liquid e-fuel cell resulting from the sluggish kinetics of the ORR. [31,32] Thus, with the advantages of ease of e-fuel handling and fast response, this present cell is believed to be a promising competitor for real applications in the future.

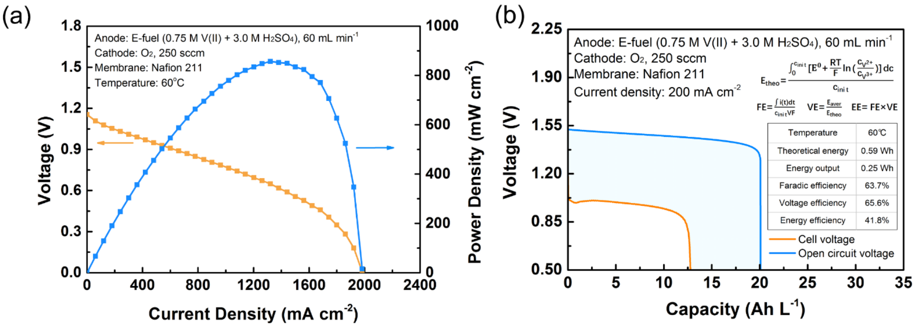

Figure 3.2 (a-b) General performance of this liquid fuel cell at 60˚C.

3.4.2 Physical and chemical characterizations of anode

The surface morphology of the catalyst-free graphite-felt anode was characterized by the SEM. It is seen from Figures 3.3 (a-b) that the catalyst-free graphite-felt anode built with its interconnected carbon fibers, [33] thereby eliminating the use of noble metal catalysts. [34,35]

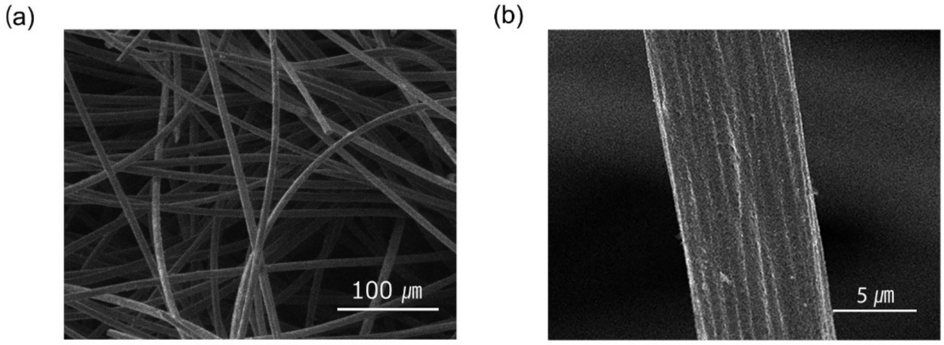

Figure 3.3 (a-b) Surface morphologies of the catalyst-free graphite-felt anode.

To evaluate the electrochemical performance improvement of the catalyst-free graphite-felt anode after thermal treatment, cyclic voltammograms (CV) test was firstly carried out at different scan rates and the results are shown in Figures 3.4 (a-b). Without thermal treatment, there is no distinct oxidation peak corresponding to the oxidation of the V^{2+} ions. In contrast, a clear and high anodic peak appears after thermal treatment, indicating that the e-fuel solution is highly reactive on the thermally treated graphite-felt electrode even without using any noble metal catalysts. Such a performance improvement after the thermal treatment is mainly attributed to the following aspects: i) the reaction between oxygen and graphite felt creates oxygen functional groups (*e.g.,* hydroxyl functional groups), which can accelerate the vanadium-ion oxidation; [36] ii) meanwhile, the reaction will also create numerous pores on the surface and thus enlarge the specific surface area; [37] and iii) the formation of oxygen functional groups further improves the hydrophilicity and thus increases the effective surface area. [34,38,39] Thus, this striking feature ensures the e-fuel cell with cost-effectivity and durability. [34] It should be also mentioned that radically different from the catalyst layer made of granular materials in conventional direct liquid fuel cells, the anode of this direct liquid e-fuel cell is made of fibrous graphite-felt materials, which has a dual-scaled pore structure (primary pores formed by voids among the fibers and secondary pores inside fibers created by thermal treatment). [40,41]

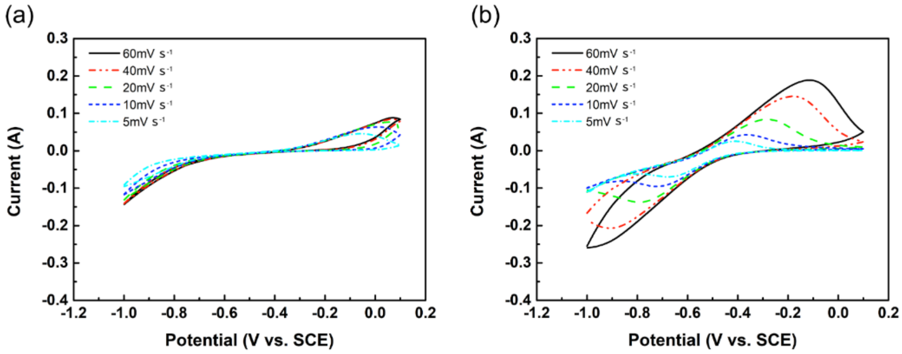

Figure 3.4 Electrochemical kinetics of the catalyst-free graphite-felt electrode (a) before and (b) after thermal treatment.

3.4.3 Effect of the cathode catalyst loading

As mentioned, this liquid fuel cell, with the superior reactivity of liquid e-fuel even on graphite felt, successfully frees the anode from any catalysts. [20] On the other hand, the poor reactivity of oxygen at the cathode side becomes a great barrier hampering the overall cell performance. One common approach of improving the reactivity of oxygen is to increase the cathode catalyst loading, as a higher catalyst loading can provide a larger active surface area and thereby efficiently enhance the ORR. [42] Hence, to examine the influences of catalyst loading on the e-fuel cell performance, cathodes with four different Pt loadings of 0.5, 1.0, 2.0, and 4.0 mg cm^{-2} are prepared and assembled into the e-fuel cell for examination. A series of polarization curves and power density curves are obtained at room temperature (Figure 3.5). It can be viewed that within the tested catalyst loading range, the fuel cell performance improves with the Pt loading. As the catalyst loading increases to 4.0 mg cm^{-2}, the maximum current density and peak power density boosts up to 1740.0 mA cm^{-2} and 588.7 mW cm^{-2}, respectively. Such an improved performance proves that the cathode catalyst loading is a crucial factor that influences the reaction kinetics of oxygen reduction, [43] which further determines the overall cell performance. It is also worth to mention that, a further increase of the catalyst loading above 4.0 mg cm^{-2} is not examined in this study for two reasons. Firstly, a higher catalyst loading will induce a thicker catalyst layer, which may deteriorate the mass transport and also decline the ORR activity, thereby limiting the cell performance. [44] Moreover, to fulfill the requirement for real application, the capital cost of this system needs to be low. Considering the fact that the cell is able to generate a performance comparable to hydrogen fuel cells at 60 ˚C, with a loading of 4.0 mg cm^{-2}, a further increase of the catalyst loading is thus considered not to be cost-effective. Therefore, in this work, the cathode achieving the best performance with a Pt loading of 4.0 mg cm^{-2} is chosen for further studies.

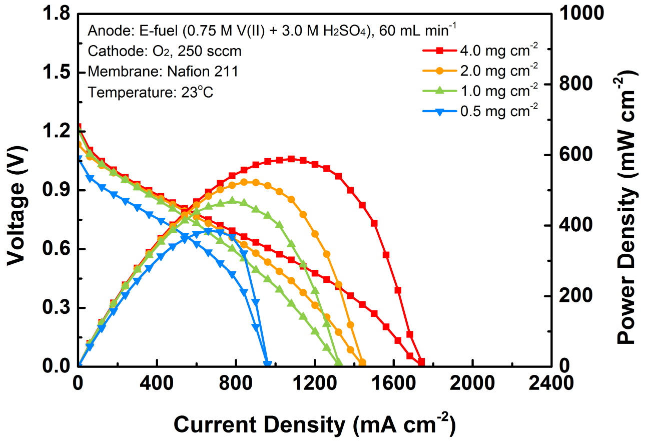

Figure 3.5 Polarization curves and power density curves of this liquid fuel cell with various cathode catalyst loadings.

3.4.4 Effect of the membrane thickness

Membrane is one of the most crucial components in this liquid fuel cell. On one hand, it plays an important role to prevent the crossover of liquid e-fuel, as the permeation of e-fuel to the cathode would lead to mixed potential and further results in large voltage loss. [45,46] On the other hand, it should also allow the ease of protons transport between the two half-cells so as to reduce ohmic loss. As widely demonstrated before, the commercial Nafion membranes with a large thickness could prevent the crossover of reactive species more effectively, while it may also lead to higher internal resistance, which thereby results in significant voltage loss according to the Ohm's law. [47,48] Hence, to examine the effect of membrane thickness, membranes including Nafion 117 (183.0 μm), Nafion 115 (127.0 μm), Nafion 212 (50.8 μm) and Nafion 211 (25.4 μm) are selected for investigation at room temperature (Figure 3.6). It can be viewed from the polarization curves that, as the membrane thickness increases, the liquid fuel cell performance decreases. Overall, the cell assembled with the membrane of the least thickness (25.4 μm) outperforms the other membranes, demonstrating the best performance. Such result suggests that the ohmic resistance of the membrane plays a key role on the cell performance, while the influences of crossover seems not to be obvious. However, it is predicted that a thin membrane may eventually induce severe crossover of reactive species, thereby limiting the cell performance. Hence, in this work, to ensure the cell with a higher peak power density, Nafion 211 membrane is considered as the best choice for the liquid e-fuel cell.

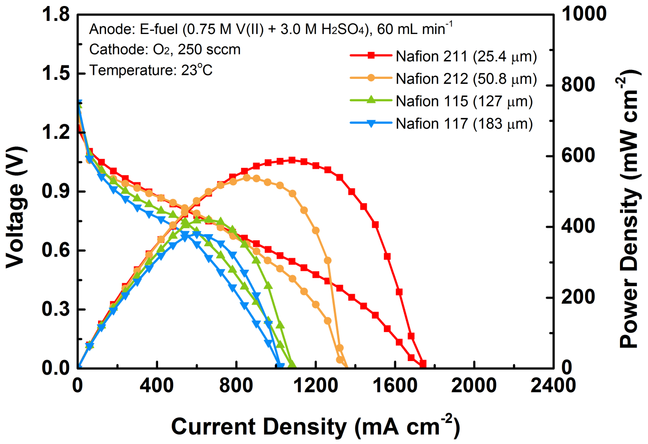

Figure 3.6 Polarization curves and power density curves of this liquid fuel cell with various membrane thicknesses.

3.4.5 Effect of the operating temperature

As mentioned in the previous section, the sluggish kinetics at cathode is one of the major limitations restraining the overall fuel cell performance. To overcome this problem, other than increasing the cathode catalyst loading, raising the operating temperature is another effective approach that has been widely demonstrated. [49,50] Hence, to examine the effect of the operating temperature, experiments were conducted from 23 to 60˚C as shown in Figure 3.7 (a). It is found that, when operated at 60˚C, the cell achieves a maximum current density of 1980.0 mA cm^{-2} with a peak power density of 857.0 mW cm^{-2}.

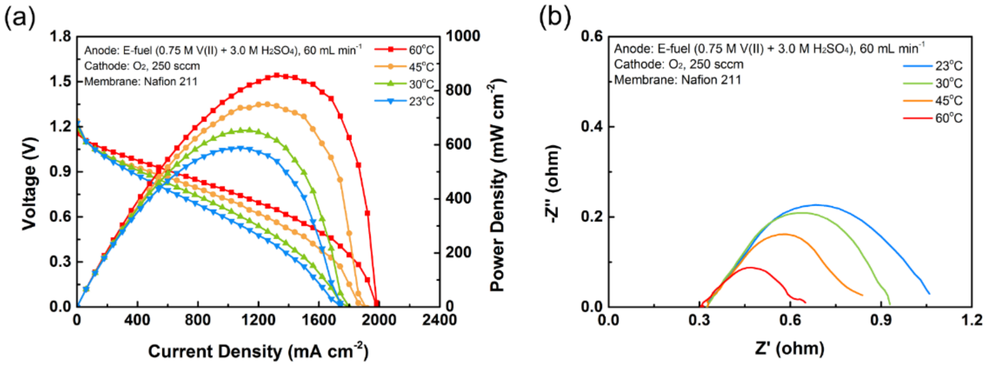

Figure 3.7 (a) Polarization, power density, and (b) EIS curves of this liquid fuel cell at various operating temperatures.

Its performance improvement under a higher operating temperature can be mainly attributed to the following reasons. Firstly, the elevation of operating temperature is an effective method that improves the sluggish reaction kinetic of oxygen reduction, [51] and thereby reduces the voltage loss. Furthermore, while the e-fuel is able to exhibit fast reaction kinetic even under room temperature due to its good reactivity, the higher operating temperature can indeed improves the e-fuel conductivity and lowers the viscosity, [52] which facilitates the reactants transport and thereby reduces the cell internal resistance. [42,53,54] Additionally, the ionic conductivity of Nafion 211 membrane is also closely related to the operating temperature, and a higher ionic conductivity can be presented at 60˚C due to the improved diffusion and migration process of protons through the membrane. [55-57] In summary, with the increase of the operating temperature, the resistance of e-fuel cell can be reduced as proven by the EIS results (Figure 3.7 (b)), which in turn leads to the exceptionally high cell performance. However, it is worth to mention that, the elevated operating temperature would, on the other hand, result in a more aggravated cross-over of vanadium ions and oxygen molecules through the membrane, [58] which would eventually lead to a severe fuel loss and performance degradation of the system.

3.4.6 Constant-current discharging behavior

The constant-current discharging test is widely applied for the examination of the actual operating behavior as well as the energy losses of a fuel cell system. Utilizing this method, here, the fuel cell was tested under an operating temperature range from 23 to 60˚C at 200 mA cm^{-2} with the e-fuel containing 0.75 M V(II), as shown in Figure 3.8 (a). The associated energy losses and three efficiencies are also calculated and summarized in Figure 3.8 (b).

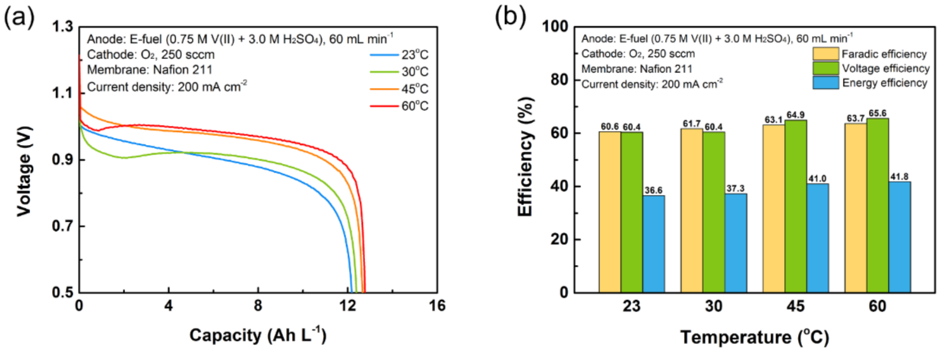

Figure 3.8 (a) Constant-current discharging behaviors of this liquid fuel cell and (b) comparison of three efficiencies at various operating temperatures.

It is observed that the increase of operating temperature leads to an increased discharge voltage plateau and thereby a higher voltage efficiency (VE), which primarily results from the lowered cell resistance in view of the enhanced conductivities of both the liquid e-fuel and the membrane as demonstrated earlier in Figure 3.7 (b). [52,59] Furthermore, this temperature variation also results in a higher discharge capacity leading to a larger Faradic efficiency, which is due to the fact that the elevated temperature can accelerate the reaction kinetics on both sides, enhancing the utilization of the liquid e-fuel. However, it is worth mentioning that, as the temperature rises, it simultaneously leads to an aggravated crossover of both the e-fuel and oxygen molecules, [53,60] which would result into a serious capacity loss. Overall, only a minor improvement on the discharge capacity are found. Nonetheless, the energy efficiency (EE) of the e-fuel cell elevates from 36.6% to 41.8% with the temperature increase to 60°C, proving that high operating temperature can effectively improve the discharging performance of this liquid e-fuel cell.

3.4.7 Long-term operation behavior

Long-term stability is of significant importance before realizing the widespread application of a fuel cell system. [61] Here, to examine the ability of this cell for long-term operation, the cell has been refueled for 50 times and discharged at 10 mA cm^{-2} at 60˚C.

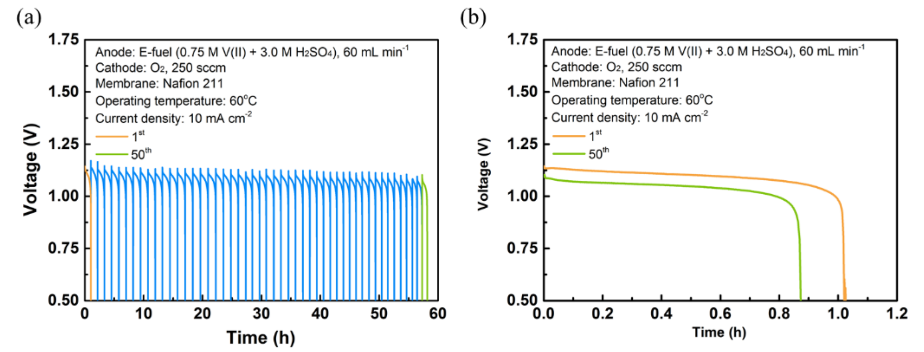

Figure 3.9 (a) Long-term discharging behaviors of this liquid fuel cell and (b) the comparison of 1st and 50th discharging curves.

The discharge curves are presented in Figure 3.9, while the efficiencies of these 50 cycles are calculated in Figure 3.10. It is shown that the present system is able to achieve a continuous and stable power generation for nearly 60 hours, with its almost instantaneous rechargeability through replacing the exhausted e-fuel with fresh ones. Furthermore, the cell also presents a relatively stable efficiency, with only a minor EE decrease of 1.4 % after 50 times refueling, indicating its potential for stable operation at high operating temperatures. However, it is noteworthy that the EE of this system at 10 mA cm^{-2} is much lower in comparison to its efficiency achieved at 200 mA cm^{-2} (Figure 3.8 (b)), which is attributed to the prolonged discharge duration leading to a more serious crossover of reactive species and a lower e-fuel utilization efficiency. [62,63]

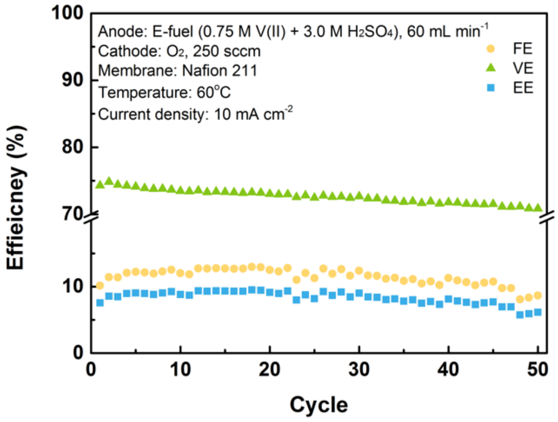

Figure 3.10 Faradic, voltage and energy efficiencies of the fuel cell during long-term operation

Hence, in the future, the development of a membrane with better selectivity could be a research direction with great importance for the enhancement of the liquid e-fuel cell performance of long-term operation at higher operating current densities. After the long-term operation test, the cell was then disassembled and the MEA without any obvious appearance damage can be seen as shown in Figure 3.11.

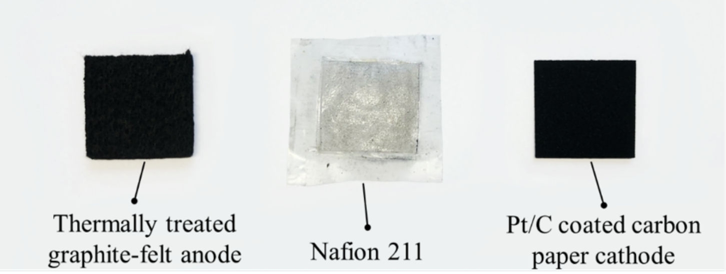

Figure 3.11 Disassembled membrane electrode assembly (MEA) after long-term operation.

To further examine the durability of the cathode, its XRD patterns (Figure 3.12 (a)) and SEM images (Figure 3.12 (b)), both before and after the long-term operation are obtained. It can be seen from these results that, little changes can be observed after the long-term operation, indicating the good chemical stability of the cathode, which again proves the capability of this liquid e-fuel cell for long-term operation. It is also worth to mention that, attributed to the excellent reactivity of the e-fuel even on carbon-based materials, which eliminate the use of any noble metal catalysts, this present system also demonstrates with a system cost estimation per unit power as low as US\$1286.74 kW^{-1}, showing it to be much more cost-effective than the conventional direct liquid fuel cells. (Table 3-1)

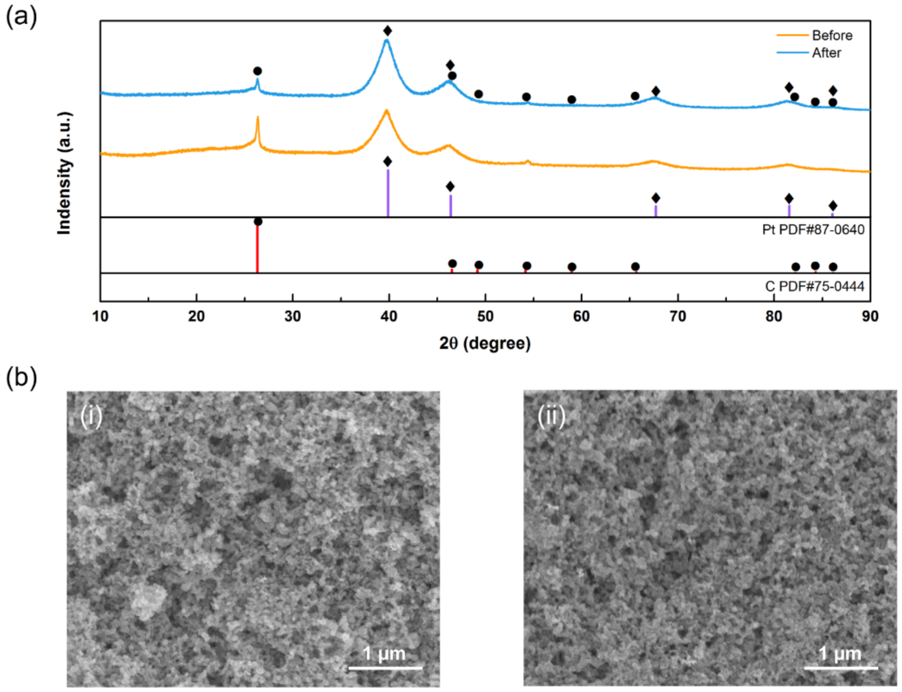

Figure 3.12 (a-b) XRD curves and SEM images of the cathode catalyst layer (i) before and (ii) after long-term discharging.

3.5 Summary

In this work, we have demonstrated the operation of an e-fuel cell that is free of anode catalysts and capable of achieving a peak power density of 857.0 mW cm^{-2} at 60˚C. It is revealed that a higher catalyst loading at the cathode side, along with the increase of operating temperature, can effectively resolve the limitation induced from the sluggish ORR kinetic and further boost the cell performance. In addition, the cell further attains an energy efficiency of 41.8 % even at 200 mA cm^{-2} with a stable operation of ~60 hours, illustrating its ability for efficient power generation and excellent long-term operation stability. It should be mentioned that the increase of operating temperature and the decrease of membrane thickness present a positive effect on the cell performance, but both can induce severe crossover of reactive species thereby deteriorating the cell performance especially during constant-current discharging. Hence, with the development of membranes with better selectivity and catalysts with better catalytic reactivity for oxygen reduction reaction, it is believed that this e-fuel cell could achieve even better performance, positioning it as a promising power generation technology in the future.

3.6 References

1. M. Contestabile, G. Offer, R. Slade, F. Jaeger and M. Thoennes, Battery electric vehicles, hydrogen fuel cells and biofuels. Which will be the winner?, Energy & Environmental Science, 2011, 4, 3754-3772.

2. K.-S. Lee, J. S. Spendelow, Y.-K. Choe, C. Fujimoto and Y. S. Kim, An operationally flexible fuel cell based on quaternary ammonium-biphosphate ion pairs, Nature energy, 2016, 1, 16120.

3. D. Y. Chung, J. M. Yoo and Y. E. Sung, Highly durable and active Pt-based nanoscale design for fuel-cell oxygen-reduction electrocatalysts, Advanced Materials, 2018, 30, 1704123.

4. X. Yuan, X.-L. Ding, C.-Y. Wang and Z.-F. Ma, Use of polypyrrole in catalysts for low temperature fuel cells, Energy & Environmental Science, 2013, 6, 1105-1124.

5. M. Lopez-Haro, L. Guétaz, T. Printemps, A. Morin, S. Escribano, P.-H. Jouneau, P. Bayle-Guillemaud, F. Chandezon and G. Gebel, Three-dimensional analysis of Nafion layers in fuel cell electrodes, Nature communications, 2014, 5, 1-6.

6. Y.-C. Chiang and J.-R. Ciou, Effects of surface chemical states of carbon nanotubes supported Pt nanoparticles on performance of proton exchange membrane fuel cells, International Journal of Hydrogen Energy, 2011, 36, 6826-6831.

7. J. Zhang, Z. Xie, J. Zhang, Y. Tang, C. Song, T. Navessin, Z. Shi, D.

Song, H. Wang and D. P. Wilkinson, High temperature PEM fuel cells, Journal of Power Sources, 2006, 160, 872-891.

8. W. Huang, H. Wang, J. Zhou, J. Wang, P. N. Duchesne, D. Muir, P. Zhang, N. Han, F. Zhao and M. Zeng, Highly active and durable methanol oxidation electrocatalyst based on the synergy of platinum–nickel hydroxide–graphene, Nature communications, 2015, 6, 1-8.

9. S. Han, Y. Yun, K. W. Park, Y. E. Sung and T. Hyeon, Simple solid-phase synthesis of hollow graphitic nanoparticles and their application to direct methanol fuel cell electrodes, Advanced Materials, 2003, 15, 1922-1925.

10. S. Song and P. Tsiakaras, Recent progress in direct ethanol proton exchange membrane fuel cells (DE-PEMFCs), Applied Catalysis B: Environmental, 2006, 63, 187-193.

11. C. Liu, W. Zhou, J. Zhang, Z. Chen, S. Liu, Y. Zhang, J. Yang, L. Xu, W. Hu and Y. Chen, Air-Assisted Transient Synthesis of Metastable Nickel Oxide Boosting Alkaline Fuel Oxidation Reaction, Advanced Energy Materials, 2020, 10, 2001397.

12 Jiang, H., Wei, L., Fan, X., Xu, J., Shyy, W. and Zhao, T. (2019). A novel energy storage system incorporating electrically rechargeable liquid fuels as the storage medium. Sci. Bull. 64, 270-280.

13 Amine, K. (2019). E-fuel system: a conceptual breakthrough for energy storage. Sci. Bull. 64, 227-228.

14 Younesi, R., Veith, G. M., Johansson, P., Edström, K. and Vegge, T. (2015). Lithium salts for advanced lithium batteries: Li–metal, Li–O2, and Li–S. Energy Environ. Sci. 8, 1905-1922.

15 Fan, X., Ji, X., Chen, L., Chen, J., Deng, T., Han, F., Yue, J., Piao, N., Wang, R. and Zhou, X. (2019). All-temperature batteries enabled by fluorinated electrolytes with non-polar solvents. Nat. Energy 4, 882-890.

16 Shi, X., Sun, Q., Boateng, B., Niu, Y., Han, Y., Lv, W. and He, W. (2019). A quasi-solid composite separator with high ductility for safe and high-performance lithium-ion batteries. J. Power Sources 414, 225-232.

17 Bai, P., Li, J., Brushett, F. R. and Bazant, M. Z. (2016). Transition of lithium growth mechanisms in liquid electrolytes. Energy Environ. Sci. 9, 3221-3229.

18 Liu, J., Shi, X., Boateng, B., Han, Y., Chen, D. and He, W. (2019). A Highly Stable Separator from an Instantly Reformed Gel with Direct Post-Solidation for Long-Cycle High-Rate Lithium-Ion Batteries. ChemSusChem 12, 908-914.

19 Zhao, Y., Setzler, B. P., Wang, J., Nash, J., Wang, T., Xu, B. and Yan, Y. (2019). An efficient direct ammonia fuel cell for affordable carbon-neutral transportation. Joule 3, 2472-2484.

20. X. Shi, X. Huo, Y. Ma, Z. Pan and L. An, Energizing fuel cells with an electrically rechargeable liquid fuel, Cell Reports Physical Science, 2020, 1, 100102.

21. S. A. M. Shaegh, N.-T. Nguyen, S. M. M. Ehteshami and S. H. Chan, A membraneless hydrogen peroxide fuel cell using Prussian Blue as cathode material, Energy & Environmental Science, 2012, 5, 8225-8228.

22. J. Liu, M. Jiao, L. Lu, H. M. Barkholtz, Y. Li, Y. Wang, L. Jiang, Z. Wu, D.-j. Liu and L. Zhuang, High performance platinum single atom electrocatalyst for oxygen reduction reaction, Nature communications, 2017, 8, 1-10.

23. N. Steffy, V. Parthiban and A. Sahu, Uncovering Nafion-multiwalled carbon nanotube hybrid membrane for prospective polymer electrolyte membrane fuel cell under low humidity, Journal of Membrane Science, 2018, 563, 65-74.

24. H.-F. Lee, J.-Y. Chang and Y. W. Chen-Yang, Improvement in physical properties of single-layer gas diffusion layers using graphene for proton exchange membrane fuel cells, RSC advances, 2018, 8, 22506-22514.

25. V. M. Umap and R. P. Ugwekar, Performance analysis of gas diffusion electrode with varying platinum loading under different oxidant condition, Renewable Energy, 2020.

26. H. Deng, Y. Zhang, X. Zheng, Y. Li, X. Zhang and X. Liu, A CNT (carbon nanotube) paper as cathode gas diffusion electrode for water management of passive μ-DMFC (micro-direct methanol fuel cell) with highly concentrated methanol, Energy, 2015, 82, 236-241.

27. F. Zhang, J. Jiang, Y. Zhou, J. Xu, Q. Huang, Z. Zou, J. Fang and H.

Yang, A neat methanol fed passive DMFC with a new anode structure, Fuel Cells, 2017, 17, 315-320.

28. Z. Yuan, W. Chuai, Z. Guo, Z. Tu and F. Kong, Investigation of self-adaptive thermal control design in passive direct methanol fuel cell, Energy Storage, 2019, 1, e64.

29. V. Bambagioni, C. Bianchini, Y. Chen, J. Filippi, P. Fornasiero, M. Innocenti, A. Lavacchi, A. Marchionni, W. Oberhauser and F. Vizza, Energy Efficiency Enhancement of Ethanol Electrooxidation on Pd–CeO2/C in Passive and Active Polymer Electrolyte-Membrane Fuel Cells, ChemSusChem, 2012, 5, 1266-1273.

30. L. Wang, A. Lavacchi, M. Bevilacqua, M. Bellini, P. Fornasiero, J. Filippi, M. Innocenti, A. Marchionni, H. A. Miller and F. Vizza, Energy efficiency of alkaline direct ethanol fuel cells employing nanostructured palladium electrocatalysts, ChemCatChem, 2015, 7, 2214-2221.

31. Y. Chen, S. Ji, S. Zhao, W. Chen, J. Dong, W.-C. Cheong, R. Shen, X. Wen, L. Zheng and A. I. Rykov, Enhanced oxygen reduction with single-atomic-site iron catalysts for a zinc-air battery and hydrogen-air fuel cell, Nature communications, 2018, 9, 1-12.

32. H. S. Casalongue, S. Kaya, V. Viswanathan, D. J. Miller, D. Friebel, H. A. Hansen, J. K. Nørskov, A. Nilsson and H. Ogasawara, Direct observation of the oxygenated species during oxygen reduction on a platinum fuel cell cathode, Nature communications, 2013, 4, 1-6.

33 Jiang, H., Sun, J., Wei, L., Wu, M., Shyy, W. and Zhao, T. (2020). A high power density and long cycle life vanadium redox flow battery. Energy Stor. Mater. *24*, 529-540.

34 Sun, B. and Skyllas-Kazacos, M. (1992). Modification of graphite electrode materials for vanadium redox flow battery application—I. Thermal treatment. Electrochim. Acta 37, 1253-1260.

35 Zeng, L., Zhao, T. and Wei, L. (2018). Revealing the performance enhancement of oxygenated carbonaceous materials for vanadium redox flow batteries: functional groups or specific surface area? Adv. Sustain. Syst. 2, 1700148.

36 Mazúr, P., Mrlík, J., Beneš, J., Pocedič, J., Vrána, J., Dundálek, J. and Kosek, J. (2018). Performance evaluation of thermally treated graphite felt electrodes for vanadium redox flow battery and their four-point single cell characterization. J. Power Sources 380, 105-114.

37 Kil, D., Lee, H. J., Park, S., Kim, S. and Kim, H. (2017). Synthesis of activated graphite felts using short-term ozone/heat treatment for vanadium redox flow batteries. J. Electrochem. Soc. 164, A3011.

38 Kim, K. J., Kim, Y.-J., Kim, J.-H. and Park, M.-S. (2011). The effects of surface modification on carbon felt electrodes for use in vanadium redox flow batteries. Mater. Chem. Phys. 131, 547-553.

39 Kim, K. J., Park, M.-S., Kim, Y.-J., Kim, J. H., Dou, S. X. and Skyllas-Kazacos, M. (2015). A technology review of electrodes and reaction

mechanisms in vanadium redox flow batteries. J. Mater. Chem. A 3, 16913-16933.

40 Jiang, H., Shyy, W., Wu, M., Zhang, R. and Zhao, T. (2019). A bi-porous graphite felt electrode with enhanced surface area and catalytic activity for vanadium redox flow batteries. Appl. Energy 233, 105-113.

41 Castañeda, L. F., Walsh, F. C., Nava, J. L. and de Leon, C. P. (2017). Graphite felt as a versatile electrode material: Properties, reaction environment, performance and applications. Electrochim. Acta 258, 1115-1139.

42. T. Kadioglu, A. C. Turkmen, K. C. Ata, R. G. Akay, I. Tikiz and C. Celik, Investigation of the performance of a direct borohydride fuel cell with low Pt/C catalyst loading under different operating conditions, International Journal of Hydrogen Energy, 2020, 45, 35006-35012.

43. H. Gasteiger and S. Yan, Dependence of PEM fuel cell performance on catalyst loading, Journal of power sources, 2004, 127, 162-171.

44. Y.-H. Shih, G. V. Sagar and S. D. Lin, Effect of electrode Pt loading on the oxygen reduction reaction evaluated by rotating disk electrode and its implication on the reaction kinetics, The Journal of Physical Chemistry C, 2008, 112, 123-130.

45. S. Jeong, L.-H. Kim, Y. Kwon and S. Kim, Effect of nafion membrane thickness on performance of vanadium redox flow battery, Korean Journal of Chemical Engineering, 2014, 31, 2081-2087.

46. X. Shi, O. C. Esan, X. Huo, Y. Ma, Z. Pan, L. An and T. Zhao, Polymer Electrolyte Membranes for Vanadium Redox Flow Batteries: Fundamentals and Applications, Progress in Energy and Combustion Science, 2021, 85, 100926.

47. B. Jiang, L. Wu, L. Yu, X. Qiu and J. Xi, A comparative study of Nafion series membranes for vanadium redox flow batteries, Journal of Membrane Science, 2016, 510, 18-26.

48. D. Chen, M. A. Hickner, E. Agar and E. C. Kumbur, Optimizing membrane thickness for vanadium redox flow batteries, Journal of Membrane Science, 2013, 437, 108-113.

49. A. Chandan, M. Hattenberger, A. El-Kharouf, S. Du, A. Dhir, V. Self, B. G. Pollet, A. Ingram and W. Bujalski, High temperature (HT) polymer electrolyte membrane fuel cells (PEMFC)–A review, Journal of Power Sources, 2013, 231, 264-278.

50. Q. Wu, L. An, X. Yan and T. Zhao, Effects of design parameters on the performance of passive direct methanol fuel cells fed with concentrated fuel, Electrochimica Acta, 2014, 133, 8-15.

51. H. Xu, Y. Song, H. R. Kunz and J. M. Fenton, Effect of elevated temperature and reduced relative humidity on ORR kinetics for PEM fuel cells, Journal of the Electrochemical Society, 2005, 152, A1828.

52. S. Xiao, L. Yu, L. Wu, L. Liu, X. Qiu and J. Xi, Broad temperature adaptability of vanadium redox flow battery—Part 1: Electrolyte research,

Electrochimica Acta, 2016, 187, 525-534.

53. J. Xi, S. Xiao, L. Yu, L. Wu, L. Liu and X. Qiu, Broad temperature adaptability of vanadium redox flow battery—Part 2: Cell research, Electrochimica Acta, 2016, 191, 695-704.

54. L. An, T. Zhao, S. Shen, Q. Wu and R. Chen, Alkaline direct oxidation fuel cell with non-platinum catalysts capable of converting glucose to electricity at high power output, Journal of Power Sources, 2011, 196, 186-190.

55. P. Dimitrova, K. Friedrich, B. Vogt and U. Stimming, Transport properties of ionomer composite membranes for direct methanol fuel cells, Journal of Electroanalytical Chemistry, 2002, 532, 75-83.

56. G. G. Kumar, A. Kim, K. S. Nahm and R. Elizabeth, Nafion membranes modified with silica sulfuric acid for the elevated temperature and lower humidity operation of PEMFC, International Journal of Hydrogen Energy, 2009, 34, 9788-9794.

57. J. Peron, A. Mani, X. Zhao, D. Edwards, M. Adachi, T. Soboleva, Z. Shi, Z. Xie, T. Navessin and S. Holdcroft, Properties of Nafion® NR-211 membranes for PEMFCs, Journal of Membrane Science, 2010, 356, 44-51.

58. R. Badrinarayanan, J. Zhao, K. Tseng and M. Skyllas-Kazacos, Extended dynamic model for ion diffusion in all-vanadium redox flow battery including the effects of temperature and bulk electrolyte transfer, Journal of Power Sources, 2014, 270, 576-586.

59. Y. Cheng, H. Zhang, Q. Lai, X. Li, Q. Zheng, X. Xi and C. Ding, Effect of temperature on the performances and in situ polarization analysis of zinc–nickel single flow batteries, Journal of Power Sources, 2014, 249, 435-439.

60. S. Ma and E. Skou, CO2 permeability in Nafion® EW1100 at elevated temperature, Solid State Ionics, 2007, 178, 615-619.

61. M. S. Masdar, A. M. Zainoodin, M. I. Rosli, S. K. Kamarudin and W. R. W. Daud, Performance and stability of single and 6-cell stack passive direct methanol fuel cell (DMFC) for long-term operation, International Journal of Hydrogen Energy, 2017, 42, 9230-9242.

62. X. Zhou, T. Zhao, L. An, L. Wei and C. Zhang, The use of polybenzimidazole membranes in vanadium redox flow batteries leading to increased coulombic efficiency and cycling performance, Electrochimica Acta, 2015, 153, 492-498.

63. Y.-J. Chiu, An algebraic semi-empirical model for evaluating fuel crossover fluxes of a DMFC under various operating conditions, International Journal of Hydrogen Energy, 2010, 35, 6418-6430.

64 J. S. Kim, J. K. Yu, H. S. Lee, J. Y. Kim, Y. C. Kim, J. H. Han, I. H. Oh, and Y. W. Rhee, Effect of temperature, oxidant and catalyst loading on the performance of direct formic acid fuel cell, Korean Journal of Chemical Engineering, 2005, 22, 661-665.

65 L. Mu, W. Cheng, L. Zhi-Xiang, and M. Zong-Qiang, The development and performance analysis of all-China-made PEM fuel cell unit and 1 kW

level fuel cell stack, International Journal of Hydrogen Energy, 2012, 37, 1106-1111.

66 Y. Zeng, T. Zhao, L. An, X. Zhou, and L. Wei, A comparative study of all-vanadium and iron-chromium redox flow batteries for large-scale energy storage, Journal of Power Sources, 2015 300, 438-443.

67 Y. Wang, G. Liu, M. Wang, G. Liu, J. Li, and X. Wang, Study on stability of self-breathing DFMC with EIS method and three-electrode system, International Journal of Hydrogen Energy, 2013, 38, 9000-9007.

68 S. Song, G. Wang, W. Zhou, X. Zhao, G. Sun, Q. Xin, S. Kontou, and P. Tsiakaras, The effect of the MEA preparation procedure on both ethanol crossover and DEFC performance, Journal of Power Sources, 2005, 140, 103-110.

Table

Table 3-1. Cost comparison of conventional direct liquid fuel cell and direct e-fuel cell.

	Cathode (USD m^{-2})	Membrane (USD m^{-2})	Anode (USD m^{-2})	MEA (USD m^{-2})	PPD (mW cm^{-2})	Cost per unit power (USD kW^{-1})	Ref.
Formic acid	$ 16017 Pt black (7 mg cm^{-2})	$ 500 Nafion series	$ 11147 Pt-Ru black (4 mg cm^{-2})	$ 27664	48.51	$ 57027.42	64-66
Methanol	$ 9171 Pt black (4 mg cm^{-2})	$ 500 Nafion series	$ 11147 Pt-Ru black (4 mg cm^{-2})	$ 20818	20.1	$ 103572.14	65-67
Ethanol	$ 6889 Pt black (3 mg cm^{-2})	$ 500 Nafion series	$ 8371 Pt-Ru black (3 mg cm^{-2})	$ 15760	29.9	$ 52709.03	65, 66, 68
E-fuel	$ 10457.36 Pt/C 60% (4.0 mg cm^{-2})	$ 500 Nafion series	$ 70 Graphite felt	$ 11027.36	857	$ 1286.74	65, 66

MEA: Membrane electrode assembly;

PPD: Peak power density.

Chapter 4 Performance characteristics of a passive fuel cell

4.1 Introduction

As a result of the increasing needs of renewable energy, the development of sustainable power generation systems has become a major research direction and drawn world-wide attention. In comparison to other existing technologies, fuel cell technology has been acknowledged as a promising candidate and utilized in numerous applications including electric vehicles, mobile devices, and even power stations. [1-3] Among the various types of fuel cell, direct liquid fuel cells attributed to their high energy density and ease of fuel handling, have been extensively studied. [4-5] Nevertheless, to realize the commercialization of direct liquid fuel cells, especially in small devices such as mobile phones and laptops, it is necessary to minimize or completely eliminate auxiliary equipment such as pumps, air blowers, and heat controllers from the system. [6-8] Passive fuel cells, using diffusion and natural convection for fuel delivery, have therefore received extensive studies in recent years. [9-10] However, as a result of the slow reaction kinetics of conventional liquid fuels, poor performance, such as lower peak power density than the typical active liquid fuel cells, is a major limitation of these passive liquid fuel cells. [11-12] To boost the performances of passive liquid fuel cells, it is thus of paramount importance to explore alternative fuels with better reactivity.

Recently, a novel concept named the electrically rechargeable liquid fuel (e-fuel), which possesses many advantages such as rechargeability and superior reactivity over the conventional liquid alcohol fuels, was presented. [13-16] Herein, drawn by the superiorities of the e-fuel, a passive fuel cell has been designed and fabricated utilizing the liquid e-fuel and paired with the ambient air for electricity production. This passive fuel cell using the liquid e-fuel impressively results in a peak power density of 116.2 mW cm^{-2} along with a stable operation for over 350 hours, which therefore place it as a promising candidate with great prospects to realize future applications.

4.2 Working Principle

The passive fuel cell structure (Figure 4.1) includes a membrane electrode assembly (MEA), an e-fuel tank, a pair of current collectors and endplates. During the cell operation, the V^{2+} ions in the e-fuel are oxidized to V^{3+} ions at the anode side, while the oxygen reduction reaction (ORR) occurs at the cathode side. The overall reaction is thus given as:

$$V^{2+} + H^+ + \frac{1}{4}O_2 \rightarrow V^{3+} + \frac{1}{2}H_2O \qquad \Delta E = 1.49\ V \qquad (1)$$

The theoretical voltage of this system is 1.49 V, [14] which is higher than those of many common direct alcohol fuel cells.

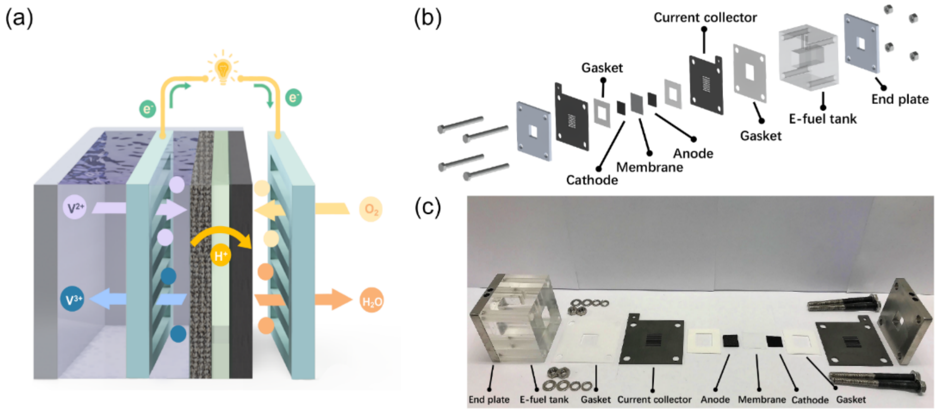

Figure 4.1 (a) Working principle, (b) design, and (c) fabrication of a passive fuel cell.

4.3 Experiments

4.3.1 Preparation of MEA

The MEA of this passive fuel cell (2.0 × 2.0 cm^2) was fabricated following the method reported before, [14] where a thermally treated graphite felt and a Pt/C coated carbon paper (2.0 mg cm^{-2}) was used as anode and cathode, respectively. [14] Nafion 117 pretreated following the standard procedure reported previously was used as proton exchange membrane in the middle of the MEA. [14]

4.3.2 Cell assembly and experimental apparatus

The passive fuel cell system consisting of an e-fuel tank and a pair of current collectors and end plates was fabricated. The home-made e-fuel tank was prepared using acrylic with two holes drilled on its top for e-fuel injection. Deionized water was sprayed onto the cathode to pre-humidify the electrode surface while 20.0 mL e-fuel to be supplied into the cell was injected into the tank before further tests. Five current collectors (CCs) with different designs and open ratios (ORs) were fabricated using graphite, namely CC1 to CC5. Among them, CC1 and CC2 adopted the circular perforation design, while CC3 to CC5 adopted the rectangular parallel channels design. [9] The OR of each current collector from CC1 to CC5 is 25.97%, 28.27%, 35.00%, 50.00%, and 70.00%, respectively. In addition, a transparent fuel cell with an acrylic end plate and a graphite current collector engraved with a serpentine flow filed was also fabricated to enable the visualization of the gas evolution process at the anode. For the transparent fuel cell, a peristaltic pump was used for the e-fuel delivery at ~5.0 mL min^{-1}, while the cell is under open circuit condition during the test.

The polarization and long-term discharge tests were performed using an Arbin BT2000 (Arbin instrument Inc.). All experiments were conducted at ambient condition. For the long-term operation behavior test, the Faradic, voltage and energy efficiencies are calculated using the following equations [15]:

$$\text{Faradic efficiency (\%)} = \frac{\int i(t)dt}{c_{init}VF} \tag{1}$$

$$\text{Voltage efficiency (\%)} = \frac{E_{aver}}{E_{theo}} = \frac{E_{aver}}{\frac{\int_0^{\mathrm{c_{init}}}[\mathrm{E^0} + \frac{\mathrm{RT}}{\mathrm{F}}\ln(\frac{\mathrm{c_{V^{2+}}}}{\mathrm{c_{V^{3+}}}})]\mathrm{dc}}{\mathrm{c_{init}}}} \tag{2}$$

$$\text{Energy efficiency (\%)} = \text{Faradic efficiency} \times \text{Voltage efficiency} \tag{3}$$

$i(t)$ is the discharging current, while c_{init} and V represents the initial concentration of e-fuel and volume of e-fuel, respectively. E_{aver} and $E_{theo}$is the average discharging voltage and theoretical average voltage calculated based on the Nernst equation, respectively.

4.4 Results and discussion

4.4.1 General performance

The general performance of this developed passive fuel cell is as depicted in Figure 4.2 (a), where the cell is assembled with CC5 and using an e-fuel of 1.0 M V^{2+} ions. The cell is found to achieve an open-circuit voltage (OCV) of 1.29 V with a peak power density of 116.2 mW cm^{-2}. It is worth to mention that, during the operation of this passive fuel cell, the V^{2+} ions would inevitably transport through the membrane to the cathode side, which thereby leads to a mixed potential due to the simultaneous oxygen reduction reaction and vanadium oxidation reaction and hence resulted in the potential loss. [14] However, when compared with the conventional passive and active liquid fuel cells reported before, as shown in Figure 4.2 (b) and Table 4-1, [29-49] this passive fuel cell utilizing the e-fuel is found to demonstrate a much higher peak power density. Such an outstanding cell performance is ascribed to the superior reactivity of the e-fuel at room temperature along with the optimized current collector design which allows the ease of e-fuel delivery. Hence, it is considered that this passive fuel cell fed with the e-fuel possesses great potential for future applications.

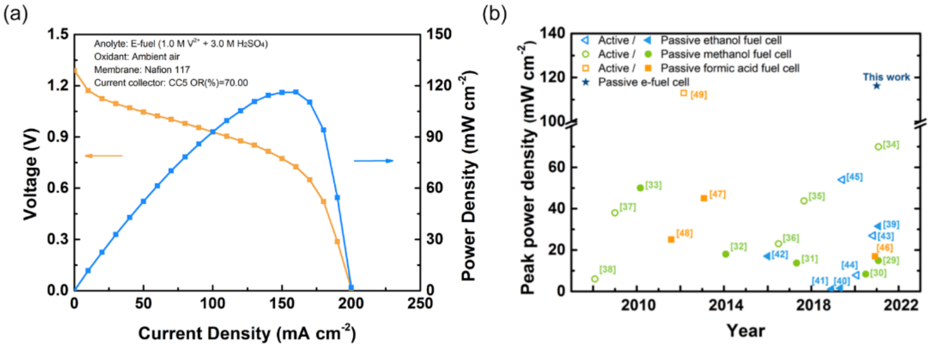

Figure 4.2 (a) General performance of a passive fuel cell; (b) Comparison of the peak power density of the passive fuel cell with the data available in the open literature.

4.4.2 Effect of the current collector design

As one of the main components of a passive fuel cell, the current collector (CC) plays multiple roles during the cell operation, which include allowing the conduction of electrons between the electrode surface and the external circuit, providing the pathways for the fuel delivery and products removal as well as giving support to the electrode. [17] It is hence essential for the current collector to have superior electric conductivity and ease of fuel transport. [9] In this work, five CCs with various opening patterns and ratios are designed and fabricated to optimize the cell performance. As shown in Figure 4.3, CC1 and CC2 adopted the circular perforation design, while CCs 3-5 adopted the rectangular parallel channels design. [9]

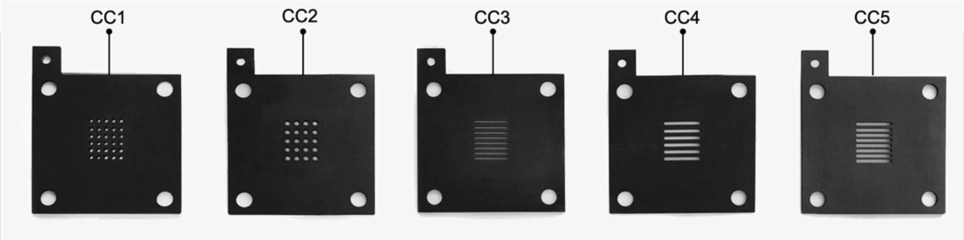

Figure 4.3 Designs of five current collectors.

All the CCs are assembled into the passive fuel cell to conduct the polarization tests and the results are as presented in Figure 4.4. It can be seen that, feeding the cell with an e-fuel of 0.6 M V^{2+} ions, both the maximum current density and the peak power density of the cell raise with the increment of the CC open ratio. In addition, the concentration loss at the end of the polarization curve is found to decrease in this order. Such result is due to the fact that, a higher open ratio of CC can provide larger pathways for fuel supply, which thereby facilitate the transport of both oxygen and the e-fuel. [17] However, it is worth noticing that allowing a higher reactant contact area through a CC of high open ratio could on the other hand lead to a high interfacial ohmic loss due to the sacrificed electric contact area for electrons transport, which can eventually limit the cell performance. [17] Still, overall, CC5 with its highest open ratio achieved the best performance among all the CCs tested and is therefore chosen and used for further studies in this work.

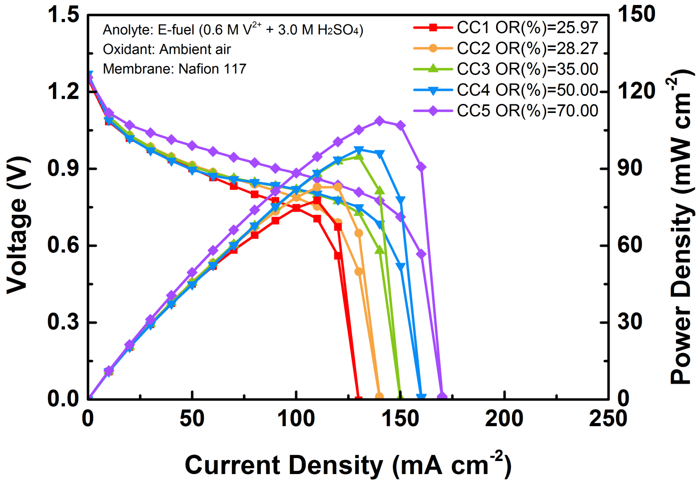

Figure 4.4 Polarization and power density curves of this passive fuel cell with different designs.

4.4.3 Effect of the e-fuel composition

As mentioned, the passive fuel cell only utilizes natural diffusion and convection for fuel delivery. [10] Hence, for a given cell design, the concentration of fuel in the tank is a major variable with significant influence on the mass transport of reactants and the availability of sufficient reactants to the reactive surface, which is of paramount importance towards determining the cell performance. [18] Here, in order to examine the effects of the e-fuel concentration on the cell performance, the liquid e-fuel with V^{2+} ions concentration varying from 0.2 M to 1.0 M are studied. As shown in Figure 4.5, the activation and concentration losses of the cell are found to reduce effectively with the increase of e-fuel concentration. It is because the high concentration of reactive species can lead to a raise of the fuel concentration gradient between the tank and electrode surface, which thereby results in an enhanced mass transport. [18] This improved e-fuel delivery thereby can help to provide more reactive species to the anode and hence promote the e-fuel oxidation reaction, leading to a better cell performance. However, it should also be noted that the usage of e-fuel with higher concentration would on the other hand promote the crossover of V^{2+} ions through the membrane and thereby lead to the loss of fuel. [19] Furthermore, the permeated V^{2+} ions to the cathode side can also result in a mixed potential due to the simultaneous e-fuel oxidation and oxygen reduction reactions, which can further deteriorate the cell performance.

[14,20]

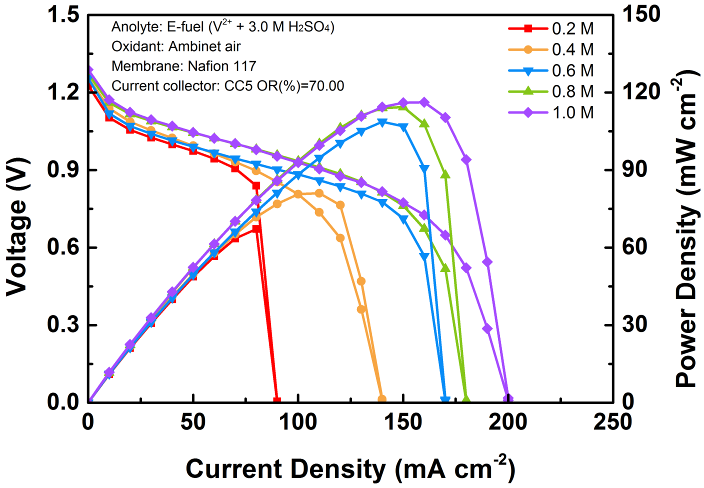

Figure 4.5 Polarization and power density curves of this passive fuel cell with various e-fuel concentrations.

4.4.4 Long-term operation behavior

It is a crucial requirement for the passive fuel cell to attain a superior long-term stability before realizing its wide commercialization. Here, to study the long-term operation behavior of this system, the passive fuel cell has been tested at 5.0 mA cm^{-2} and refueled for 25 times. The discharge curves are as shown in Figure 4.6 (a), while the associated efficiencies - Faradic, voltage, and energy efficiencies are calculated using the equations as reported before [15] and as shown in Figure 4.6 (b). The cell is found to achieve a stable operation for over 350 hours, with little difference between the discharge curves obtained at the first and last cycle, indicating the excellent long-term stability of this system. It is also found that, in comparison to the discharge curve obtained at the first cycle, the cell voltage at the last cycle is slightly lower. Such a phenomenon may be ascribed to the crossover of reactive species across the membrane inducing the accumulation of vanadium ions at the cathode side, which thereby block the reactive surface of the catalysts and enlarges overpotential loss. [14-15, 21] Furthermore, it is worth mentioning that, an unexpected gas evolution phenomenon was observed at the anode side during the test, which can also obstruct the reactive surface at the anode and hamper the mass transport of reactants, resulting in the fluctuation of cell voltage as demonstrated in the discharge curves. [22-23] This phenomenon is later proved as a spontaneous hydrogen evolution reaction and discussed extensively in the next section. Such a reaction accompanied with the inevitable crossover of e-fuel through the membrane would result in the loss of reactive species, which thereby lead to the loss of Faradic efficiency and further reduces the energy efficiency of the cell. Overall, this present passive cell is found to achieve a stable energy efficiency of ~40% during the 25 times of refueling tests, demonstrating its superior capability for long-term operation.

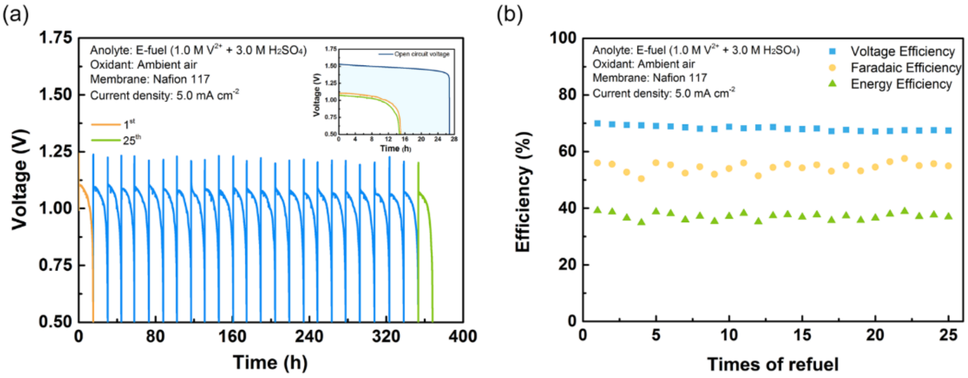

Figure 4.6 (a) Long-term discharging behavior and comparison of the 1st and 25th discharging curves of this passive fuel cell (insert). (b) The Faradic, voltage, and energy efficiencies of this passive fuel cell.

4.4.5 Visualization of anode flow channels

As discussed in the previous section, during the long-term operation of this passive fuel cell, an unexpected gas evolution phenomenon is observed at its anode side, which limits the transport of the reactants and deteriorates the cell performance. [21] In order to further observe and examine this phenomenon, a transparent cell is designed and fabricated as shown in Figure 4.7, where a new graphite current collector engraved with a serpentine flow field is fabricated and used as the anode current collector while CC5 is used at the cathode side.

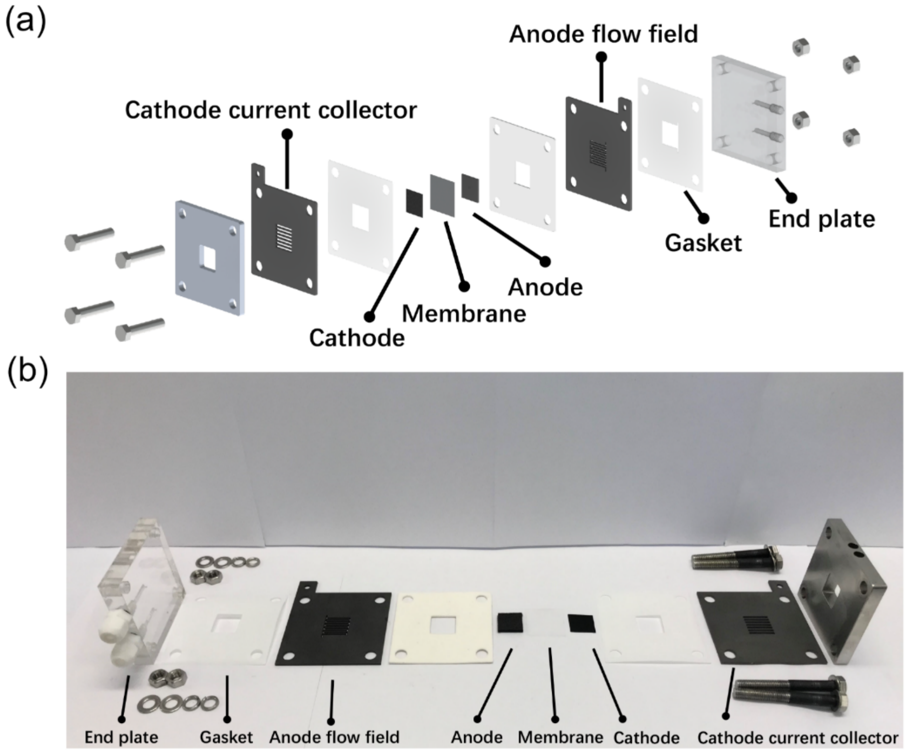

Figure 4.7 (a) Design and (b) fabrication of a fuel cell with a transparent anode flow field.

This transparent cell is assembled three times using the same MEA used for the previous tests, a used graphite felt, and a fresh graphite felt, respectively. Four different solutions, including 3.0 M H_2SO_4, and 1.0 M $VO^{2+}/V^{3+}/V^{2+}$ in 3.0 M H_2SO_4, are fed into the anode side of the cell and the results are as shown in Figure 4.8. Gas evolution was only observed when the e-fuel of 1.0 M V^{2+} is used (Figure 4.8), which thereby indicate the occurrence of a spontaneous gas evolution reaction.

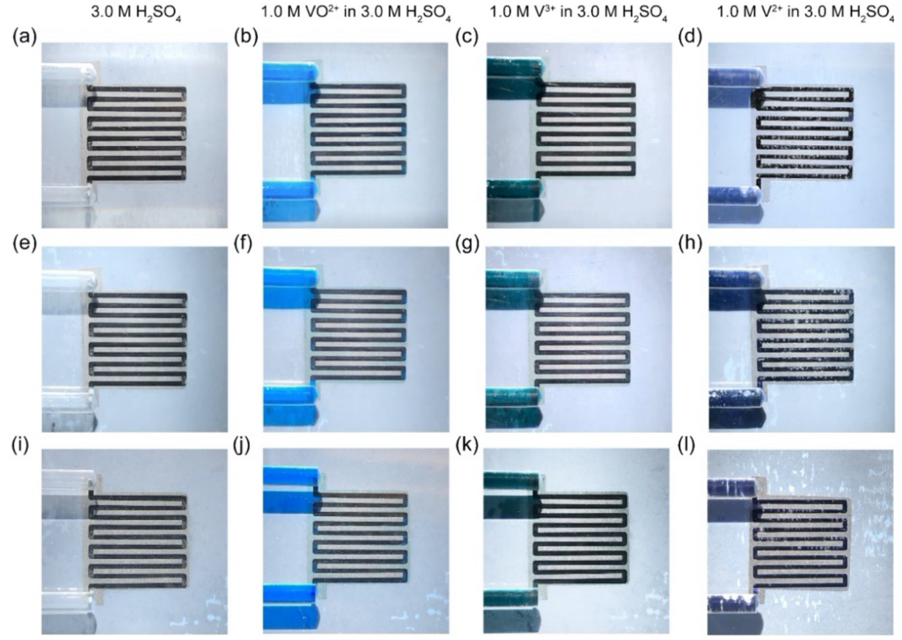

Figure 4.8 Visualization of the anode flow channels with (a-d) complete MEA, (e-h) used and (i-l) fresh thermally treated graphite felt anode.

Considering the superior reactivity of V^{2+} ions, even without any catalyst, the following reaction as reported before might have happened, [24-25] which results in a hydrogen generation process:

$$V^{2+} + H^{+} \rightarrow V^{3+} + \frac{1}{2}H_2 \tag{2}$$

To prove and justify this idea, the generated gas is then collected from the outlet of the transparent cell by water displacement method and then fed into a typical hydrogen-oxygen fuel cell, which results in an OCV of 1.11 V (Figure 4.9) similar to the value obtained when this cell is fed with pure hydrogen, thereby proving the presence of a spontaneous hydrogen evolution reaction (HER) at the anode side. It is worth to mention that, during the visualization tests, a similar gas evolution phenomenon is observed in the cell using the used MEA and the used graphite felt, while a less severe gas generation process is observed when the fresh thermally treated graphite felt anode is tested (Figure 4.8). [24] Such a phenomenon is considered to be attributed to the superior catalytic reactivity of Pt, which penetrate from the cathode side across the membrane after the cell operation. [26-27] It is also worth to stress that, this spontaneous HER should be regarded with great importance in this passive fuel cell system as it could severely deteriorate the cell performance from the following aspects: i) the HER can occupy the reactive surface on the anode and lead to large overpotential loss; [28] ii) this HER will consume the reactive species and lead to fuel capacity loss; and iii) the generated hydrogen gas can hamper the mass transport of the fuel and results in large mass transport polarization. [21] Moreover, in the future, for the fuel cell at industrial-scale, such HER may also raise safety concerns and thus may require proper ventilation system to avoid any fire or explosion hazards. It is therefore a critical consideration to develop an electrode of good reactivity to the e-fuel oxidation reaction while suppressing the spontaneous HER so as to gain a better cell performance. In addition, it is also essential to prevent any potential contamination from the environment during the cell assembling and develop a membrane that can efficiently suppress the transport of catalyst from the cathode side so as to attain a more stable cell performance. Other potential strategies including: i) using the fuel with lower V^{2+} and H^+ concentrations to slow down the reaction kinetics; and ii) developing selective catalysts or adding additives which can suppress the HER; may also help suppress this undesired HER.

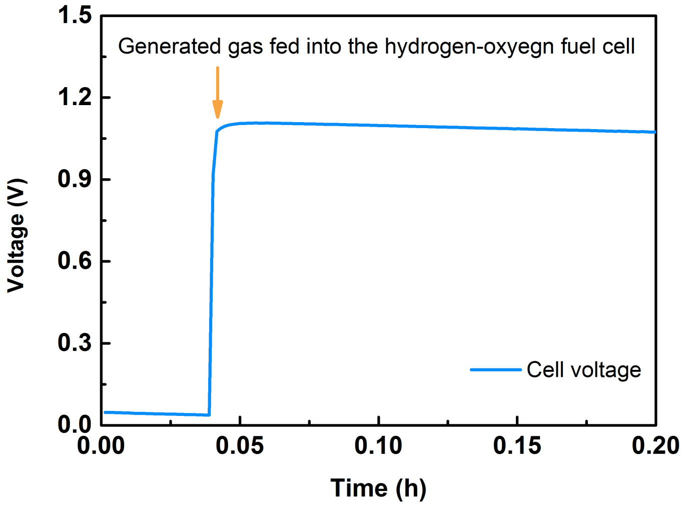

Figure 4.9 Voltage profile of the hydrogen-oxygen fuel cell fed with the generated gas from the anode side of the passive fuel cell.

4.5 Summary

In this work, a passive fuel cell utilizing the liquid e-fuel and ambient air for power generation is designed and fabricated. It is found that both the current collector open ratios and e-fuel compositions show a major effect on the transport of reactant inside the cell, which thereby greatly influences the cell performance. The cell remarkably demonstrates a peak power density of 116.2 mW cm^{-2} along with a stable operation for over 350 hours, which even outperforms many conventional active liquid fuel cells. Such a superior performance therefore validates the capability of this developed passive fuel cell for wide-spread application in the future especially for powering mobile devices. However, it is also found that a spontaneous hydrogen evolution reaction happens at the anode, which would decrease the e-fuel capacity and further deteriorate the cell performance. It is thus believed that further performance enhancement of this passive fuel cell can be achieved in the future with the development of electrode with superior reactivity to the e-fuel while also suppressing the undesired hydrogen evolution reaction. Water flooding, which is another critical issue responsible for limiting the performance of this passive fuel cell, also needs to be addressed as it can hamper the delivery of oxygen and thereby deteriorate the reaction kinetics at the cathode side. It is therefore essential to investigate the influences of water flooding on the cell performance and develop a suitable membrane and electrode to attain a better cell performance in the future.

4.6 References

1. Wang, Y.-J.; Qiao, J.; Baker, R.; Zhang, J., Alkaline Polymer Electrolyte Membranes for Fuel Cell Applications. Chemical Society Reviews 2013, 42 (13), 5768-5787.

2. Laberty-Robert, C.; Valle, K.; Pereira, F.; Sanchez, C., Design and Properties of Functional Hybrid Organic–Inorganic Membranes for Fuel Cells. Chemical Society Reviews 2011, 40 (2), 961-1005.

3. Yuan, X.; Ding, X.-L.; Wang, C.-Y.; Ma, Z.-F., Use of Polypyrrole in Catalysts for Low Temperature Fuel Cells. Energy & Environmental Science 2013, 6 (4), 1105-1124.

4. Antolini, E., Palladium in Fuel Cell Catalysis. Energy & Environmental Science 2009, 2 (9), 915-931.

5. Tadanaga, K.; Furukawa, Y.; Hayashi, A.; Tatsumisago, M., Direct Ethanol Fuel Cell Using Hydrotalcite Clay as a Hydroxide Ion Conductive Electrolyte. Advanced Materials 2010, 22 (39), 4401-4404.

6. Zhao, T.; Chen, R.; Yang, W.; Xu, C., Small Direct Methanol Fuel Cells with Passive Supply of Reactants. Journal of Power Sources 2009, 191 (2), 185-202.

7. Pan, Z.; Bi, Y.; An, L., Performance Characteristics of a Passive Direct Ethylene Glycol Fuel Cell with Hydrogen Peroxide as Oxidant. Applied Energy 2019, 250, 846-854.

8. Oliveira, V.; Pereira, J.; Pinto, A., Modeling of Passive Direct Ethanol

Fuel Cells. Energy 2017, 133, 652-665.

9. Mallick, R. K.; Thombre, S. B.; Shrivastava, N. K., A Critical Review of the Current Collector for Passive Direct Methanol Fuel Cells. Journal of Power Sources 2015, 285, 510-529.

10. Munjewar, S. S.; Thombre, S. B.; Mallick, R. K., Approaches to Overcome the Barrier Issues of Passive Direct Methanol Fuel Cell–Review. Renewable and Sustainable Energy Reviews 2017, 67, 1087-1104.

11. Wang, Z.; Zhang, X.; Nie, L.; Zhang, Y.; Liu, X., Elimination of Water Flooding of Cathode Current Collector of Micro Passive Direct Methanol Fuel Cell by Superhydrophilic Surface Treatment. Applied Energy 2014, 126, 107-112.

12. Munjewar, S. S.; Thombre, S. B.; Patil, A. P., Passive Direct Alcohol Fuel Cell Using Methanol and 2-Propanol Mixture as a Fuel. Ionics 2019, 25 (5), 2231-2241.

13. Jiang, H.; Wei, L.; Fan, X.; Xu, J.; Shyy, W.; Zhao, T., A Novel Energy Storage System Incorporating Electrically Rechargeable Liquid Fuels as the Storage Medium. Science Bulletin 2019, 64 (4), 270-280.

14. Shi, X.; Huo, X.; Ma, Y.; Pan, Z.; An, L., Energizing Fuel Cells with an Electrically Rechargeable Liquid Fuel. Cell Reports Physical Science 2020, 1 (7), 100102.

15. Shi, X.; Huo, X.; Esan, O. C.; An, L.; Zhao, T., Performance Characteristics of a Liquid E-fuel Cell. Applied Energy 2021, 297, 117145.

16. Shi, X.; Huo, X.; Esan, O. C.; Ma, Y.; An, L.; Zhao, T., A Liquid E-fuel Cell Operating at −20° C. Journal of Power Sources 2021, 506, 230198.

17. Braz, B.; Moreira, C.; Oliveira, V.; Pinto, A., Effect of the Current Collector Design on the Performance of a Passive Direct Methanol Fuel Cell. Electrochimica Acta 2019, 300, 306-315.

18. Liu, J.; Zhao, T.; Chen, R.; Wong, C., The Effect of Methanol Concentration on the Performance of a Passive DMFC. Electrochemistry Communications 2005, 7 (3), 288-294.

19. Hao, L.; Wang, Y.; He, Y., Modeling of Ion Crossover in an All-vanadium Redox Flow Battery with the Interfacial Effect at Membrane/Electrode Interfaces. Journal of The Electrochemical Society 2019, 166 (8), A1310-A1322.

20. Pereira, J.; Falcão, D.; Oliveira, V.; Pinto, A., Performance of a Passive Direct Ethanol Fuel Cell. Journal of Power Sources 2014, 256, 14-19.

21. Wei, L.; Zhao, T.; Xu, Q.; Zhou, X.; Zhang, Z., In-situ Investigation of Hydrogen Evolution Behavior in Vanadium Redox Flow Batteries. Applied Energy 2017, 190, 1112-1118.

22. Noack, J.; Cognard, G.; Oral, M.; Küttinger, M.; Roznyatovskaya, N.; Pinkwart, K.; Tübke, J., Study of the Long-term Operation of a Vanadium/Oxygen Fuel Cell. Journal of Power Sources 2016, 326, 137-145.

23. Liu, B.; Li, Z.; Zhu, J.; Suda, S., Influences of Hydrogen Evolution on the Cell and Stack Performances of the Direct Borohydride Fuel Cell.

Journal of Power Sources 2008, 183 (1), 151-156.

24. Sun, C.-N.; Delnick, F. M.; Baggetto, L.; Veith, G. M.; Zawodzinski Jr, T. A., Hydrogen evolution at the negative electrode of the all-vanadium redox flow batteries. Journal of Power Sources 2014, 248, 560-564.

25. Peljo, P.; Vrubel, H.; Amstutz, V.; Pandard, J.; Morgado, J.; Santasalo-Aarnio, A.; Lloyd, D.; Gumy, F.; Dennison, C.; Toghill, K. E., All-vanadium dual circuit redox flow battery for renewable hydrogen generation and desulfurisation. Green Chemistry 2016, 18 (6), 1785-1797.

26. Guilminot, E.; Corcella, A.; Charlot, F.; Maillard, F.; Chatenet, M., Detection of Pt z+ ions and Pt nanoparticles inside the membrane of a used PEMFC. Journal of The Electrochemical Society 2006, 154 (1), B96.

27. Akita, T.; Taniguchi, A.; Maekawa, J.; Siroma, Z.; Tanaka, K.; Kohyama, M.; Yasuda, K., Analytical TEM study of Pt particle deposition in the proton-exchange membrane of a membrane-electrode-assembly. Journal of Power Sources 2006, 159 (1), 461-467.

28. Chen, F.; Liu, J.; Chen, H.; Yan, C., Study on Hydrogen Evolution Reaction at a Graphite Electrode in the All-vanadium Redox Flow Battery. Int. J. Electrochem. Sci 2012, 7 (4), 3750-3764.

29. Wang, L.; Yin, L.; Yang, W.; Cheng, Y.; Wen, F.; Liu, C.; Dong, L.; Wang, M.; Ma, S.; Feng, X., Evaluation of Structural Aspects and Operation Environments on the Performance of Passive Micro Direct Methanol Fuel Cell. International Journal of Hydrogen Energy 2021, 46 (2), 2594-2605.

30. Zakaria, Z.; Kamarudin, S. K., Evaluation of Quaternized Polyvinyl Alcohol/Graphene Oxide-based Membrane Towards Improving the Performance of Air-breathing Passive Direct Methanol Fuel Cells. International Journal of Energy Research 2020, 44 (11), 8988-9000.

31. Ong, B.; Kamarudin, S.; Masdar, M.; Hasran, U., Applications of Graphene Nano-sheets as Anode Diffusion Layers in Passive Direct Methanol Fuel Cells (DMFC). International Journal of Hydrogen Energy 2017, 42 (14), 9252-9261.

32. Yuan, T.; Pu, L.; Huang, Q.; Zhang, H.; Li, X.; Yang, H., An Effective Methanol-blocking Membrane Modified with Graphene Oxide Nanosheets for Passive Direct Methanol Fuel Cells. Electrochimica Acta 2014, 117, 393-397.

33. Xu, C.; Faghri, A.; Li, X.; Ward, T., Methanol and Water Crossover in a Passive Liquid-feed Direct Methanol Fuel Cell. International Journal of Hydrogen Energy 2010, 35 (4), 1769-1777.

34. Li, X.; Miao, Z.; Marten, L.; Blankenau, I., Experimental Measurements of Fuel and Water Crossover in an Active DMFC. International Journal of Hydrogen Energy 2021, 46 (5), 4437-4446.

35. Ercelik, M.; Ozden, A.; Seker, E.; Colpan, C. O., Characterization and Performance Evaluation of PtRu/CTiO2 Anode Electrocatalyst for DMFC Applications. International Journal of Hydrogen Energy 2017, 42 (33), 21518-21529.

36. Al-Batty, S.; Dawson, C.; Shanmukham, S.; Roberts, E.; Holmes, S., Improvement of Direct Methanol Fuel Cell Performance Using a Novel Mordenite Barrier Layer. Journal of Materials Chemistry A 2016, 4 (28), 10850-10857.

37. Fujiwara, N.; Siroma, Z.; Yamazaki, S.-i.; Ioroi, T.; Senoh, H.; Yasuda, K., Direct Ethanol Fuel Cells Using an Anion Exchange Membrane. Journal of Power Sources 2008, 185 (2), 621-626.

38. Scott, K.; Yu, E.; Vlachogiannopoulos, G.; Shivare, M.; Duteanu, N., Performance of a Direct Methanol Alkaline Membrane Fuel Cell. Journal of Power Sources 2008, 175 (1), 452-457.

39. Kakaei, K.; Rahnavardi, M., Synthesis of Nitrogen-doped Reduced Graphene Oxide and Its Decoration with High Efficiency Palladium Nanoparticles for Direct Ethanol Fuel Cell. Renewable Energy 2021, 163, 1277-1286.

40. Shaari, N.; Kamarudin, S. K.; Zakaria, Z., Enhanced Alkaline Stability and Performance of Alkali-doped Quaternized Poly (vinyl alcohol) Membranes for Passive Direct Ethanol Fuel Cell. International Journal of Energy Research 2019, 43 (10), 5252-5265.

41. Shrivastava, N. K.; Chadge, R. B.; Ahire, P.; Giri, J. P., Experimental Investigation of a Passive Direct Ethanol Fuel Cell. Ionics 2019, 25 (2), 719-726.

42. Modibedi, R. M.; Mehlo, T.; Ozoemena, K. I.; Mathe, M. K.,

Preparation, Characterisation and Application of Pd/C Nanocatalyst in Passive Alkaline Direct Ethanol Fuel Cells (ADEFC). International Journal of Hydrogen Energy 2015, 40 (45), 15605-15612.

43. Pinheiro, V. S.; Souza, F. M.; Gentil, T. C.; Nascimento, A. N.; Böhnstedt, P.; Parreira, L. S.; Paz, E. C.; Hammer, P.; Sairre, M. I.; Batista, B. L., Sn-containing Electrocatalysts with a Reduced Amount of Palladium for Alkaline Direct Ethanol Fuel Cell Applications. Renewable Energy 2020, 158, 49-63.

44. Choudhary, A. K.; Pramanik, H., Enhancement of Ethanol Electrooxidation in Half Cell and Single Direct Ethanol Fuel Cell (DEFC) Using Post-treated Polyol Synthesized Pt-Ru Nano Electrocatalysts Supported on HNO3-functionalized Acetylene Black Carbon. International Journal of Hydrogen Energy 2020, 45 (1), 574-594.

45. Sun, X.; Li, Y.; Li, M.-J., Highly Dispersed Palladium Nanoparticles on Carbon-decorated Porous Nickel Electrode: An Effective Strategy to Boost Direct Ethanol Fuel Cell up to 202 mW cm–2. ACS Sustainable Chemistry & Engineering 2019, 7 (13), 11186-11193.

46. Nogalska, A.; Navarro, A. B.; Garcia-Valls, R., MEA Preparation for Direct Formate/Formic Acid Fuel Cell—Comparison of Palladium Black and Palladium Supported on Activated Carbon Performance on Power Generation in Passive Fuel Cell. Membranes 2020, 10 (11), 355.

47. Cai, W.; Liang, L.; Zhang, Y.; Xing, W.; Liu, C., Real Contribution of

Formic Acid in Direct Formic Acid Fuel Cell: Investigation of Origin and Guiding for Micro Structure Design. International Journal of Hydrogen Energy 2013, 38 (1), 212-218.

48. Hong, P.; Luo, F.; Liao, S.; Zeng, J., Effects of Pt/C, Pd/C and PdPt/C Anode Catalysts on the Performance and Stability of Air Breathing Direct Formic Acid Fuel Cells. International Journal of Hydrogen Energy 2011, 36 (14), 8518-8524.

49. Bauskar, A. S.; Rice, C. A., Impact of Anode Catalyst Layer Porosity on the Performance of a Direct Formic Acid Fuel Cell. Electrochimica Acta 2012, 62, 36-41.

Table

Table 4-1. Comparison of power densities among various liquid fuel cells.

Fuel	**Type**	**Year**	**Anode catalyst**	**Membrane**	**Temp (˚C)**	**Peak Power Density (mW cm^{-2})**	**Ref**
MeOH	Passive	2021	Pt-Ru (2.0 mg cm^{-2})	Nafion 117	25	14.91	[29]
		2020	Pt-Ru (2.0 mg cm^{-2})	Nafion 117	30	8.36	[30]
		2017	Pt–Ru black (8.0 mg cm^{-2})	Nafion 117	RT	13.7	[31]
		2014	Pt–Ru black (4.0 mg cm^{-2})	Nafion 212	RT	18	[32]
		2010	Pt-Ru (5.0 mg cm^{-2})	Nafion 115	22~24	50	[33]
	Active	2020	Pt：Ru (3.0:1.5 mg cm^{-2})	Nafion 115	60	69.94	[34]
		2017	Pt-Ru/C-TiO_2 (4.0 mg cm^{-2})	Nafion 115	45	43.75	[35]
		2016	Pt-Ru/Vulcan XC-72 (1.0 mg cm^{-2})	Nafion 117	40	~23	[36]
		2008	PtRu black (3.0 mg cm^{-2})	Nafion 117	RT	38	[37]
		2008	Pt-Ru/C (1.0 mg cm^{-2})	Morgane® -ADP	30	~6	[38]
EtOH	Passive	2021	Pd/NRGO (1.0 mg cm^{-2})	A-006	RT	31.5	[39]
		2019	Pt-Ru (2.0 mg cm^{-2})	Nafion 117	30	1.54	[40]
		2018	Pt-Ru/C (4.0 mg cm^{-2})	Nafion 115	22~25	~1.10	[41]
		2015	Pd (1.7 mg cm^{-2})	A-006	25	17	[42]
	Active	2020	Pd_1Sn_3/Vulcan XC-72 (1.0 mg cm^{-2})	Nafion 117	40	~27	[43]
		2020	Pt-Ru/C (1.0 mg cm^{-2})	Nafion 117	40	7.86	[44]
		2019	Pd (5.0 mg cm^{-2})	A201	20	54	[45]
Formic acid	Passive	2020	Pd/C (1.0 mg cm^{-2})	Nafion 117	25	16.99	[46]
		2013	Pd/C (4.0 mg cm^{-2})	Nafion 117	RT	45	[47]
		2011	Pd/C (1.0 mg cm^{-2})	Nafion 212	RT	25.1	[48]
	Active	2012	Pt/Ru black (9.0 mg cm^{-2})	Nafion 115	40	113	[49]
E-fuel	Passive	2021	/	Nafion 117	RT	116.23	This work

Chapter 5 Design and development of an all-climate liquid fuel cell

5.1 Introduction

Concerns over the energy crisis and environmental impacts of using fossil fuels have attracted an increasing attention towards the development of clean and sustainable power generation as well as energy storage systems. [1-3] Among the various advanced power generation systems, hydrogen fuel cells, with their compact structure and high energy density, are considered as one of the most promising candidates for various applications, as well as gradual acceptance in the transportation sector to power future electric vehicles, [4,5] i.e., fuel cell electric vehicles (FCEVs). However, after several decades of investigations and commercialization, their widespread application, in terms of market presence and penetration, is still being hindered by the various difficulties and safety issues mostly pertaining to the problematic handling of gaseous hydrogen. [6,7] Alternatively, liquid fuel cells, typically using liquid alcohol fuels, have drawn worldwide attention owing to their high energy density, inbuilt safety, and ease of fuel handling. Although promising, some critical engineering issues, including low energy efficiency and power density of these conventional direct liquid fuel cells still need to be addressed to attain substantial cell performance and widespread commercialization. [8,9] Therefore, it is of vital importance to propose alternative and suitable fuel candidates, other than the commonly used liquid alcohols, to energize future fuel cells.

Generally, the operation of fuel cells involves heat/mass/ions/electron transport and electrochemical reactions, all of which are greatly influenced by temperature, particularly in sub-zero environments. [10,11] Therefore, beyond the common high and room operating temperatures, stable and efficient performance of fuel cells at low and sub-zero temperatures are also expected to be attainable, as fuel cells will be undoubtedly exposed to various climatic conditions in practical applications. [12,13] However, operating the conventional fuel cells under sub-zero temperatures has been reported to be confronted with some critical challenges. For instance, the sluggish oxidation reaction kinetics of liquid alcohol significantly limit their operating temperature windows as well as their application scenarios. [14,15] In addition, the ice formation at sub-zero environment, may not only plug the porous catalyst layer to prevent electrochemical reactions by starving the reactants and reducing the electrochemically active area, but can also lead to an internal short circuit, thereby raising safety concerns. [16,17] Performance loss resulting from insufficient ionic conductivity is another challenge for sub-zero temperature operation of fuel cells. In an attempt to overcome these challenges, previous studies on the operations of conventional liquid fuel cells at sub-zero temperatures incorporated a cold-start strategy, in form of either external or internal heating strategy and its associated thermal control system, to rapidly raise the cell temperature at the beginning of the operation. [18,19] However, this additional heating system for rapid startup not only adds more weight and design complexity to the fuel cell structure, but also deteriorates the system efficiencies. [20,21] It is therefore of paramount importance to develop an electrochemical power system that is completely free of any heating system while enabling a rapid startup and stable operation in a sub-zero environment.

Recently, a novel electrically rechargeable liquid fuel (e-fuel) has been proposed [22,23] and demonstrated. [22,24] Rationally different from the conventional liquid fuels, the liquid e-fuel, which functions as the storage medium, has the potential to be made from various electroactive materials including, but not limited, to metal-ions. We therefore introduce a liquid e-fuel made of vanadium ions for the anodic reaction, paired with oxygen at the cathode side, to demonstrate the operation of a liquid e-fuel cell. Unlike the conventional liquid alcohol fuels, the liquid e-fuel offers an excellent reactivity on carbon-based materials and thus completely removes the need of any noble metal electrocatalyst for the liquid e-fuel oxidation, which significantly reduces the fabrication cost of the cell and enhances its power density, energy efficiency, as well as life-time of the system. Following this, a novel liquid fuel cell, utilizing a graphite-felt anode without any catalyst, is fabricated. In addition, the e-fuel is electrically rechargeable through an e-fuel charger and hence allows an operation for more than 100 cycles, which in turn significantly reduces production and recycling costs of the e-fuel. The typical low freezing point of this liquid e-fuel containing vanadium ions which is ~ -30°C [25] is another significant feature and advantage, which enables the fuel cell to potentially achieve a sub-zero temperature operation.

In this work, the operation of a liquid fuel cell, competent to efficiently converting a liquid e-fuel to generate stable electricity at sub-zero cell temperature as low as -20°C, without involving any form of internal or external heating system is demonstrated. Different from the common cold-start strategies prominent in existing conventional fuel cells, whose temperature needs to be rapidly raised at the beginning of their operation, this e-fuel cell system utilizes a cold-start-free operation strategy, such that cell temperature is maintained at sub-zero while demonstrating stable and high performances. Under this operating condition, the e-fuel cell was able to achieve stable and consistent operation at sub-zero temperatures as low as -20°C, demonstrating a high power density (76.8 mW cm^{-2}) and energy efficiency (25.2 % at 30 mA cm^{-2}), thereby presenting it as a very promising fuel cell candidate for wide range operating temperature and applications. To the best of our knowledge, the successful operation of fuel cells under the aforementioned cell structure and operating conditions has never been reported to be achieved by either hydrogen-oxygen fuel cells or any conventional direct liquid fuel cells. This significant advance thus highlights significant direction for the development of sub-zero temperature fuel cell technology, particularly for energizing future FCEVs with an all-climate operation.

5.2 Experiments

5.2.1 Preparation of a membrane electrode assembly

In this work, a membrane electrode assembly (MEA) with an active area of 2.0 cm × 2.0 cm, consisting of a commercial proton exchange membrane sandwiched between a thermally treated graphite felt and a carbon paper with Pt/C coated was prepared. [24] The commercial membrane Nafion 117, with a geometric size of 3.0 cm × 3.0 cm, was pre-treated using the standard procedure previously reported. [24] It was boiled in 3.0 wt. % hydrogen peroxide solution, deionized (DI) water, 1.0 M sulfuric acid solution and DI water, successively, with each boiling process lasting for 1 hour. Afterwards, the treated membrane was stored in DI water before further use.

5.2.2 E-fuel cell setup and instrumentation

The structural design of the fuel cell, as reported before, [24] consists a pair of graphite flow field engraved with serpentine flow channel, gold-coated current collector, aluminum plate, and plastic endplate was fabricated to investigate the e-fuel cell performance. To avoid any leakage of gas and liquid, several pieces of polytetrafluoroethylene (PTFE) gaskets were used during assembling. On the cathode, pure oxygen at 250 sccm was supplied using an oxygen cylinder through a flow meter (Cole-Parmer, USA).

The experimental setup containing a fuel cell, a low-temperature chamber, a thermometer working with thermocouple (K-type) for monitoring the operating temperature and other accessories, is illustrated in Figure 5.1.

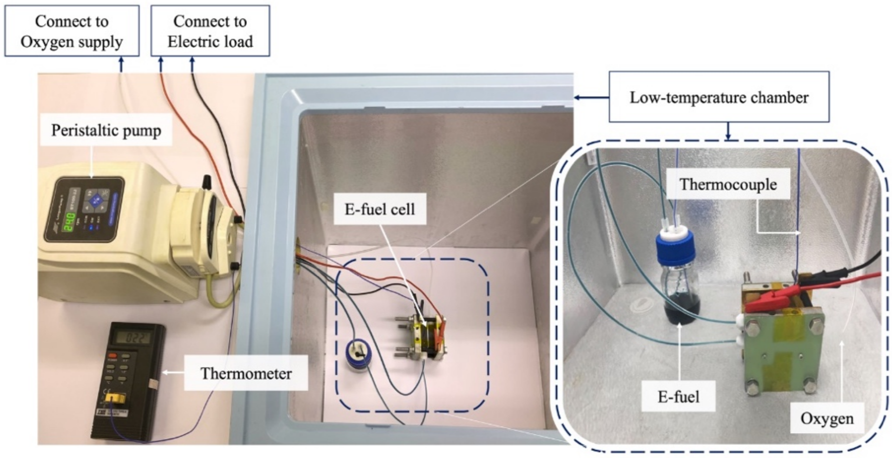

Figure 5.1 Experimental setup of this liquid fuel cell at sub-zero environment.

Before testing, the liquid e-fuel container was first placed in the low-temperature chamber for pre-cooling after purged with N_2. In the meanwhile, the fuel cell was pre-cooled by a 3.0-M sulfuric acid aqueous solution, which was left to circulate until the fuel cell reached the target temperature. During the test, the cell temperature was well-controlled and maintained throughout the whole experiment by cooling the environment with no obvious temperature rise. The polarization and constant-current discharging curves were recorded by the fuel cell testing system (Arbin BT2000, Arbin instrument Inc.).

The electrochemical impedance spectroscopy (EIS) for the fuel cell was conducted (between 0.01 and 10^5 Hz) via an electrochemical workstation (CHI-605C, CH Instruments, China) in order to investigate the contribution of different resistances, while the ionic conductivity of membrane was measured through a home-made cell (between 10^2 and 10^5 Hz) via electrochemical workstation (Autolab PGSTAT 302N, Netherlands). Before the measurement, the membrane was immersed into 3.0 M H_2SO_4 for 24 hours. Afterwards, its ionic conductivity (σ_m) was calculated using:

$$\sigma_\mathrm{m}\ (\mathrm{S\ cm^{-1}}) = \frac{\delta_m}{R_m a_{v,m}} \qquad (2)$$

where δ_m and $a_{v,m}$ represent the thickness and the effective area of the membrane sample, respectively. $\mathrm{R_m}$ represents the ohmic resistance of the membrane, obtained through the real-axis intercepts of the Nyquist plots, which results from the contact resistance and ion-conducting resistance in the membrane. In order to examine the effect of vanadium ions on the membrane conductivity, its conductivity has also been measured after immersing the membrane into the e-fuel of 1.0 M V^{2+} for 24 hours. The cyclic voltammetry tests for the thermally treated graphite felt, and the EIS tests for the liquid e-fuel (between 1 and 10^5 Hz) were conducted in an electrochemical cell using the electrochemical workstation (CHI-660e, CH Instruments, China). The ionic conductivity (σ_e) of the liquid e-fuel was then determined according to:

$$\sigma_\mathrm{e}\ (\mathrm{S\ cm^{-1}}) = \frac{\sigma_\mathrm{KCl} \times \mathrm{R_{KCl}}}{\mathrm{R_e}} = \mathrm{G} \times \frac{1}{\mathrm{R_e}} \qquad (3)$$

where σ_KCl represents the ionic conductivity of KCl standard solution. $\mathrm{R_{KCl}}$ and $\mathrm{R_e}$ represent the overall resistance (including contact resistance and ion-conducting resistance) of the KCl standard solution and the liquid e-fuel, respectively. [26] G represents the cell constant, which was first calibrated using 1.0 D KCl standard solution at 25˚C. [26,27] The viscosity of the liquid e-fuel was measured using the Ubbelohde viscometer. [28]

5.3 Results and discussion

Conventional liquid fuel cells have been mostly operated and studied at room and high temperatures. [29,30] However, as a power generation system, the operating temperature of liquid fuel cells would apparently fluctuate with different places, seasons, and climate areas. To extend the operational temperature range of these systems, it is expedient to also investigate their operations and performances at sub-zero temperatures. Operating fuel cells at sub-zero temperatures, however, raises a few concerns that could limit the overall system performance. To begin with, properties of the liquid fuel including concentration, conductivity, viscosity, and diffusivity could be affected at such a low temperature. Without doubt, these would also affect the mass transport of reactive species to the electrochemical reaction sites and transport properties such as membrane conductivity. Previous studies on the operations of common liquid fuel cells at such a low temperature therefore incorporated pre-heating systems which are on the other hand detrimental to the system efficiencies. Here, with the introduction of liquid e-fuel cells, the need for pre-heating system is eliminated. The use of a catalyst-free graphite-felt as the anode, in lieu of the commonly used noble metal electrocatalyst, for the oxidation of liquid e-fuel in this low temperature fuel cell not only demonstrates an improved reaction kinetics but also improves the system life cycle and reduces the system cost. In addition, as the liquid e-fuel possesses rapid reaction kinetics, the fuel cell is equipped with instantaneous cold-start ability, which in turn facilitates rapid start of the cell at the set temperature whenever and wherever needed. Considering the influences of the low operating temperature on the liquid fuel cell, we therefore examine the: i) effects of operating temperatures on the properties of the liquid e-fuel, membrane, and electrode; and ii) operations and performances of a liquid e-fuel cell at a sub-zero temperature as low as -20˚C, without involving any form of internal or external heating system. The results from the various investigations are presented and discussed in the following sections.

5.3.1 Characterizations of the e-fuel, electrode, and membrane

5.3.1.1 E-fuel performance

The liquid e-fuel can be typically made of different electroactive species such as inorganic materials, organic materials, and suspension of particles. [22] The chemical composition of the liquid e-fuel determines its intrinsic properties including ionic conductivity and viscosity, and further influences the overall fuel cell performance. [25] Another important parameter, operating temperature, also shows a great impact on the properties of liquid e-fuels. Here, the liquid e-fuel containing vanadium ions with its least applicable temperature of ~-30˚C enables the cell to be operated in sub-zero environments. Hence, as shown in Figure 5.2, the viscosity and ionic conductivity of the liquid e-fuel were measured at -20˚C to 20˚C.

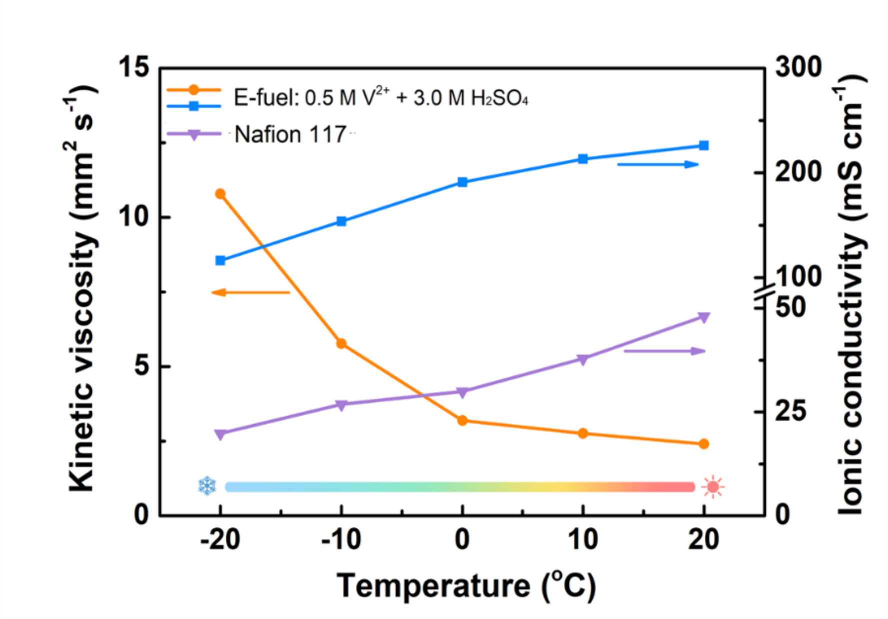

Figure 5.2 Kinetic viscosity and ionic conductivity of this liquid e-fuel, and ionic conductivity of the membrane (Nafion 117) at an operating temperature range from -20˚C to 20˚C.

It can be seen that the viscosity of the liquid e-fuel elevates as the operating temperature declines, which is due to the decreased kinetic energy of water molecules and ions in the liquid e-fuel at low operating temperatures. Such a trend therefore limits the mobility of ions and results in large transport resistance and further lowers ionic conductivity of the e-fuel, thereby demonstrating the significant influence of low operating temperature on the e-fuel properties. [31,32]

5.3.1.2 Membrane performance

As discussed, the fuel cell operation at low temperatures not only limits the transport properties of liquid e-fuels but also influences the transport properties of the ion-exchange membrane. As illustrated in Figure 5.2, with the operating temperature drops to -20˚C, the membrane conductivity also declines from 48.09 to 19.81 mS cm^{-1}. Such variation is considered to be associated with the hindered proton transport through the membrane, which follows two major mechanisms - diffusion and migration. As the operating temperature declines, the increasing liquid e-fuel viscosity hinders the relative motion between water molecules and protons, leading to a lower ion mobility through the membrane and further restrict the diffusion and migration process of protons, which thereby reduces the membrane conductivity. Other than the operating temperature, a lower membrane conductivity of 30.52 mS cm^{-1} is also found at 20˚C after immersing the membrane into the e-fuel made of 1.0 M V^{2+} ions for 24 hours to absorb the metal ions. Such a phenomenon is mainly due to the following reasons: i) the relatively poor mobility of vanadium ions through the membrane in contrast to the protons; and ii) the penetration of vanadium ions into the membrane matrix blocks the ionic conduction pathways inside the membrane and thereby results in the reduced ionic conductivity. [33] It is worth to mention that, similar to protons, the vanadium ions, which can also transport through the membrane and lead to the crossover phenomenon, was reported to show a reduced permeability through the membrane with the declining operating temperature. [34] It is due to the fact that, the diffusion coefficient of vanadium ions and protons reduces as the operating temperature declines, which thereby greatly restricts the transport of these species across the membrane. Still, to lessen vanadium ions crossover and its corresponding negative impacts on the cell performance, [35,36] we therefore utilized a thick membrane (Nafion 117) in our study.

5.3.1.3 Electrode performance

The cyclic voltammetry (CV) is a common method to quantitatively analyze the reaction kinetics of an electrochemical system. [37] Here, to demonstrate the effects of operating temperature on the anode electrochemical performance, the CV curves were obtained at various temperatures, as shown in Figure 5.3. It is shown that, as the temperature declines, the distinct peaks at -0.25 V and 0.4 V are weakened, indicating an inhibited electrochemical reactivity of the electrode. Such a reactivity deterioration mainly comes from the decreased oxidation/reduction reaction rate and increased e-fuel viscosity. It is believed that the rise of the e-fuel viscosity, which results from a reduced kinetic energy of ions, is associated with the declined ions mobility in the liquid e-fuel and therefore hinders the transport of electroactive species moving towards or out from the reactive sites. Such a phenomenon thereby greatly deteriorates the reaction kinetics of the liquid e-fuel oxidation reaction and restricts the electrochemical performance of the electrode. It should also be mentioned that, the superior electrochemical reactivity of the anode is attained after thermal treatment, where the formed oxygen functional groups on the graphite felt would not only aid the vanadium-ion oxidation reaction, but also enhance its hydrophilicity and hence enlarges the effective surface area of the electrode. [38,39]

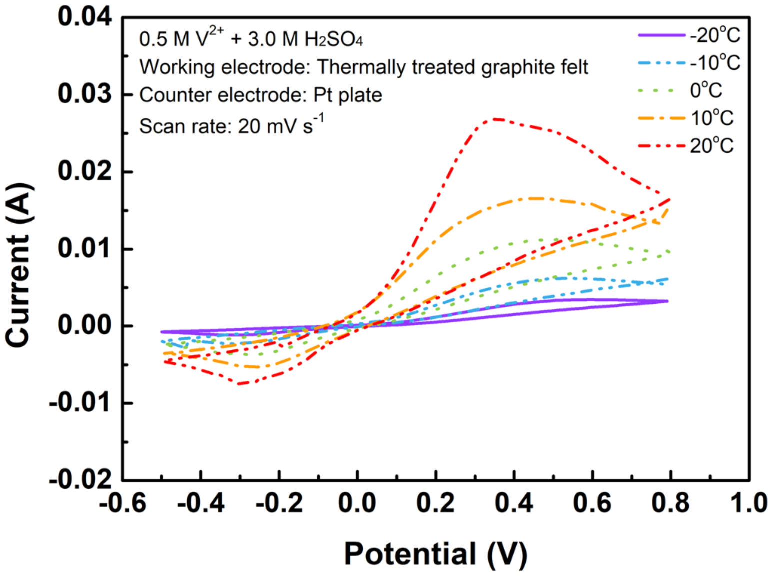

Figure 5.3 Cyclic voltammetry curves of the catalyst-free graphite-felt anode at an operating temperature range from -20˚C to 20˚C.

5.3.2 General performance

As shown in Figures 5.4 (a-b), it is experimentally found that this liquid e-fuel cell can be at -20˚C while achieve a superior performance including a high open-circuit voltage (1.26 V), maximum current density (390 mA cm^{-2}) and peak power density (76.8 mW cm^{-2}). Furthermore, it is able to demonstrate an energy efficiency of 25.2 % at 30 mA cm^{-2}.

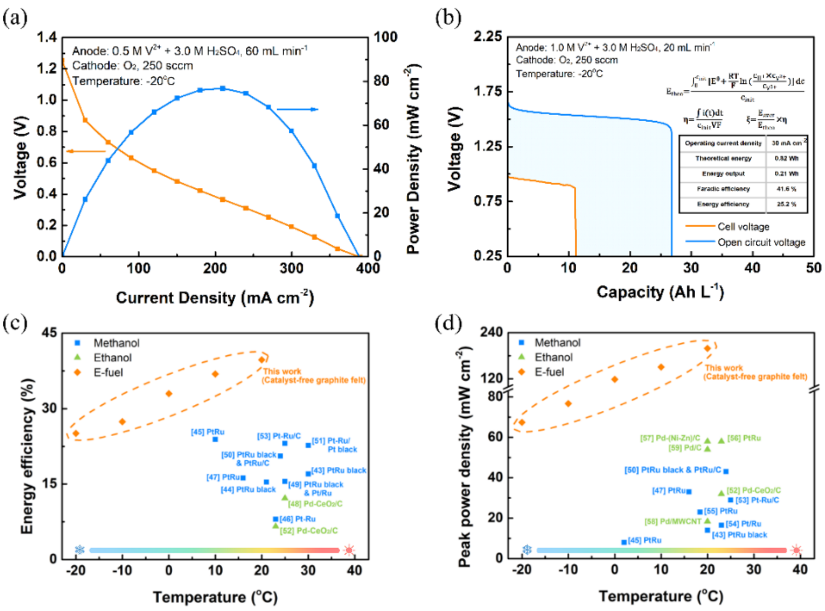

Figure 5.4 (a-b) General performance of this liquid fuel cell at -20˚C; (c) energy efficiency and (d) peak power density comparisons with the data in the open literature.

Compared to conventional liquid fuel cells, the present liquid e-fuel cell possesses the following two advantages: i) it is not only free from any noble metal catalysts for the liquid e-fuel oxidation, but also still able to generate impressive power density and energy efficiency; and ii) it eliminates the needs for extra internal or external pre-heating system while being able to be operated under sub-zero environment. These features greatly expand the operating temperature window and application scenarios of this system. As presented in Figures 5.4 (c-d), all of the results achieved by this cell are way higher than the sub-zero and even room temperature performances of conventional liquid fuel cells as summarized in Tables 5-1 and 5-2. [43-59] Such a notable performance improvement not only highlights significant directions towards the development of sub-zero temperature fuel cells, but also offers great potentials for applications in the future fuel cell electric vehicles.

5.3.3 Effect of the operating temperature

As mentioned earlier, the operating temperature as an important parameter, not only influences the viscosity of the liquid e-fuel and electrode reactivity, but also closely related to the membrane conductivity, which thereby has great impacts on the overall system performance. To investigate the influence of low operating temperatures on the liquid e-fuel cell in detail, experiments were conducted at 20 to -20˚C. As shown in Figure 5.5 (a), significant voltage drops are obtained at the beginning of the polarization curves as a result of activation loss, which is considered to be resulted from the relatively slow reaction kinetics at cathode, [40] in comparison to the fast vanadium-ion oxidation reaction at the anode side. [22] Meanwhile, as mentioned above, due to the crossover phenomenon of vanadium ions, the permeated vanadium ions at the cathode side will result in both vanadium-ion oxidation and oxygen reduction reactions concurrently and thereby leads to a mixed potential. [41] Moreover, it can also be seen that, from 20 to -20˚C, the maximum current density decreases from 660 to 270 mA cm^{-2}, while the peak power density of the e-fuel cell declines from 199 to 67 mW cm^{-2}, demonstrating a declining rate of -9.75 mA cm^{-2} $˚C^{-1}$ and -3.3 mW cm^{-2} $˚C^{-1}$, respectively. Such a declined performance is mainly due to the rise of the membrane and liquid e-fuel resistances, as revealed by the EIS results in Figure 5.5 (b) and Table 5-3. However, the peak power density obtained at

-20˚C is still comparable to those of the common liquid fuel cells at ~ 20˚C (or above) as summarized in Table 5-2, which hence demonstrates the capability of this fuel cell to operate under sub-zero environment in the future. [42]

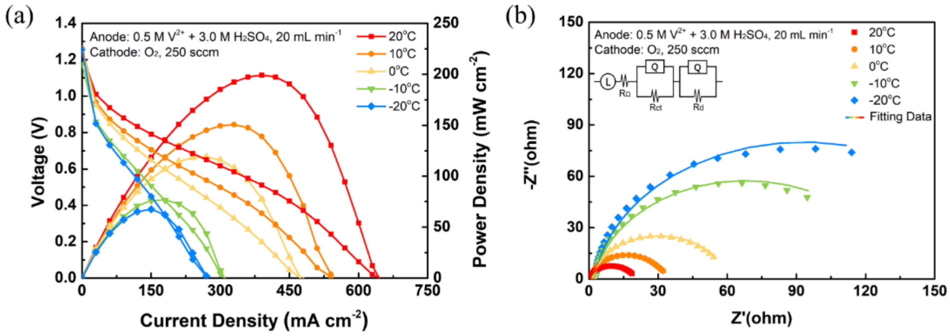

Figure 5.5 (a) Polarization curves, power density curves, and (b) resistances of this liquid fuel cell at an operating temperature range from -20˚C to 20˚C

5.3.4 Effect of the e-fuel flow rate

The mass transport of liquid e-fuel inside the fuel cell is closely related to its flow rate, which hence plays important roles to determine the overall fuel cell performance. Hence, to examine the influences of the flow rate, experiments were conducted at the flow rate between 10 to 60 mL min^{-1} under 0˚C and -20˚C. During the cell operation at 0˚C, with the increase in flow rate as shown in Figure 5.6 (a), the maximum current density increases from 420 mA cm^{-2} to 540 mA cm^{-2} while the peak power density boosts from 97.7 to 147.9 mW cm^{-2}, which hence achieves a 51.4 % higher peak power density. Such an upgraded performance is as a result of the fact that the increase in flow rate facilitates and improves the mass transport of reactants, which thereby results in the reduced resistances, as revealed by EIS results in Figure 5.6 (b) and Table 5-4.

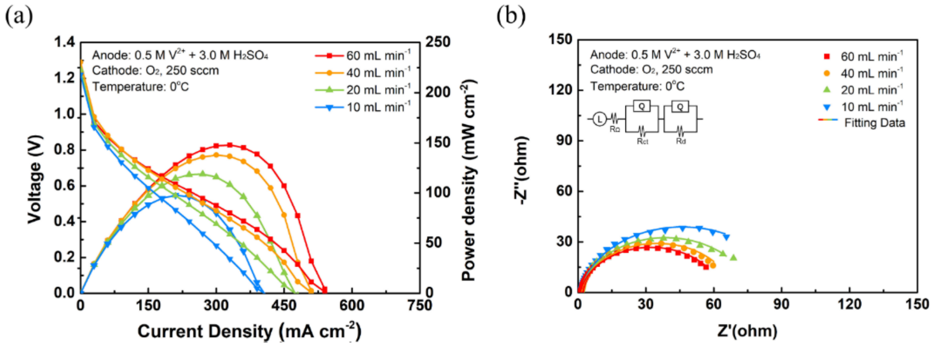

Figure 5.6 (a) Polarization curves, power density curves, and (b) resistances of this liquid fuel cell with flow rates from 10 mL min^{-1} to 60 mL min^{-1} at 0˚C

Furthermore, the fuel cell performance obtained at 60 mL min^{-1} under 0˚C (Figure 5.6 (a)) is even comparable to its performance at 20 mL min^{-1} under 10˚C (Figure 5.5 (a)), suggesting that the increment of the flow rate can ameliorate the limited mass transport observed at low operating temperatures, proving it to be an important factor towards the enhancement of the overall cell performance. Similar trend is also observed when it was operated at -20˚C, as shown in Figure 5.7 (a), with a maximum current density of 390 mA cm^{-2} and a peak power density of 76.8 mW cm^{-2} at 60 mL min^{-1}. In the meanwhile, as presented in Figure 5.7 (b) and Table 5-4, the resistances also decrease as the flow rate increases at -20˚C. It is worth noting that, attributed to the inhibited ion mobility inside the membrane and liquid e-fuel at lower operating temperatures, all of the resistances at -20˚C are much higher than their corresponding values at 0˚C.

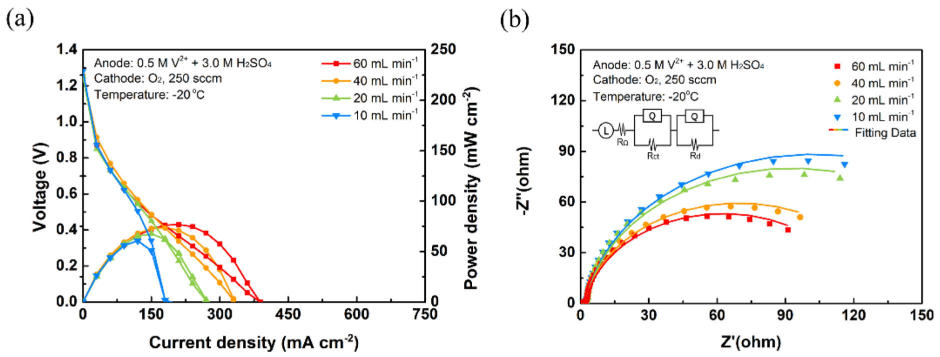

Figure 5.7 (a) Polarization curves, power density curves, and (b) resistances of this liquid fuel cell with flow rates from 10 mL min^{-1} to 60 mL min^{-1} at -20˚C

5.3.5 Constant-current discharging behavior

An efficient approach to determine the operating behavior of the fuel cell during its real application is to perform the constant-current discharging test. It not only accurately reveals the real performance of the system, but also measures its efficiencies and further evaluates its capability for practical applications. As presented in Figures 5.8 (a-b), the constant-current discharging tests were performed at 20 to -20˚C with a liquid e-fuel of 0.5 M and 1.0 M V^{2+}. When the cell is fed with the liquid e-fuel of 1.0 M V^{2+}, it is found that the operating temperature which drops from 20 to -20˚C leads to an obvious reduction in energy output, where the discharging capacity drops from 17.45 to 11.15 Ah L^{-1}. In the meanwhile, the discharge voltage plateau also shows a trend of decreasing as the operating temperature drops, indicating a degraded fuel cell performance.

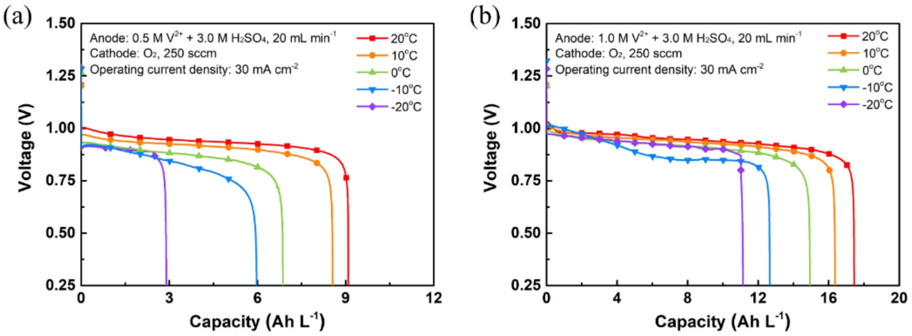

Figure 5.8 Constant-current discharging curves of this fuel cell at an operating temperature range from -20˚C to 20˚C with the e-fuel of (a) 0.5 M and (b) 1.0 M V^{2+} ions.

Such a phenomenon is primarily due to the following reasons: i) based on the Nernst equation as shown in Figure 5.9, the theoretical voltage of the cell decreases with the decline of operating temperature; ii) the low operating temperature reduces the ionic conductivity of the membrane and liquid e-fuel, hence leading to the rise in internal resistance of the system and further limiting the voltage plateau; and iii) the hindered mass transport of electroactive species declines the reaction rate of the liquid e-fuel at lower operating temperatures, which therefore reduces the energy output. The energy efficiency is one significant indicator in evaluating the capability of the fuel cell to efficiently convert chemical energy to electricity, which is calculated based on the ratio of actual generated energy to theoretical energy stored in the fuel cell. It can be influenced by the crossover phenomenon and the internal resistances. In this work, the energy efficiencies of the fuel cell under different operating temperatures were calculated to reflect the fuel cell performance. (Figure 5.10)

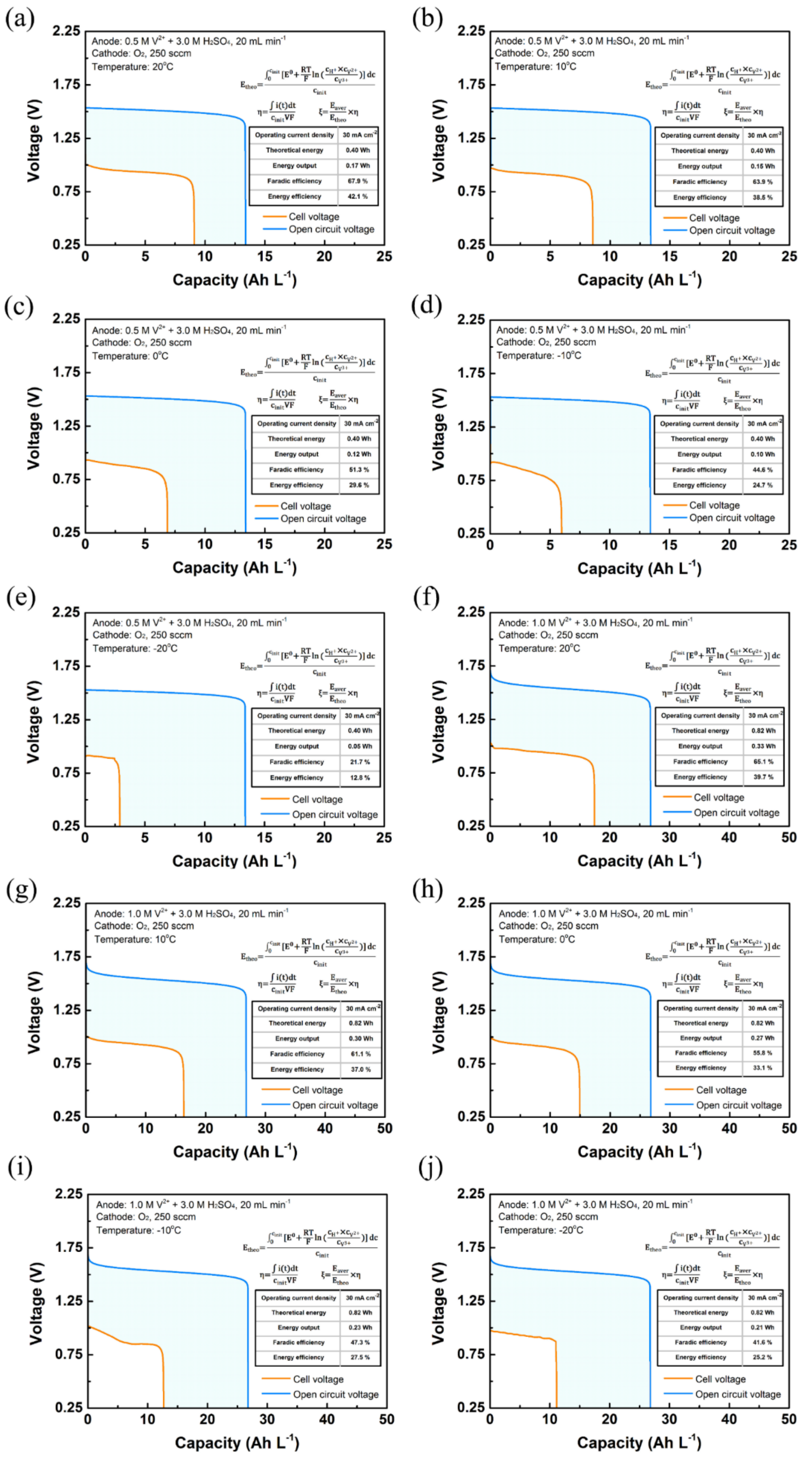

(a)

Operating current density	30 mA cm^{-2}
Theoretical energy	0.40 Wh
Energy output	0.17 Wh
Faradic efficiency	67.9 %
Energy efficiency	42.1 %

(b)

Operating current density	30 mA cm^{-2}
Theoretical energy	0.40 Wh
Energy output	0.15 Wh
Faradic efficiency	63.9 %
Energy efficiency	38.5 %

(c)

Operating current density	30 mA cm^{-2}
Theoretical energy	0.40 Wh
Energy output	0.12 Wh
Faradic efficiency	51.3 %
Energy efficiency	29.6 %

(d)

Operating current density	30 mA cm^{-2}
Theoretical energy	0.40 Wh
Energy output	0.10 Wh
Faradic efficiency	44.6 %
Energy efficiency	24.7 %

(e)

Operating current density	30 mA cm^{-2}
Theoretical energy	0.40 Wh
Energy output	0.05 Wh
Faradic efficiency	21.7 %
Energy efficiency	12.8 %

(f)

Operating current density	30 mA cm^{-2}
Theoretical energy	0.82 Wh
Energy output	0.33 Wh
Faradic efficiency	65.1 %
Energy efficiency	39.7 %

(g)

Operating current density	30 mA cm^{-2}
Theoretical energy	0.82 Wh
Energy output	0.30 Wh
Faradic efficiency	61.1 %
Energy efficiency	37.0 %

(h)

Operating current density	30 mA cm^{-2}
Theoretical energy	0.82 Wh
Energy output	0.27 Wh
Faradic efficiency	55.8 %
Energy efficiency	33.1 %

(i)

Operating current density	30 mA cm^{-2}
Theoretical energy	0.82 Wh
Energy output	0.23 Wh
Faradic efficiency	47.3 %
Energy efficiency	27.5 %

(j)

Operating current density	30 mA cm^{-2}
Theoretical energy	0.82 Wh
Energy output	0.21 Wh
Faradic efficiency	41.6 %
Energy efficiency	25.2 %

Figure 5.9 Energy loss and efficiency analysis of this fuel cell using the e-fuel containing (a-e) 0.5 M and (f-j) 1.0 M V^{2+} ions at -20 to 20°C.

As shown in Figure. 5.10 (b), feeding with the liquid e-fuel containing 1.0 M V^{2+}, the energy efficiency of the cell decreases from 39.7 % to 25.2 % as the operating temperature decreases to -20˚C, due to the increase in activation loss and restricted mass transport of electroactive species. The energy losses at each operating temperature were also analyzed, as shown in Figure 5.9 (with 0.5 M and 1.0 M V^{2+}).

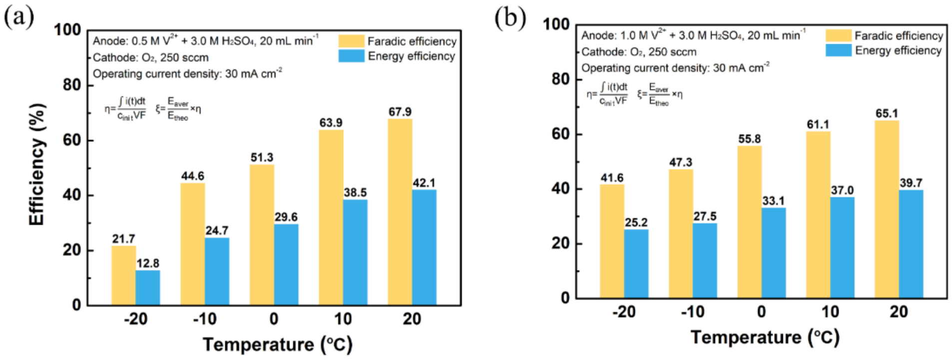

Figure 5.10 Faradic and Energy efficiencies of this fuel cell at an operating temperature range from -20˚C to 20˚C with the e-fuel of (a) 0.5 M and (b) 1.0 M V^{2+} ions.

Despite the decrease in the cell performance at lower operating temperatures, this present fuel cell, attributing to the low freezing point of the liquid e-fuel and its high reactivity on carbon-based materials, is capable of achieving a much higher energy efficiency even at -20˚C without any heating system in comparison to the conventional liquid fuel cells operated even at room temperature (~20˚C) or above, as summarized in Figure 5.4 (c) and Table 5-1. Hence, the present fuel cell with its capability of achieving an energy efficiency of 25.2 % at -20˚C, opens a window for its further application in the future fuel cell electric vehicles in virtually all-climate areas.

5.3.6 Demonstration of a lab-scale e-fuel cell operation in a sub-zero environment

As mentioned, the liquid e-fuel cell with its compelling features and advantages positions the cell to satisfactorily operate in a sub-zero environment. Hence, to practically demonstrate the ability of this cell for power generation, the cell along with a set of LEDs were placed inside a freezing low-temperature chamber (Figure 5.11 (a)). The LEDs arranged in form of PolyU (The Hong Kong Polytechnic University) emit a luminous warm yellow light on top of the ice in this freezing environment, proving that the e-fuel cell not only works at -20˚C, but can also generate stable electricity to power the lights and to brighten the freezing winter during its real application. Hence, this fuel cell, with its e-fuel rechargeability, all-climate operation capability, fast-response, cost-effectiveness, and durability (Figure 5.11 (b)), shows great potentials for diverse applications such as powering electric vehicles, airplanes, cities, industries and emergency power for grid. However, it is undeniable that this system is still being confronted by some limitations such as a relatively low energy density in comparison to conventional liquid alcohol fuels and compressed hydrogen and the continuous need of oxygen during the cell operation, which thereby hampers its application scenarios such as in space craft or in submarine. It is therefore considered to be of paramount importance to try to increase the solubility of vanadium-ions as well as screen and develop other materials for the e-fuel fabrication so as to gain a higher energy density in the future. These findings therefore suggest further directions for more future studies and investigations on this novel liquid e-fuel cell technology.

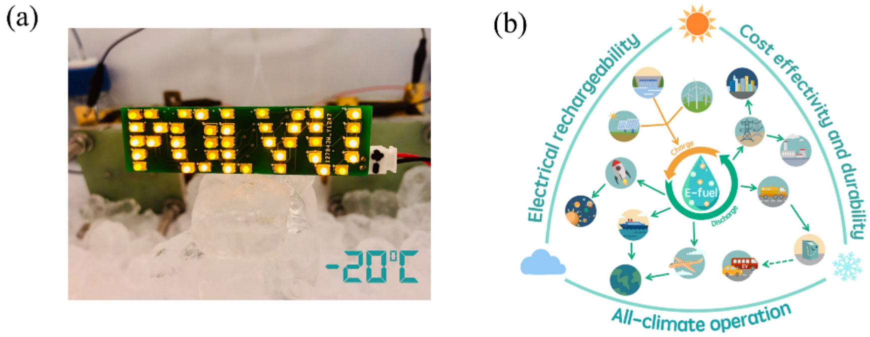

Figure 5.11 (a) Demonstration of a lab-scale fuel cell operation in a sub-zero environment and (b) potential applications of this e-fuel cell technology.

5.4 Summary

In this work, the operation of a liquid e-fuel cell, completely free of any internal or external heating systems, capable of stably and continuously generating electricity at sub-zero cell temperatures as low as -20˚C is demonstrated. The liquid e-fuel cell employs a graphite-felt free from any catalyst as anode and is experimentally found to exhibit a superior cell performance including a peak power density of 76.8 mW cm^{-2} and an energy efficiency of 25.2 % even at -20˚C, outperforming all of those conventional liquid alcohol fuel cells that were operated and tested at sub-zero and even at higher temperatures (20˚C or above). It is believed that this present cell possesses the prospects to achieve higher and better performance after future modifications including, but not limited to, the optimization of the cell structure and component materials, such as more suitable e-fuels of higher reactivity, energy density, and lower freezing point. It therefore opens a path for the development of liquid e-fuel cells towards achieving a better fuel cell performance with even wider operational temperature range.

5.5 References

1. C. Duan, R. Kee, H. Zhu, N. Sullivan, L. Zhu, L. Bian, D. Jennings and R. O Hayre, Highly efficient reversible protonic ceramic electrochemical cells for power generation and fuel production, Nat. Energy, 2019, 4, 230-240.

2. Y. J. Wang, J. Qiao, R. Baker and J. Zhang, Alkaline polymer electrolyte membranes for fuel cell applications, Chem. Soc. Rev., 2013, 42, 5768-5787.

3. E. Fabbri, D. Pergolesi and E. Traversa, Materials challenges toward proton-conducting oxide fuel cells: a critical review, Chem. Soc. Rev., 2010, 39, 4355-4369.

4. N. Ramaswamy and S. Mukerjee, Alkaline Anion-Exchange Membrane Fuel Cells: Challenges in Electrocatalysis and Interfacial Charge Transfer, Chem. Rev., 2019, 119, 11945-11979.

5. C. J. Zhong, J. Luo, P. N. Njoki, D. Mott, B. Wanjala, R. Loukrakpam, S. Lim, L. Wang, B. Fang and Z. Xu, Fuel cell technology: nano-engineered multimetallic catalysts, Energy Environ. Sci., 2008, 1, 454-466.

6. J. Yang and S. Hirano, Improving the hydrogen reaction kinetics of complex hydrides, Adv. Mater., 2009, 21, 3023-3028.

7. L. Schlapbach, Hydrogen-fuelled vehicles, Nature, 2009, 460, 809-811.

8. B. Ong, S. Kamarudin and S. Basri, Direct liquid fuel cells: A review, Int. J. Hydrogen Energy, 2017, 42, 10142-10157.

9. J. N. Tiwari, R. N. Tiwari, G. Singh and K. S. Kim, Recent progress in

the development of anode and cathode catalysts for direct methanol fuel cells, Nano Energy, 2013, 2, 553-578.

10. F. Mo, G. Liang, Q. Meng, Z. Liu, H. Li, J. Fan and C. Zhi, A flexible rechargeable aqueous zinc manganese-dioxide battery working at− 20° C, Energy Environ. Sci., 2019, 12, 706-715.

11. J. A. Malen and V. Viswanathan, Regulating hot and cold, Nat. Energy, 2018, 3, 826-827.

12. M. Hao, J. Li, S. Park, S. Moura and C. Dames, Efficient thermal management of Li-ion batteries with a passive interfacial thermal regulator based on a shape memory alloy, Nat. Energy, 2018, 3, 899-906.

13. M.-T. F. Rodrigues, G. Babu, H. Gullapalli, K. Kalaga, F. N. Sayed, K. Kato, J. Joyner and P. M. Ajayan, A materials perspective on Li-ion batteries at extreme temperatures, Nat. Energy, 2017, 2, 1-14.

14. C. Bianchini and P. K. Shen, Palladium-based electrocatalysts for alcohol oxidation in half cells and in direct alcohol fuel cells, Chem. Rev., 2009, 109, 4183-4206.

15. H. S. Casalongue, S. Kaya, V. Viswanathan, D. J. Miller, D. Friebel, H. A. Hansen, J. K. Nørskov, A. Nilsson and H. Ogasawara, Direct observation of the oxygenated species during oxygen reduction on a platinum fuel cell cathode, Nat. Commun., 2013, 4, 1-6.

16. R. Borup, J. Meyers, B. Pivovar, Y. S. Kim, R. Mukundan, N. Garland, D. Myers, M. Wilson, F. Garzon and D. Wood, Scientific aspects of polymer

electrolyte fuel cell durability and degradation, Chem. Rev., 2007, 107, 3904-3951.

17. O. Z. Sharaf and M. F. Orhan, An overview of fuel cell technology: Fundamentals and applications, Renew. Sust. Energ. Rev., 2014, 32, 810-853.

18. X. Hu, Y. Zheng, D. A. Howey, H. Perez, A. Foley and M. Pecht, Battery warm-up methodologies at subzero temperatures for automotive applications: Recent advances and perspectives, Progr. Energy Combust. Sci., 2020, 77, 100806.

19. P. Atanassov, Fuel cells: a call for total design, Joule, 2018, 2, 1210-1211.

20. Y. Luo and K. Jiao, Cold start of proton exchange membrane fuel cell, Progr. Energy Combust. Sci., 2018, 64, 29-61.

21. J. Deng, C. Bae, A. Denlinger and T. Miller, Electric Vehicles Batteries: Requirements and Challenges, Joule, 2020.

22. H. Jiang, L. Wei, X. Fan, J. Xu, W. Shyy and T. Zhao, A novel energy storage system incorporating electrically rechargeable liquid fuels as the storage medium, Sci. Bull., 2019, 64, 270-280.

23. K. Amine, E-fuel system: a conceptual breakthrough for energy storage, Sci. Bull., 2019, 64, 227-228.

24. X. Shi, X. Huo, Y. Ma, Z. Pan and L. An, Energizing fuel cells with an electrically rechargeable liquid fuel, Cell Rep. Phys. Sci., 2020, 1, 100102.

25. S. Xiao, L. Yu, L. Wu, L. Liu, X. Qiu and J. Xi, Broad temperature adaptability of vanadium redox flow battery—Part 1: Electrolyte research, Electrochim. Acta, 2016, 187, 525-534.

26. F. Azeez and P. S. Fedkiw, Conductivity of libob-based electrolyte for lithium-ion batteries, J. Power Sources, 2010, 195, 7627-7633.

27. D. Feng and L. Holland, A dc Method for the Absolute Determination of Conductivities of the Primary Standard KCl Solutions from 0^ C to 50" C, J. Res. Natl. Inst. Stand. Technol., 1994, 99.

28. S. Zhang, B. Zhang, G. Zhao and X. Jian, Anion exchange membranes from brominated poly (aryl ether ketone) containing 3, 5-dimethyl phthalazinone moieties for vanadium redox flow batteries, J. Mater. Chem. A, 2014, 2, 3083-3091.

29. Y. J. Wang, D. P. Wilkinson and J. Zhang, Noncarbon support materials for polymer electrolyte membrane fuel cell electrocatalysts, Chem. Rev., 2011, 111, 7625-7651.

30. R. Thimmappa, S. Aralekallu, M. C. Devendrachari, A. R. Kottaichamy, Z. M. Bhat, S. P. Shafi, K. S. Lokesh and M. O. Thotiyl, A single chamber direct methanol fuel cell, Adv. Mater. Interfaces, 2017, 4, 1700321.

31. J. Datta, A. Dutta and S. Mukherjee, The beneficial role of the cometals Pd and Au in the carbon-supported PtPdAu catalyst toward promoting ethanol oxidation kinetics in alkaline fuel cells: temperature effect and reaction mechanism, J. Phys. Chem. C, 2011, 115, 15324-15334.

32. X. Li, J. Xiong, A. Tang, Y. Qin, J. Liu and C. Yan, Investigation of the use of electrolyte viscosity for online state-of-charge monitoring design in vanadium redox flow battery, Appl. Energy, 2018, 211, 1050-1059.

33. S. Yun, J. Parrondo and V. Ramani, Derivatized cardo-polyetherketone anion exchange membranes for all-vanadium redox flow batteries, J. Mater. Chem. A, 2014, 2, 6605-6615.

34. J. Winsberg, T. Hagemann, T. Janoschka, M. D. Hager and U. S. Schubert, Redox-flow batteries: from metals to organic redox-active materials, Angew. Chem. Int. Ed., 2017, 56, 686-711.

35. M. Zago, A. Bisello, A. Baricci, C. Rabissi, E. Brightman, G. Hinds and A. Casalegno, On the actual cathode mixed potential in direct methanol fuel cells, J. Power Sources, 2016, 325, 714-722.

36. J. Xi, S. Xiao, L. Yu, L. Wu, L. Liu and X. Qiu, Broad temperature adaptability of vanadium redox flow battery—Part 2: Cell research, Electrochim. Acta, 2016, 191, 695-704.

37. H. Wang, X. Yuan and H. Li, PEM Fuel Cell Diagnostic Tools, CRC Press, Taylor and Francis Group, 2012.

38. H. Zhang, X. Li and J. Zhang, Redox Flow Batteries: Fundamentals and Applications, CRC Press, 2017.

39. Y. Kim, Y. Y. Choi, N. Yun, M. Yang, Y. Jeon, K. J. Kim and J.-I. Choi, Activity gradient carbon felt electrodes for vanadium redox flow batteries, J. Power Sources, 2018, 408, 128-135.

40. N. Zhang, X. Chen, Y. Lu, L. An, X. Li, D. Xia, Z. Zhang and J. Li, Nano-Intermetallic AuCu3 Catalyst for Oxygen Reduction Reaction: Performance and Mechanism, Small, 2014, 10, 2662-2669.

41. A. Kulikovsky, A model for mixed potential in direct methanol fuel cell cathode, Electrochim. Acta, 2012, 62, 185-191.

42. J. Kim and H. Park, Electrokinetic parameters of a vanadium redox flow battery with varying temperature and electrolyte flow rate, Renew. Energ., 2019, 138, 284-291.

43. R. Jiang, C. Rong and D. Chu, Determination of energy efficiency for a direct methanol fuel cell stack by a fuel circulation method, J. Power Sources, 2004, 126, 119-124.

44. J. Liu, T. S. Zhao, R. Chen and C. W. Wong, Effect of methanol concentration on passive DMFC performance, Fuel Cells Bull., 2005, 2005, 12-17.

45. D. Chu and R. Jiang, Effect of operating conditions on energy efficiency for a small passive direct methanol fuel cell, Electrochim. Acta, 2006, 51, 5829-5835.

46. L. Feng, J. Zhang, W. Cai, W. Xing and C. Liu, Single passive direct methanol fuel cell supplied with pure methanol, J. Power Sources, 2011, 196, 2750-2753.

47. C. Xu, A. Faghri and X. Li, Improving the water management and cell performance for the passive vapor-feed DMFC fed with neat methanol, Int.

J. Hydrogen Energy, 2011, 36, 8468-8477.

48. V. Bambagioni, C. Bianchini, Y. Chen, J. Filippi, P. Fornasiero, M. Innocenti, A. Lavacchi, A. Marchionni, W. Oberhauser and F. Vizza, Energy efficiency enhancement of ethanol electrooxidation on Pd–CeO2/C in passive and active polymer electrolyte-membrane fuel cells, ChemSusChem, 2012, 5, 1266-1273.

49. J. Cao, L. Wang, L. Song, J. Xu, H. Wang, Z. Chen, Q. Huang and H. Yang, Novel cathodal diffusion layer with mesoporous carbon for the passive direct methanol fuel cell, Electrochim. Acta, 2014, 118, 163-168.

50. P. Chen, H. Wu, T. Yuan, Z. Zou, H. Zhang, J. Zheng and H. Yang, Electronspun nanofiber network anode for a passive direct methanol fuel cell, J. Power Sources, 2014, 255, 70-75.

51. H. Deng, Y. Zhang, X. Zheng, Y. Li, X. Zhang and X. Liu, A CNT (carbon nanotube) paper as cathode gas diffusion electrode for water management of passive μ-DMFC (micro-direct methanol fuel cell) with highly concentrated methanol, Energy, 2015, 82, 236-241.

52. L. Wang, A. Lavacchi, M. Bevilacqua, M. Bellini, P. Fornasiero, J. Filippi, M. Innocenti, A. Marchionni, H. A. Miller and F. Vizza, Energy efficiency of alkaline direct ethanol fuel cells employing nanostructured palladium electrocatalysts, ChemCatChem, 2015, 7, 2214-2221.

53. F. Zhang, J. Jiang, Y. Zhou, J. Xu, Q. Huang, Z. Zou, J. Fang and H. Yang, A neat methanol fed passive DMFC with a new anode structure, Fuel

Cells, 2017, 17, 315-320.

54. G. Q. Lu, C. Y. Wang, T. J. Yen and X. Zhang, Development and characterization of a silicon-based micro direct methanol fuel cell, Electrochim. Acta, 2004, 49, 821-828.

55. R. Chen and T. S. Zhao, A novel electrode architecture for passive direct methanol fuel cells, Electrochem. Commun., 2007, 9, 718-724.

56. N. Fujiwara, Z. Siroma, S. i. Yamazaki, T. Ioroi, H. Senoh and K. Yasuda, Direct ethanol fuel cells using an anion exchange membrane, J. Power Sources, 2008, 185, 621-626.

57. C. Bianchini, V. Bambagioni, J. Filippi, A. Marchionni, F. Vizza, P. Bert and A. Tampucci, Selective oxidation of ethanol to acetic acid in highly efficient polymer electrolyte membrane-direct ethanol fuel cells, Electrochem. Commun., 2009, 11, 1077-1080.

58. V. Bambagioni, C. Bianchini, A. Marchionni, J. Filippi, F. Vizza, J. Teddy, P. Serp and M. Zhiani, Pd and Pt–Ru anode electrocatalysts supported on multi-walled carbon nanotubes and their use in passive and active direct alcohol fuel cells with an anion-exchange membrane (alcohol= methanol, ethanol, glycerol), J. Power Sources, 2009, 190, 241-251.

59. X. Sun, Y. Li and M. J. Li, Highly dispersed palladium nanoparticles on carbon-decorated porous nickel electrode: an effective strategy to boost direct ethanol fuel cell up to 202 mW cm-2, ACS Sustain. Chem. Eng., 2019.

Table

Table 5-1 Energy efficiency comparison among various liquid fuel cells.

Year	Discharge condition	Temp.	Energy efficiency	Liquid fuel	Catalysts for liquid fuel oxidation	Ref.
2004	8 V	30°C	17 %	Methanol	PtRu black (4 mg cm^{-2})	43
2005	0.35 V	21-23°C	15.4 %	Methanol	PtRu black (4 mg cm^{-2})	44
2006	0.6 V	10°C	23.9 %	Methanol	PtRu (4 mg cm^{-2})	45
2011	11.1 mA cm^{-2}	R.T.	8 %	Methanol	Pt-Ru (8 mg cm^{-2})	46
2011	0.3 V	16~26°C	16.2 %	Methanol	Pt:Ru (5 mg cm^{-2})	47
2012	20 mA cm^{-2}	25°C	12.2 %	Ethanol	Pd–CeO$_2$/C (1 mg cm^{-2})	48
2014	40 mA cm^{-2}	25°C	15.5 %	Methanol	Pt-Ru black and Pt-Ru/C (4 ± 0.2 mg cm^{-2})	49
2014	0.35 V	25±1°C	20.6 %	Methanol	PtRu black and PtRu/C (2 mg cm^{-2})	50
2015	100 mA cm^{-2}	30°C	22.7 %	Methanol	Pt-Ru/Pt black (4 mg cm^{-2})	51
2015	20 mA cm^{-2}	R.T.	6.57 %	Ethanol	Pd-CeO$_2$/C (1 mg cm^{-2})	52
2017	0.35 V	25°C	23.1 %	Methanol	Pt-Ru/C (4 mg cm^{-2})	53
2021	30 mA cm^{-2}	20°C	39.7 %	E-fuel	Catalyst-free graphite felt	This work
		10°C	37.0 %			
		0°C	33.1 %			
		-10°C	27.5 %			
		-20°C	25.2 %			

Table 5-2 Peak power density comparison among various liquid fuel cells.

Year	**Temp.**	**Peak power density (mW cm^{-2})**	**Liquid fuel**	**Catalysts for liquid fuel oxidation**	**Ref.**
2004	20°C	14.00	Methanol	PtRu black (4 mg cm^{-2})	43
2004	23°C	16.50	Methanol	Pt/Ru (4-6 mg cm^{-2})	54
2006	2°C	~16	Methanol	PtRu (4 mg cm^{-2})	45
2007	18.4°C	~23	Methanol	PtRu (4 mg cm^{-2})	55
2008	R.T.	58.00	Ethanol	PtRu black (3 mg cm^{-2})	56
2009	20°C	58.00	Ethanol	Pd–(Ni–Zn)/C (1 mg cm^{-2})	57
2009	20-22°C	18.4	Ethanol	Pd/MWCNT (0.7 mg cm^{-2})	58
2011	16~26°C	33	Methanol	Pt:Ru (5 mg cm^{-2})	47
2014	25±1°C	43.0±0.9	Methanol	PtRu black and PtRu/C (2 mg cm^{-2})	50
2015	R.T.	47	Ethanol	Pd-CeO$_2$/C (1 mg cm^{-2})	52
2017	25°C	29	Methanol	Pt-Ru/C (4 mg cm^{-2})	53
2019	20°C	54	Ethanol	Pd/C (5 mg cm^{-2})	59
2021	20°C	199.2	E-fuel	Catalyst-free graphite felt	This work
	10°C	150.7			
	0°C	118.9			
	-10°C	76.7			
	-20°C	67.4			

Table 5-3 EIS fitting results of this fuel cell at operating temperatures from -20˚C to 20˚C.

Temperature (˚C)	**L (nH)**	**R_Ω (Ohm)**	**R_{ct} (Ohm)**	**Q_{ct} ($Ohm^{-1}\ s^n$)**	**n_{ct}**	**R_d (Ohm)**	**Q_d ($Ohm^{-1}\ s^n$)**	**n_d**
-20	3.958	0.648	181.50	0.056	0.920	1.722	0.013	0.751
-10	3.838	0.626	131.10	0.059	0.916	1.864	0.010	0.796
0	3.872	0.509	58.47	0.061	0.905	1.025	0.011	0.787
10	3.861	0.459	32.42	0.065	0.906	0.413	0.015	0.765
20	1.187	0.350	18.73	0.114	0.880	0.053	0.007	0.917

Table 5-4 EIS fitting results of this fuel cell with anolyte flow rates from 10 to 60 mL min^{-1} at -20˚C and 0˚C.

Temp. (˚C)	**Flow rate (mL min^{-1})**	**L (nH)**	**R_{Ω} (Ohm)**	**R_{ct} (Ohm)**	**Q_{ct} (Ohm^{-1} s^{n})**	**n_{ct}**	**R_{d} (Ohm)**	**Q_{d} (Ohm^{-1} s^{n})**	**n_{d}**
-20	10	3.960	0.654	199.90	0.055	0.921	1.754	0.013	0.755
	20	3.958	0.648	181.50	0.056	0.920	1.722	0.013	0.751
	40	3.852	0.598	134.80	0.059	0.919	1.633	0.010	0.795
	60	3.852	0.608	121.00	0.059	0.918	1.661	0.010	0.799
0	10	3.714	0.512	89.66	0.059	0.912	0.773	0.013	0.776
	20	3.718	0.508	75.17	0.059	0.911	0.703	0.014	0.770
	40	3.819	0.501	67.30	0.061	0.910	0.655	0.011	0.795
	60	3.831	0.494	62.50	0.062	0.904	0.607	0.019	0.729

Chapter 6 Mathematical modeling

6.1 Introduction

In recent decades, due to the growing needs for energy across the globe, the search for sustainable energy sources to replace the traditional fossil fuels has attracted increasing attention. [1-3] To date, diverse kinds of novel power generation systems have been developed, among which the proton exchange membrane fuel cell (PEMFC) employing hydrogen as fuel has received great attention. [4,5] However, hampered by the difficulties of hydrogen production, storage, and transportation, the widespread adoption of PEMFCs is still being restricted. [6,7] As an alternative, liquid fuel cell using alcohol fuels instead of hydrogen is believed to be a promising candidate. [4,8,9] While the liquid fuel cells avoid the difficulties associated with the handling of gaseous fuels, their limited performance become the major barriers in their commercialization process. [10,11]

Recently, an innovative fuel cell using an electrically rechargeable liquid fuel (e-fuel) has attracted research attentions worldwide. [12-14] Using the e-fuel and oxygen, we have developed a liquid fuel cell and investigated its performance under various operating conditions. [15,16] While the demonstrated system has presented its superior performance, it is believed that there remains a large room for further performance improvement in the future. Therefore, it is necessary to develop a mathematical model that can simulate the processes in the system under different conditions as: i) it can help to gain an in-depth insight on the complex physical and chemical processes which occur inside the cell; [17-20] and ii) it can give an effective and economical approach to predict the influences of various structural and operation parameters on the fuel cell performance and further provide directions for future system improvement.

In this work, a two-dimensional transient model has been developed for a liquid fuel cell fed with the e-fuel. To begin with, the experimental data has been compared with the simulation results for validation, which is found to show a good agreement. Thereafter, to illustrate the effects of various structural parameters and operating conditions, the cell performance is simulated by varying the e-fuel compositions, oxygen concentrations, electrode porosity and thickness, as well as exchange current densities. Moreover, to gain an extensive knowledge for the e-fuel cell and analyze the major factors limiting its performance, the concentration distributions of reactive species in the cell are obtained to provide substantial information inside the cell.

6.2 Model formulation

6.2.1 Physical and chemical processes

The computational domain of the cell is presented in Figure 6.1, comprising of the anode/cathode current collectors, a porous anode, an ion exchange membrane (IEM), and a porous cathode diffusion layer (CDL) coated with cathode catalyst layer (CCL). During the cell operation, the e-fuel would transport from the tank to the anode surface for the oxidation reaction as shown below:[12]

Anode: $V^{2+} \rightarrow V^{3+} + e^{-}$ $\qquad E_a^0 = -0.26\ V \qquad (1)$

The released electrons would then follow the external electrical circuit to reach the cathode side. Meanwhile, the oxidant will diffuse through the CDL to the CCL surface to react with the protons and electrons as:[12]

Cathode: $O_2 + 4H^{+} + 4e^{-} \rightarrow 2H_2O$ $\qquad E_c^0 = +1.23\ V \qquad (2)$

The overall reaction can thus be expressed as:[12]

Overall: $4V^{2+} + O_2 + 4H^{+} \rightarrow 4V^{3+} + 2H_2O$ $\qquad E^0 = 1.49\ V \qquad (3)$

Therefore, thermodynamically, the theoretical voltage of this cell is as high as 1.49 V, which exceeds that of the convectional alcohol fuel cells and PEMFCs.[12]

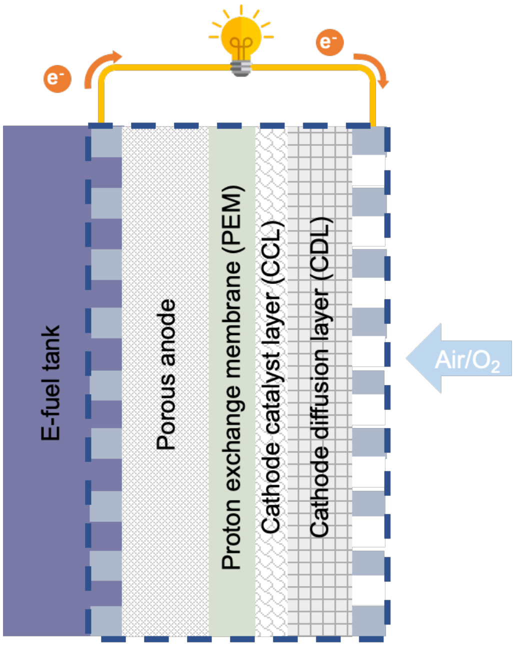

Figure 6.1 Schematic of the domain of passive liquid fuel cell.

6.2.2 Model assumptions

To simplify the multiple physical and chemical processes occurring inside the cell, the computational 2D model considers the following assumptions:

1) Properties of anode, cathode and membrane are regarded to be homogeneous and isotropic.
2) The crossover of liquid/gas flow across the membrane are neglected.
3) Side reactions are neglected.
4) The liquid water generated during the cell operation is ignored.
5) The two-step dissociation of sulfuric acid is fully completed.

6.2.3 Governing equations

6.2.3.1 Anode

6.2.3.1.1 Mass transport

The mass transport of various species at the anode side mainly follows diffusion and migration. Following the Nernst-Plank equation, the molar flux ($\vec{N_i}$) of each specie *i* can be described as:[21]

$$\overrightarrow{N_\iota} = -D_i^{eff}\nabla C_i - z_i \mathrm{u}_i^{\mathrm{eff}} F C_i \nabla \emptyset_{a,l} \tag{4}$$

where C_i and z_i is the concentration and charge number of species *i* (i = V^{2+}, V^{3+}, H^+, $SO_4{}^{2-}$), respectively. F denotes Faradic constant. The effective diffusivity (D_i^{eff}) in the porous anode is given by the Bruggeman relation as: [22]

$$D_i^{eff} = \varepsilon_a{}^{1.5} D_i \tag{5}$$

where ε_a represents the porosity of anode and D_i represents the diffusion coefficient of specie i. The effective mobility (u_i^{eff}) in the porous anode follows the Nernst-Einstein relation as: [23]

$$u_i^{eff} = \frac{D_i^{eff}}{RT} \tag{6}$$

The mass conservation of each specie inside the anode at the transient state can be expressed as:[24]

$$\frac{\partial \varepsilon_a C_i}{\partial t} + \nabla \overrightarrow{N_i} = S_i \tag{7}$$

The source term S_i is the consumption/production rate of the species i resulted from the electrochemical reactions occurred in the porous anode, which is represented as:[17]

$$S_i = \frac{v_{a,i}}{n_a F} i_a \tag{8}$$

where v_a, n_a and i_a denote the stoichiometric coefficient, the number of participating electrons and the anode current density, respectively.

6.2.3.1.2 Charge transport

Inside the porous anode, the liquid fuel is considered as electrically neutral. Therefore, the electroneutrality can be described by (i = V^{2+}, V^{3+}, H^+, SO_4^{2-}): [25]

$$\Sigma z_i C_i = 0 \tag{9}$$

During the cell operation, the charges transfer from the liquid phase to the solid electrode phase and generate current. Therefore, the charge conservation can be described as:[17]

$$i_a = \nabla \cdot \overrightarrow{i_{a,l}} = -\nabla \cdot \overrightarrow{i_{a,s}} \tag{10}$$

where $\overrightarrow{i_{a,l}}$ is the total ionic current due to ions transfer in the solutions (i = V^{2+}, V^{3+}, H^+, SO_4^{2-}), which is given by:[17]

$$\overrightarrow{i_{a,l}} = F \sum z_i \overrightarrow{N_i} \tag{11}$$

while $\overrightarrow{i_{a,s}}$ represents the total electronic current as: [17]

$$\overrightarrow{i_{a,s}} = -\sigma_a^{eff} \nabla \emptyset_{a,s} \tag{12}$$

where $\emptyset_{a,s}$ and σ_a^{eff} are the electric potential and effective electronic conductivity of anode, respectively. The σ_a^{eff} is calculated by the Bruggeman correction as: [25]

$$\sigma_a^{eff} = (1-\varepsilon_a)^{3/2} \sigma_a \tag{13}$$

where σ_a is the electronic conductivity of the anode.

6.2.3.2 Cathode

6.2.3.2.1 Mass transport

At the cathode side, the diluted species approximation was used to describe the species transport. The air is diffused through the porous CDL to the CCL and the oxygen flux ($\vec{N}_{O_2}$) is defined by Fick's law: [26]

$$\overrightarrow{N_{O_2}} = -D_{O_2}^{eff} \nabla C_{O_2} \tag{14}$$

where C_{O_2} is the concentration of oxygen. The effective diffusivity $D_{O_2}^{eff}$ is given by the Bruggeman relation as: [22]

$$D_{O_2}^{eff} = \varepsilon_{ccl/cdl}^{\frac{3}{2}} D_{O_2} \tag{15}$$

where $\varepsilon_{ccl/cdl}$ represents the porosity of the CCL or CDL and D_{O_2} represents the diffusion coefficient of oxygen. The mass conservation at cathode side is given by:

$$\frac{\partial \varepsilon_{ccl/cdl} C_{O_2}}{\partial t} + \nabla \overrightarrow{N_{O_2}} = S_{O_2} \tag{16}$$

where the source term (S_{O_2}) can be represented as:[27]

$$S_{O_2} = \frac{v_{O_2}}{n_c F} i_c \tag{17}$$

where v_{O_2}, n_c and i_c denote the stoichiometric coefficient, the number of participating electrons and the cathode current density, respectively.

It is worth mentioning that when pure oxygen is used, the cathode is assumed to be fully filled with oxygen, where the oxygen concentration in the CCL and CDL are expressed as:[26]

$$C_{O_2} = C_{O_2,pure}^{0} \tag{18}$$

6.2.3.2.2 Charge transport

During the cell operation, the charge conservation in CCL is described by:[17]

$$i_c = \nabla \cdot \overrightarrow{i_{c,l}} = -\nabla \cdot \overrightarrow{i_{c,s}} \tag{19}$$

where $\overrightarrow{i_{c,l}}$ is the total ionic current due to ions transfer, which is given by:[17]

$$\overrightarrow{i_{c,l}} = -\sigma_{ccl,l} \nabla \emptyset_{c,l} \tag{20}$$

where $\sigma_{ccl,l}$ and $\emptyset_{c,l}$ are the ionic conductivity and ionic potential of CCL, respectively. $\overrightarrow{\imath_{c,s}}$ is the total electronic current due to electron transfer in the solid CCL following the Ohm's law:[17]

$$\overrightarrow{\imath_{c,s}} = -\sigma_{ccl,s}\nabla\emptyset_{c,s} \tag{21}$$

where $\sigma_{ccl,s}$ and $\emptyset_{c,s}$ are the electronic conductivity and electric potential of CCL, respectively.

6.2.3.3 Ion exchange membrane

Since there is no reaction in the IEM, the ionic current ($\overrightarrow{\imath_m}$) transport across membrane is given as:[17]

$$\overrightarrow{\imath_m} = -\sigma_m\nabla\phi_m \tag{22}$$

where σ_m and ϕ_m are the ionic conductivity and ionic potential of the membrane, respectively. Furthermore, the conservation of charge in the membrane gives:[17]

$$\nabla\cdot\overrightarrow{\imath_m} = 0 \tag{23}$$

The proton flux ($\overrightarrow{N_{H^+}}$) through the membrane is expressed as:[17]

$$\overrightarrow{N_{H^+}} = \frac{\overrightarrow{\imath_m}}{F} = -\frac{\sigma_m}{F}\nabla\phi_m \tag{24}$$

6.2.3.4 Electrochemical kinetics

In the anode, the interfacial reaction kinetics between the anode surface and liquid e-fuel are governed by the Butler-Volmer equation: [17]

$$i_a = a_{v,a} i_{0,a} (C_{V^{2+}})^{\alpha_{a,a}} (C_{V^{3+}})^{\alpha_{a,c}} \left[exp\left(\frac{\alpha_{a,a}F\eta_a}{RT}\right) - exp\left(-\frac{\alpha_{a,c}F\eta_a}{RT}\right)\right] \tag{25}$$

where $a_{v,a}$ denotes the anode specific area. $\alpha_{a,a}$ and $\alpha_{a,c}$ is the anode anodic and cathodic charge transfer coefficient, respectively. η_a represents the anode overpotential. The reference anodic exchange current density is defined as:[17]

$$i_{0,a} = Fk_a \tag{26}$$

where k_a is the rate constant for anode reaction. While in CCL, Tafel equation is adopted for the calculation of the cathode current density: [26]

$$i_c = a_{v,c} i_{0,c} \left(\frac{C^{ccl}_{O_2}}{C^{ref}_{O_2}}\right)^{\gamma_c} exp\left(\frac{\alpha_c F\eta_c}{RT}\right) \tag{27}$$

$$\gamma_c \begin{cases} 0 & C^{ccl}_{O_2} > C^{ref}_{O_2} \\ 1 & C^{ccl}_{O_2} \le C^{ref}_{O_2} \end{cases} \tag{28}$$

where $a_{v,c}$ denotes the CCL specific area, $i_{0,c}$ represents the reference cathodic exchange current density, α_c denotes cathode charge transfer coefficient and η_c represents cathode overpotential. The reaction order (γ_c) is set to be zero when the oxygen concentration in the CCL ($C^{ccl}_{O_2}$) exceeds the reference concentration ($C^{ref}_{O_2}$). The overpotentials on anode and cathode are represented as:[17]

$$\eta_{a/c} = \emptyset_{a/c,s} - \emptyset_{a/c,l} - E_{a/c} \tag{29}$$

where the anode equilibrium potential (E_a) is defined by the Nernst equation as:[17,21]

$$E_a = E^0_a + \frac{RT}{F} \ln\left(\frac{C_{V^{3+}}}{C_{V^{2+}}}\right) \tag{30}$$

In the meanwhile, the cathode equilibrium potential (E_c) is defined as:

$$E_c = E_c^0 \tag{31}$$

where E_a^0 and E_c^0 is the equilibrium potentials of the anode and cathode half reactions, respectively.

6.2.3.5 Boundary conditions

It is assumed that no inward flux exists at the outer wall of the domain, which can be expressed by:

$$-\vec{n} \cdot \overrightarrow{N_\iota} = 0 \tag{32}$$

In the anode, at the tank/current collector interface, the concentration of species *i* is assumed to be constant, which is expressed as:[26]

$$C_i = C_i^0 \tag{33}$$

where C_i^0 is the initial concentration of species *i*. Similarly, at the interface between the cathode current collector and outside, the oxygen concentration is assumed to be constant as:[26]

$$C_{O_2} = C_{O_2}^0 \tag{34}$$

where $C_{O_2}^0$ is the initial concentration of oxygen.

At the electrode/membrane interfaces, the ionic potential is assumed to be continuous, which can therefore be expressed as:[17]

$$\emptyset_{a/c,l} - \emptyset_m = 0 \tag{35}$$

Moreover, the flux of species is at the anode/membrane interface are given as:[17]

$$\overrightarrow{N_{\iota}} = 0 \ (\mathrm{i} \ \neq H^{+}) \tag{36}$$

$$\overrightarrow{N_{H^{+}}} = \frac{\overrightarrow{\iota_{a,l}}}{F} \tag{37}$$

6.3. Results and Discussion

6.3.1 Model validation

To begin with, the model is first validated by comparing the numerical results with the experimental data. As reported, the experiment was conducted using a home-made passive fuel cell where the e-fuel composed of V^{2+} ions in 3.0 M H_2SO_4 and ambient air are supplied as reactants. Using the same operation parameters, the simulated results show a good agreement with the experimental data under a wide range of e-fuel concentrations from 0.2 to 1.0 M V^{2+} ions as presented in Figure 6.2, which thereby demonstrates the accuracy of the model developed.

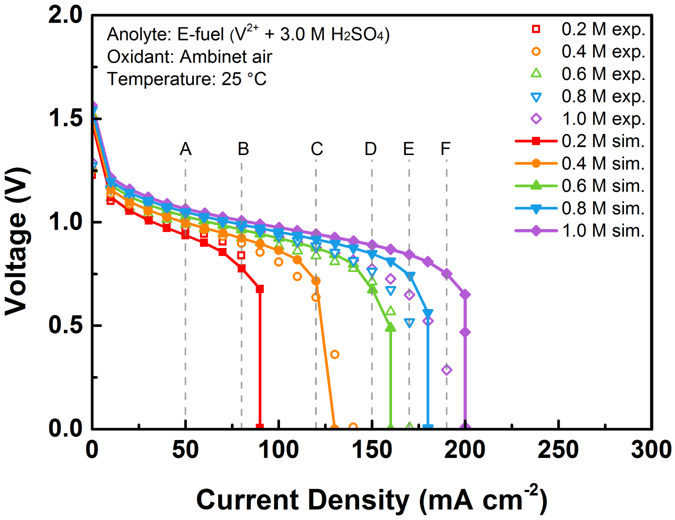

Figure 6.2 Model validation

A further analysis of the simulation results shows that, the cell performance is found to be significantly enhanced with the increment of the e-fuel concentration. Such a change can be traced back to the presence of more V^{2+} ions on the electrode surface (Figure 6.3). When examined under the same current density, the concentration of V^{2+} ions within anode is found to increase with the e-fuel concentration, which enables a lower concentration polarization loss and further ensures a better cell performance. [28]

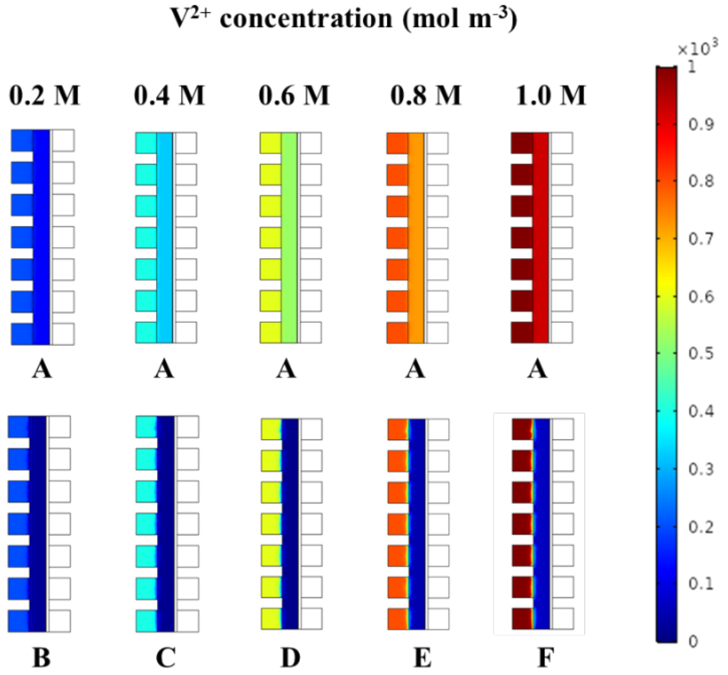

Figure 6.3 Effect of the e-fuel composition on the concentration distribution of V^{2+} ions at the anode

Moreover, the performance boost can be ascribed to the improved mass transport due to the enhanced diffusion process. It is also worthy noticing that irrespective of the e-fuel composition used, when the discharging current density approaches the respective maximum current density, the concentrations of V^{2+} ions in the electrode are all identical and extremely low, which thereby demonstrates the limited mass transport to be the major reason restricting the cell performance. However, undeniably, the deviation in the cell voltage between the model and experiment results becomes relatively larger as the liquid e-fuel concentration gets higher and the discharging current density rises. Such a difference is considered to arise from the assumptions made during modeling. For instance, the assumption of no liquid e-fuel crossover through the membrane ignored the possible mixed overpotential loss induced, while the ignorance of liquid water generated during cell operation disregards the negative impacts associated with the water flooding issue, which therefore make the model to be unable of achieving a perfect fitting with the experimental results.

6.3.2 Effect of the anode thickness

As a key structural parameter, the anode thickness has a great impact on cell performance. On the one hand, a thicker anode could ensure a larger surface area and thereby offer more reactive sites for the electrochemical reaction to lower the polarization loss. On the other hand, the larger anode thickness may lead to a longer path for the species transport and thereby result in a higher mass transfer resistance to limit the cell performance. [29] Therefore, to examine its actual influence, using the model developed, the effects of anode thickness are studied here. As in Figure 6.4, the cell using five different anode thicknesses including 1.0, 1.5, 2.0, 2.5, and 3.0 mm have been simulated, where the cell performance is found to be improved with the anode thickness.

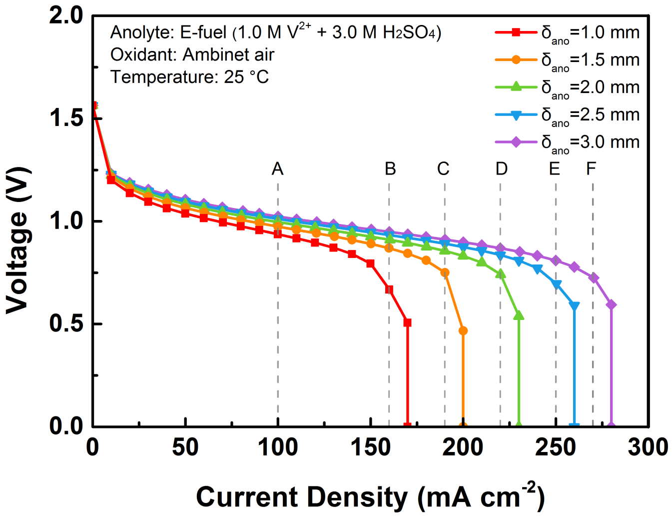

Figure 6.4 Effect of the anode thickness on the cell performance

More detailly, both the cell voltage and maximum current density boost as the anode thickness increases. Notably, the passive fuel cell using 3.0 mm anode exhibits a maximum current density of 280 mA cm^{-2}, which thereby demonstrates the significant role of anode thickness in determining the cell performance.

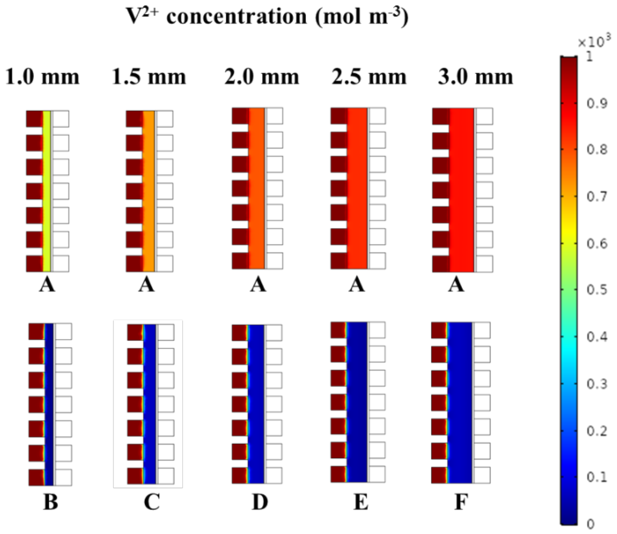

Figure 6.5 Effect of the anode thickness on the concentration distribution of V^{2+} ions at the anode.

Furthermore, it is noted that when examined under the same current density, the cell with a thicker anode is found to present a higher V^{2+} ions concentration distribution (Figure 6.5), which thereby allows the cell to be with better performance by alleviating the concentration polarization loss.

6.3.3 Effect of the anode porosity

The transport of reactive species inside this fuel cell mainly follows diffusion and migration. Therefore, in addition to the anode thickness, the anode porosity is also a key parameter that influences the delivery of electroactive species to the reactive surface and further determines the cell performance. Here, different anode porosities of 0.6, 0.7, 0.8, and 0.9 have been used for numerical studies to analyze its effects (Figure 6.6).

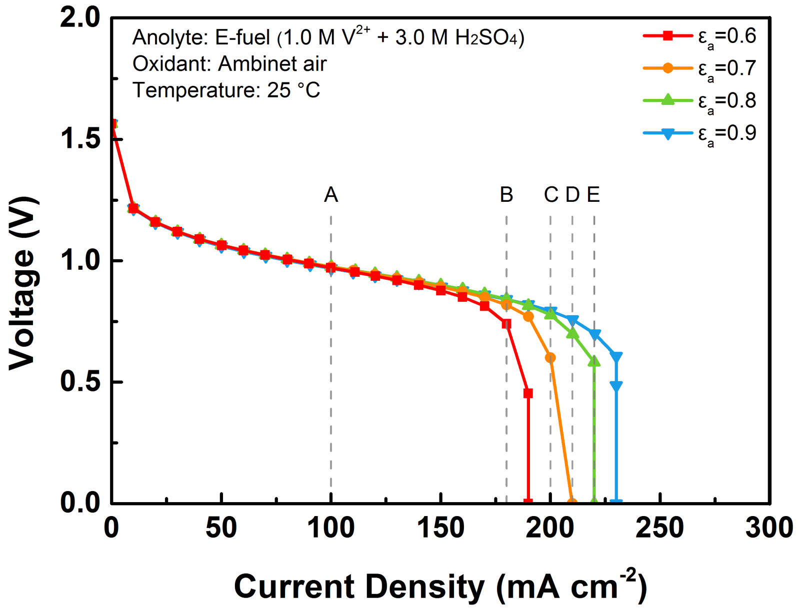

Figure 6.6 Effect of the anode porosity on the cell performance.

It shows that, at the low to middle current density region, the cell voltages using anodes of different porosities are similar. While in contrast, the cell maximum current density is found to increase with the anode porosity, where it rises from 190 mA cm^{-2} (0.6) to 230 mA cm^{-2} (0.9). Such a phenomenon is considered to be attributed to the higher reactants permeability as a result of larger anode porosity, which thereby ensures the electrode surface to be with higher e-fuel concentration. At 180 mA cm^{-2} (Figure 6.7), for example, the concentration of V^{2+} ions in the anode with a porosity of 0.9 is much higher than that with a porosity of 0.6, which therefore justifies the improved reactant mass transport. It is due to this enhanced mass/charge transport inside the fuel cell, a lower concentration polarization loss inside the porous anode is achieved which thereby lowers the overpotentials and enhances the cell performance. [26]

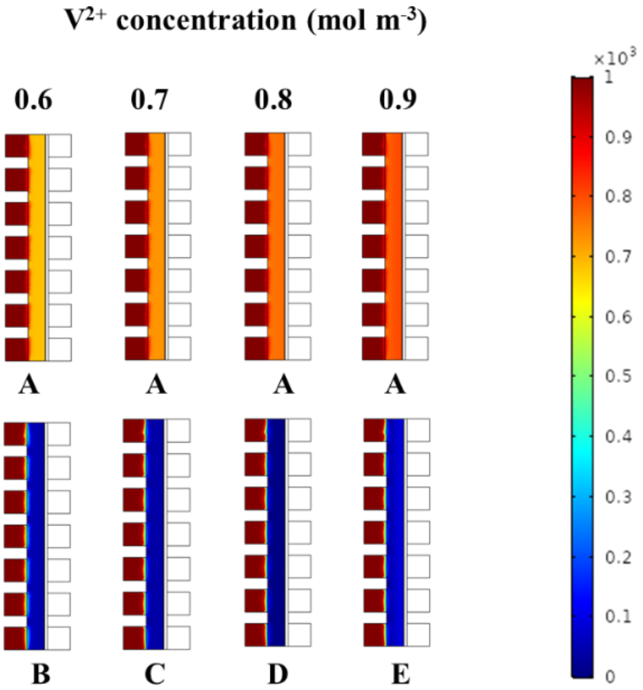

Figure 6.7 Effect of the anode porosity on the concentration distribution of V^{2+} ions at the anode.

6.3.4 Effect of the cathode catalyst layer thickness

Similar to the porous anode, the CCL is also an essential part that not only influences the oxygen transport but also provides reactive sites for the cathode oxygen reduction reaction. Hence, the CCL thickness is also pivotal to the cell performance. In this section, numerical model has been used to study the effects of CCL thickness and the results are shown in Figure 6.8. It suggests that the cell voltage gets higher with the increment of the CCL thickness, which indicates an improved overall cell performance.

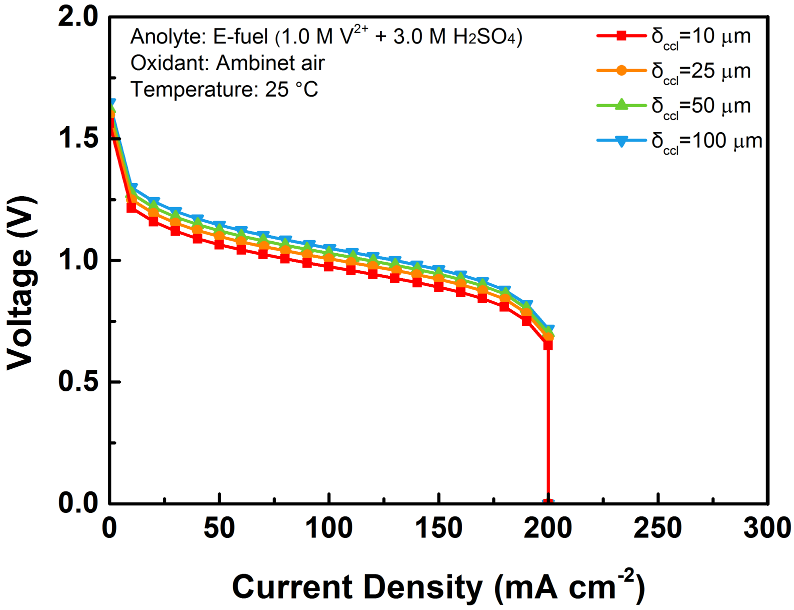

Figure 6.8 Effect of the CCL thickness on the cell performance.

In more detail, for instance, the open-circuit voltage of the cell can be seen to increase to 1.65 V as the cathode catalyst thickness increases 100 μm. Such a boost in cell performance is due to that a thicker CCL can provide more reactive sites and thereby lowers the cathode activation overpotential to achieve a higher cell voltage. [27] However, it is worth mentioning that, the thicker CCL can also impede the oxygen transport due to the lengthened channel and further show a negative effect on the cell performance eventually. [30]

6.3.5 Effect of the oxygen concentration

During cell operation, the oxygen molecules are needed to transport through the CDL to reach the CCL for participating the reactions. Hence, the oxygen concentration is another major factor which is critical for the cell performance. As presented in Figure 6.9, the cell fed with the pure oxygen is found to achieve a higher cell voltage in comparison to its performance when fed with ambient air.

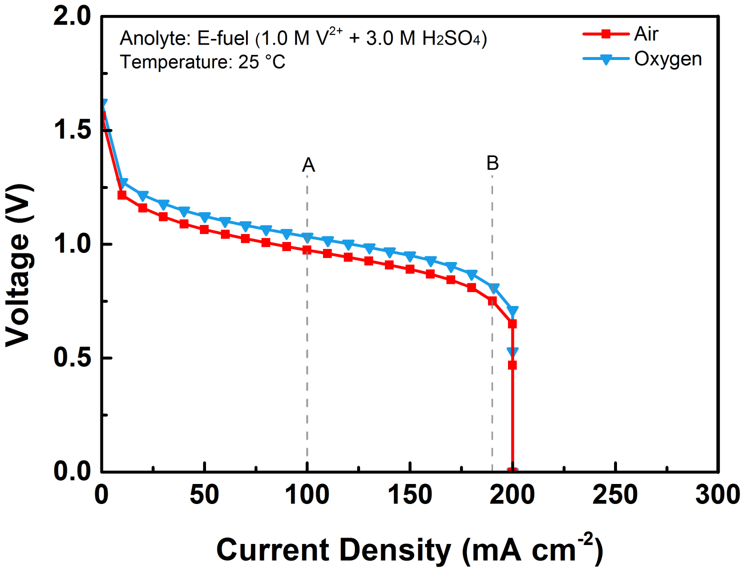

Figure 6.9 Effect of the oxygen concentration on the cell performance.

Such a result is due to the presence of more oxidant molecules within the cathode by using pure oxygen, which thereby leads to a lower activation loss and further lower the cathode overpotential. However, it is also found that, using both the pure oxygen and the ambient air as oxidant, the cell exhibits the same maximum current density. On top of that, as presented in Figure 6.10, even when ambient air is fed, the oxygen concentration gradient from the outlet to the CCL remains small in spite of the discharging current density approaching the maximum current density, which thereby suggests the oxygen concentration be sufficient throughout the whole test. In contrast, at near the maximum current density, the concentration of electroactive species inside porous anode is found to be extremely low. Such a phenomenon thus indicates that the major reason limiting the fuel cell performance arises from the insufficient electroactive species inside the porous anode, while the oxidant due to the relatively high diffusion coefficient of gaseous oxygen is not the primary cause.

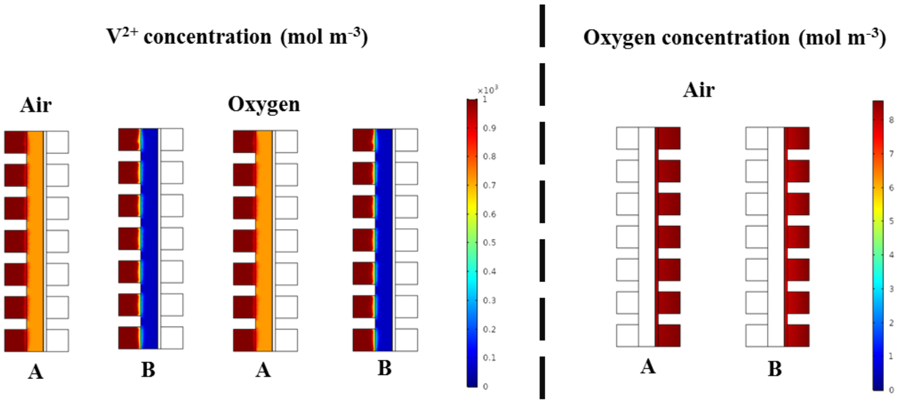

Figure 6.10 Concentration distributions of V^{2+} ions at the anode and oxygen at the cathode.

6.3.6 Effect of the anodic/cathodic exchange current density

Besides various structural parameters, the electrocatalytic activity also affects the system performance. The exchange current density is an indicator of the electrode electrocatalytic activity, which can reflect the electrochemical kinetics of the reactions. [31] Therefore, here, the effects of exchange current density on the cell performance are investigated (Figure 6.11), where their increments are found to boost the cell performance.

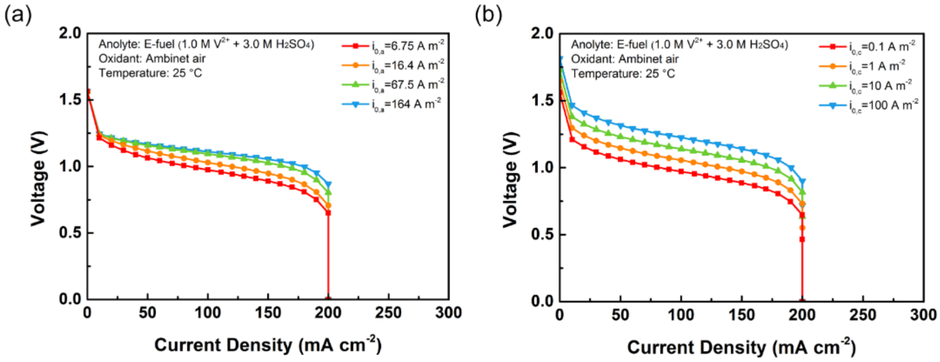

Figure 6.11 Effect of the (a) anodic and (b) cathodic exchange current densities on the cell performance.

For instance, the cell voltage is found to be increased as the cathodic exchange current density rises, demonstrating the importance of cathode catalytic reactivity towards the cell performance. More detailly, at 50 mA cm^{-2}, the cell voltage has been found to elevate to 1.32 V as the cathodic exchange current density increased to 100 A cm^{-2}, proving an improved cell performance due to lowered cathode overpotential. Similar performance enhancement is also found with the increase of anodic exchange current density, where a lower anode overpotential results in a better cell performance. Overall, the highest anodic and cathodic exchange current density are proved to offer the best cell performance. Therefore, it is believed that, increasing the exchange current densities via developing porous anode and cathode catalyst materials with better catalytic reactivity should be regarded as an efficient approach to boost the fuel cell performance.

6.4 Summary

In this work, a 2D transient model for the liquid fuel cell fed with the e-fuel has been developed. This numerical data shows a superior agreement with experimental results, which not only demonstrates its accuracy but also helps to analyze the concentration distribution of reactive species within the cell, showing the limited mass transport of e-fuel to be the major reason restricting the cell performance. In addition, various structural parameters such as the anode thickness, anode porosity, and CCL thickness are also studied, where their increment are all found to boost the cell performance. Meanwhile, the effect of oxygen concentration is also examined, where the usage of oxidant with a higher oxygen concentration is found to be able of achieving a higher cell voltage while the predominant reason limiting the operational current density range is found to be arising from the anode side due to the slow e-fuel transport. Furthermore, the anodic and cathodic exchange current densities are also demonstrated to influence the cell performance due to the significant roles of electrodes catalytic reactivity in influencing the anode and cathode overpotential. In the future, it is believed that with the development of catalysts with excellent electrocatalytic reactivity especially for the oxygen reduction reaction, the cell performance can be further boosted and finally achieve the commercialization of the system.

6.5 References

1. M. K. Singla, P. Nijhawan and A. S. Oberoi, Hydrogen fuel and fuel cell technology for cleaner future: a review, Environmental Science and Pollution Research, 2021, 28, 15607-15626.

2. J. Wang, H. Wang and Y. Fan, Techno-economic challenges of fuel cell commercialization, Engineering, 2018, 4, 352-360.

3. N. Sazali, W. N. Wan Salleh, A. S. Jamaludin and M. N. Mhd Razali, New perspectives on fuel cell technology: A brief review, Membranes, 2020, 10, 99.

4. N. Shaari, S. K. Kamarudin, R. Bahru, S. H. Osman and N. A. I. Md Ishak, Progress and challenges: Review for direct liquid fuel cell, International Journal of Energy Research, 2021, 45, 6644-6688.

5. S. K. Suraparaju, S. K. Natarajan and P. Karthikeyan, 2019.

6. M. E. Scofield, H. Liu and S. S. Wong, A concise guide to sustainable PEMFCs: recent advances in improving both oxygen reduction catalysts and proton exchange membranes, Chemical Society Reviews, 2015, 44, 5836-5860.

7. M. M. Whiston, I. s. M. Lima Azevedo, S. Litster, C. Samaras, K. S. Whitefoot and J. F. Whitacre, Hydrogen storage for fuel cell electric vehicles: Expert elicitation and a levelized cost of driving model, Environmental Science & Technology, 2020, 55, 553-562.

8. B. Ong, S. Kamarudin and S. Basri, Direct liquid fuel cells: A review,

International journal of hydrogen energy, 2017, 42, 10142-10157.

9. P. Kumar, K. Dutta, S. Das and P. P. Kundu, An overview of unsolved deficiencies of direct methanol fuel cell technology: factors and parameters affecting its widespread use, International Journal of Energy Research, 2014, 38, 1367-1390.

10. S. Abdullah, S. Kamarudin, U. Hasran, M. Masdar and W. Daud, Modeling and simulation of a direct ethanol fuel cell: An overview, Journal of Power Sources, 2014, 262, 401-406.

11. S. Basri, S. Kamarudin, W. Daud and Z. Yaakub, Nanocatalyst for direct methanol fuel cell (DMFC), International Journal of Hydrogen Energy, 2010, 35, 7957-7970.

12. X. Shi, X. Huo, Y. Ma, Z. Pan and L. An, Energizing fuel cells with an electrically rechargeable liquid fuel, Cell Reports Physical Science, 2020, 1, 100102.

13. X. Shi, X. Huo, O. C. Esan, L. An and T. Zhao, Performance characteristics of a liquid e-fuel cell, Applied Energy, 2021, 297, 117145.

14. X. Shi, X. Huo, O. C. Esan, Y. Ma, L. An and T. Zhao, A liquid e-fuel cell operating at− 20° C, Journal of Power Sources, 2021, 506, 230198.

15. X. Shi, Y. Dai, O. C. Esan, X. Huo, L. An and T. Zhao, A passive fuel cell fed with an electrically rechargeable liquid fuel, ACS Applied Materials & Interfaces, 2021, 13, 48795-48800.

16. X. Shi, X. Huo, O. C. Esan, Y. Dai, L. An and T. Zhao, Manipulation of

Electrode Composition for Effective Water Management in Fuel Cells Fed with an Electrically Rechargeable Liquid Fuel, ACS Applied Materials & Interfaces.

17. O. C. Esan, X. Shi, X. Su, Y. Dai, L. An and T. Zhao, A computational model of a liquid e-fuel cell, Journal of Power Sources, 2021, 501, 230023.

18. S. Abdullah, S. K. Kamarudin, U. A. Hasran, M. Masdar and W. R. W. Daud, Electrochemical kinetic and mass transfer model for direct ethanol alkaline fuel cell (DEAFC), Journal of Power Sources, 2016, 320, 111-119.

19. K. Oh, H. Yoo, J. Ko, S. Won and H. Ju, Three-dimensional, transient, nonisothermal model of all-vanadium redox flow batteries, Energy, 2015, 81, 3-14.

20. T. T. Pham, F. Mollaamin, M. Monajjemi and C. M. Dang, A review of 2019 fuel cell technologies: modelling and controlling, International Journal of Nanotechnology, 2020, 17, 498-513.

21. K. Knehr, E. Agar, C. Dennison, A. Kalidindi and E. Kumbur, A transient vanadium flow battery model incorporating vanadium crossover and water transport through the membrane, Journal of The Electrochemical Society, 2012, 159, A1446.

22. M. Ismail, D. Ingham, K. Hughes, L. Ma and M. Pourkashanian, Effective diffusivity of polymer electrolyte fuel cell gas diffusion layers: an overview and numerical study, International Journal of Hydrogen Energy, 2015, 40, 10994-11010.

23. X. Zhou, T. Zhao, L. An, Y. Zeng and X. Yan, A vanadium redox flow battery model incorporating the effect of ion concentrations on ion mobility, Applied energy, 2015, 158, 157-166.

24. S. Won, K. Oh and H. Ju, Numerical analysis of vanadium crossover effects in all-vanadium redox flow batteries, Electrochimica acta, 2015, 177, 310-320.

25. H. Sathisha and A. Dalal, Two-Dimensional Unsteady Simulation of All-Vanadium Redox Flow Battery, Journal of Thermal Science and Engineering Applications, 2016, 8.

26. L. An, Z. Chai, L. Zeng, P. Tan and T. Zhao, Mathematical modeling of alkaline direct ethanol fuel cells, international journal of hydrogen energy, 2013, 38, 14067-14075.

27. X. Su, Z. Pan, L. An and Y. Yu, Mathematical modeling of direct formate fuel cells incorporating the effect of ion migration, International Journal of Heat and Mass Transfer, 2021, 164, 120629.

28. Z. Yuan, J. Yang, Y. Zhang and X. Zhang, The optimization of air-breathing micro direct methanol fuel cell using response surface method, Energy, 2015, 80, 340-349.

29. S. Kumar and S. Jayanti, Effect of electrode intrusion on pressure drop and electrochemical performance of an all-vanadium redox flow battery, Journal of Power Sources, 2017, 360, 548-558.

30. S. Matar and H. Liu, Effect of cathode catalyst layer thickness on

methanol cross-over in a DMFC, Electrochimica Acta, 2010, 56, 600-606.

31. Z. Pan, Y. Bi and L. An, Mathematical modeling of direct ethylene glycol fuel cells incorporating the effect of the competitive adsorption, Applied Thermal Engineering, 2019, 147, 1115-1124.

32. H. Meng, A two-phase non-isothermal mixed-domain PEM fuel cell model and its application to two-dimensional simulations, Journal of Power Sources, 2007, 168, 218-228.

33. M. Ghasabehi, M. Ashrafi and M. Shams, Performance analysis of an innovative parallel flow field design of proton exchange membrane fuel cells using multiphysics simulation, Fuel, 2021, 285, 119194.

34. K. Oh, S. Won and H. Ju, A comparative study of species migration and diffusion mechanisms in all-vanadium redox flow batteries, Electrochimica acta, 2015, 181, 238-247.

35. Y. Q. Xue, H. Guo, H. H. Shang, F. Ye and C. F. Ma, Simulation of mass transfer in a passive direct methanol fuel cell cathode with perforated current collector, Energy, 2015, 81, 501-510.

36. E. Ali, H. Kwon, J. Choi, J. Lee, J. Kim and H. Park, A numerical study of electrode thickness and porosity effects in all vanadium redox flow batteries, Journal of Energy Storage, 2020, 28, 101208.

37. S. Zhang, S. Beale, U. Reimer, M. Andersson and W. Lehnert, Polymer electrolyte fuel cell modeling-A comparison of two models with different levels of complexity, International Journal of Hydrogen Energy, 2020, 45,

19761-19777.

38. F. Wandschneider, M. Küttinger, J. Noack, P. Fischer, K. Pinkwart, J. Tübke and H. Nirschl, A coupled-physics model for the vanadium oxygen fuel cell, Journal of Power Sources, 2014, 259, 125-137.

39. R. Chen and T. Zhao, Mathematical modeling of a passive-feed DMFC with heat transfer effect, Journal of Power Sources, 2005, 152, 122-130.

40. W. Cai, S. Li, L. Feng, J. Zhang, D. Song, W. Xing and C. Liu, Transient behavior analysis of a new designed passive direct methanol fuel cell fed with highly concentrated methanol, Journal of Power Sources, 2011, 196, 3781-3789.

Tables:

Table 6-1 Structural parameters.

Symbol	Description	Value	Unit	Ref.
h	Cell height	0.02	m	[15]
w	Cell width	0.02	m	[15]
$\boldsymbol{\delta_{ano}}$	Anode thickness	0.0015	m	[17]
$\boldsymbol{\delta_{m}}$	Membrane thickness	25	μm	[32]
$\boldsymbol{\delta_{cdl}}$	Thickness of CDL	260	μm	[33]
$\boldsymbol{\delta_{ccl}}$	Thickness of CCL	10	μm	[33]
$\boldsymbol{\varepsilon_{a}}$	Porosity of anode	0.68	/	[34]
$\boldsymbol{\varepsilon_{cdl}}$	Porosity of CDL	0.7	/	[35]
$\boldsymbol{\varepsilon_{CCL}}$	Porosity of CCL	0.3	/	[35]
$\boldsymbol{a_{v,a}}$	Specific area of the porous anode	16200	m^{-1}	[36]
$\boldsymbol{a_{v,ccl}}$	Specific area of the CCL	2×10^{5}	m^{-1}	[33]
$\boldsymbol{\sigma_{a}}$	Electrical conductivity of the solid phase	1000	$S\ m^{-1}$	[36]
$\boldsymbol{\sigma_{m}}$	Membrane conductivity	5.5	$S\ m^{-1}$	[26]
$\boldsymbol{\sigma_{cdl,s}}$	Electrical conductivity of CDL	5000	$S\ m^{-1}$	[37]
$\boldsymbol{\sigma_{ccl,s}}$	Electrical conductivity of CCL	2000	$S\ m^{-1}$	[37]
$\boldsymbol{\sigma_{ccl,l}}$	Ionic conductivity of CCL	3.05	$S\ m^{-1}$	[17]

Table 6-2 Properties and parameters.

Symbol	Parameter description	Value	Unit	Ref.
$C^0_{V^{2+}}$	Initial concentration of V^{2+}	1000	mol m^{-3}	[15]
$C^0_{V^{3+}}$	Initial concentration of V^{3+}	200	mol m^{-3}	[15]
$C^0_{H^+}$	Initial concentration of H^+	6000	mol m^{-3}	[15]
$C^0_{O_2,air}$	Initial concentration of O_2 in air	8.584	mol m^{-3}	[26]
$C^0_{O_2,pure}$	Initial concentration of pure O_2	40.876	mol m^{-3}	[26]
$C^{ref}_{O_2}$	Reference concentration of O_2	40.876	mol m^{-3}	[26]
$D_{V^{2+}}$	Diffusion coefficient of V^{2+}	2.4×10^{-10}	m^2 s^{-1}	[38]
$D_{V^{3+}}$	Diffusion coefficient of V^{3+}	2.4×10^{-10}	m^2 s^{-1}	[38]
D_{H^+}	Diffusion coefficient of H^+	9.3×10^{-9}	m^2 s^{-1}	[38]
$D_{SO_4^{2-}}$	Diffusion coefficient of SO_4^{2-}	1.07×10^{-9}	m^2 s^{-1}	[38]
D_{O_2}	Diffusion coefficient of O_2	2.5×10^{-5}	m^2 s^{-1}	[39]

Table 6-3 Electrochemical parameters

Symbol	Description	Value	Unit	Ref.
$\boldsymbol{\alpha_{a,a}}$	Anode anodic charge transfer coefficient	0.4	/	Est.
$\boldsymbol{\alpha_{a,c}}$	Anode cathodic charge transfer coefficient	0.6	/	Est.
$\boldsymbol{\alpha_c}$	Cathode charge transfer coefficient	0.5	/	[26]
$\boldsymbol{k_a}$	Anode reaction rate constant	7×10^{-8}	m s^{-1}	[34]
$\boldsymbol{i_{0,c}}$	Reference cathodic exchange current density	0.11	A m^{-2}	[40]
$\boldsymbol{E_a^0}$	Anode equilibrium potential	-0.26	V	[15]
$\boldsymbol{E_c^0}$	Cathode equilibrium potential	1.23	V	[15]

Nomenclature

$\boldsymbol{a_v}$: Specific area, m^{-1}

$\boldsymbol{C}$: Species concentration, mol m^{-3}

$\boldsymbol{D}$: Diffusion coefficient, m^{2} s^{-1}

$\boldsymbol{E}$: Potential/voltage, V

$\boldsymbol{E^0}$: Equilibrium potential, V

$\boldsymbol{F}$: Faradic constant, A s mol^{-1}

h：Cell height, m

$\boldsymbol{i}$: Current density, A m^{-3}

$\boldsymbol{i_0}$: Reference exchange current density, A m^{-2}

$\boldsymbol{k}$: Reaction rate constant, m s^{-1}

$\vec{\boldsymbol{N}}$: Flux, mol m^{-2} s^{-1}

$\boldsymbol{n}$: Number of participating electrons

$\vec{\boldsymbol{n}}$: Normal vector

$\boldsymbol{R}$: Universal gas constant, J mol^{-1} K^{-1}

$\boldsymbol{S}$: Source term

$\boldsymbol{T}$: Operating temperature, K

$\boldsymbol{t}$: Time, s

$\boldsymbol{u}$: Mobility, mol s kg^{-1}

$\boldsymbol{v}$: Stoichiometric coefficient

w：Cell width, m

z: Valence of ion

Greek

α: Charge transfer coefficient

γ: Reaction order

δ: Thickness, m

ε: Porosity

η: Overpotential, V

σ: Conductivity, S m^{-1}

$\emptyset$: potential, V

Superscripts

0: Initial

ccl: Cathode catalyst layer

eff: Effective

ref: Reference

Subscripts

a: Anode

c: Cathode

ccl: Cathode catalyst layer

cdl: Catalyst diffusion layer

H^+: Proton

i: Species

l: liquid

m: Membrane

O_2: Oxygen

s: solid

SO_4^{2-}: Sulphate ion

V^{2+}: Vanadium (II) ion

V^{3+}: Vanadium (III) ion

Chapter 7 Design and development of a fuel cell stack

7.1 Introduction

Due to the rapid change of climate and imminent energy crisis, the development of renewable energy to replace conventional fossil fuels for power generation has become an imperative option across the globe in the last decades. [1-3] Among the diverse types of renewable power generation systems, the proton exchange membrane fuel cell (PEMFC) using hydrogen and oxygen for electricity production has received an increasing attention. [4,5] The PEMFC possesses a lot of advantages including high efficiencies, zero emission, and fast refueling. [6,7] However, up till now, the production, storage, and transportation of hydrogen still lack effective solutions and hence greatly restrict the commercialization progress of PEMFCs. [8] Alternatively, direct liquid fuel cells (DLFCs) using liquid alcohols have made notable progress and are considered to be a promising power generation candidate. [9-11] However, while the DLFCs cracked the fuel transportation difficulties faced by PEMFCs, by using liquid fuels, their limited power densities are still far from practical application requirements. [11]

Recently, a novel fuel cell using the electrically rechargeable fuel (e-fuel) for power generation has been demonstrated, [12,13] where the e-fuel can be made of a wide range of electroactive materials. As discussed above, by employing vanadium-based e-fuel and oxygen as reactants, we have developed a liquid fuel cell and demonstrated its power generation capability under different operating conditions. [14-18] While the cell is proved to exhibit a substantially improved performance which exceeds other conventional direct alcohol fuel cells, it is found that the water generated at the cathode during the cell operation due to the oxygen reduction reaction could lead to water flooding problem. [19] Such a phenomenon would block the reactive sites at the cathode and further impede the mass transport of reactive species, which thereby could lead to unstable and limited cell performance, especially at low oxidant flow rates. [19]

Hence, in this work, to resolve the water flooding problem in the fuel cell, polytetrafluoroethylene (PTFE) as one of the widely used hydrophobic binding agents, [20,21] has been blended with Nafion and used as the binder for cathode fabrication. It is believed that the PTFE not only helps with the excessive water removal to avoid water flooding problem during the cell operation, but also reduces the cathode production cost due to its cheaper price in comparison to Nafion. [21] Using this blended binder cathode, a fuel cell with an improved cell stability and a higher peak power density in comparison to the cell using pure Nafion for the cathode is demonstrated. Furthermore, a fuel cell stack, using the blended binder cathode, has also been designed and fabricated, of which an excellent performance consistency between its two individual cells is found and is capable of powering a 3D-printed toy car. The significant cell performance and demonstration achieved in this work thus present the fuel cell as a promising device feasible for future real-world applications.

7.2 Experiments

7.2.1. Preparation of the membrane electrode assembly

The home-made MEA used in this work consisted of an anode, a cathode and a Nafion 211 membrane in the middle. The graphite felt (AvCarb G100, Fuel Cell Store) was thermally treated in the air for 5 hours at 500˚C before its usage as the anode to enhance its hydrophilicity and activity. Meanwhile, the Pt/C coated carbon paper cathodes were prepared following the previously reported method. [13] The catalyst ink was first prepared by mixing 60 wt. % Pt/C (Johnson Matthey Co., USA) as catalyst, 5 wt. % Nafion (Fuel Cell Store, USA) and 60 wt. % PTFE (Fuel Cell Store, USA) of different weight ratios as binder, and ethanol as solvent. Afterwards, the ink was sprayed onto the carbon paper to form the catalyst layer with a metallic loading of 2.0 mg cm^{-2}. In this work, by altering the binder compositions during ink preparation, three types of cathodes using 100 wt.% Nafion, 50 wt.% Nafion and 50 wt.% PTFE, and 100 wt.% PTFE were prepared and are denoted as Nafion$_{1.0}$, Nafion$_{0.5}$PTFE$_{0.5}$, and PTFE$_{1.0}$, respectively. The Nafion 211 membrane was pretreated following the reported standard procedure to ensure high proton conductivity and reduce the membrane area resistance, which in turn lowers the ohmic polarization loss of the cell for better performance. [13]

7.2.2. Experimental apparatus

The surface morphologies and hydrophobicity of each fabricated cathode were characterized by the field emission scanning electron microscope (SEM) (Tescan VEGA3, Czechoslovakia) and the contact angle test instrument (Theta Flex, Biolin, Sweden), respectively. The transparent fuel cell was designed and fabricated using a transparent acrylic plate to visualize the water flooding phenomenon at the cathode. During the test, the e-fuel is delivered to the anode by a peristaltic pump at a flow rate of 60 mL min^{-1} from a tank of 120 mL e-fuel, while pure oxygen was fed to the cathode at a flow rate of 10 sccm. The polarization curve tests were conducted using another home-made active [13-15] and passive fuel cells [16] as reported before, both of which have an active area of 2.0*2.0 cm^2. For the active fuel cell, the e-fuel and the oxygen were fed into the cell at 60 mL min^{-1} and 10 sccm, respectively. While for the passive fuel cell, a current collector with an open ratio of 70 % was adopted. [16] Both cells used 20 mL e-fuel during the tests. The stack performance was investigated with a home-made fuel cell stack, which consists of two individual passive fuel cells each with 20 mL e-fuel tank. The active area of each individual cell in the stack was 2.0*4.0 cm^2. The polarization and constant-current discharging tests were carried out using an Arbin BT2000 (Arbin Instrument Inc.). All the experiments were performed under room temperature.

7.3 Results and discussion

7.3.1 Characterization of the blended binder cathodes

Excellent water management has been well recognized as a critical requirement to provide the fuel cell with superior performance. [22,23] On the one hand, good wettability of the electrode plays significant influence towards securing a suitable humidity to ensure adequate membrane hydration level and thereby allowing the ease of ion conduction and a lower ohmic loss. [22] However, it is also required for the electrode to be capable of removing excess liquid water so as to prevent water flooding. [24] Hence, in this work, to achieve a balance between adequate membrane hydration level and cathode water removal ability, the hydrophobic PTFE has been blended with the hydrophilic Nafion during the catalyst ink preparation for the cathode fabrication. [25] Then, to investigate the effects of the binder compositions on the hydrophilicity of the cathode catalyst layer, the water contact angles of the prepared cathodes have also been tested as shown in Figure 7.1.

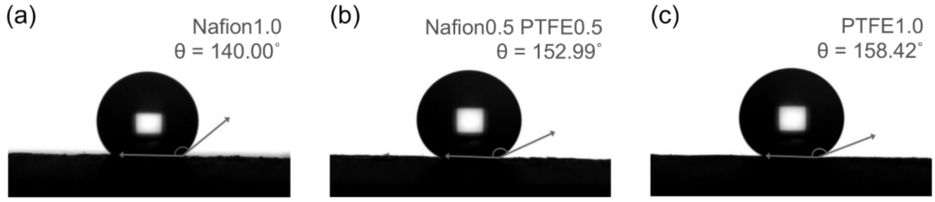

Figure 7.1 Contact angles of (a) $\text{Nafion}_{1.0}$, (b) $\text{Nafion}_{0.5}\text{PTFE}_{0.5}$, and (c) $\text{PTFE}_{1.0}$ cathodes, respectively.

It is observed that, a contact angle of 140.00°, 152.99°, and 158.42° is presented for the $\text{Nafion}_{1.0}$, $\text{Nafion}_{0.5}\text{PTFE}_{0.5}$, and $\text{PTFE}_{1.0}$ cathodes, respectively. Such result thereby suggests that the use of more PTFE during electrode fabrication can result in better hydrophobicity as expected, which thereafter can enhance the water removal ability of the cathode. [24] Furthermore, to examine the effects of the binder composition on the surface morphologies of the cathodes, the SEM images of the three cathodes have also been captured. As presented in Figure 7.2, no obvious morphology change is found, which thereby demonstrates that the addition of PTFE to Nafion does not make any significant influence on the cathode catalyst layer structure.

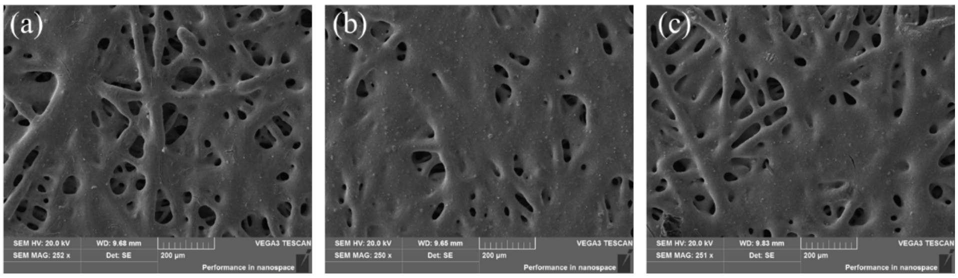

Figure 7.2 Surface morphologies of (a) $\text{Nafion}_{1.0}$, (b) $\text{Nafion}_{0.5}\text{PTFE}_{0.5}$, and (c) $\text{PTFE}_{1.0}$ cathodes, respectively

7.3.2 General performance

In this work, to address the water flooding issue, the hydrophobic PTFE ionomer has been blended with the conventional Nafion resin and used as the binding agents to fabricate a blended binder cathode. The fabricated $\text{Nafion}_{0.5}\text{PTFE}_{0.5}$ cathode using a blended binder of 50% wt. Nafion and 50% wt. PTFE is then examined and the results are as shown in Figures 7.3 (a) and (c). It can be seen that, with the active and passive cell design, a peak power density of 552.68 and 120.90 mW cm^{-2} has been demonstrated, respectively. Such a superior performance not only exceeds that of the pure Nafion/PTFE cathodes as presented below, but also substantially surpasses those of the conventional alcohol fuel cells (Figures 7.3 (b) and (d) and Tables 7-1 and 7-2). [34-56] Thus, with the advantages of achieving a balance between an adequate membrane hydration level and a satisfactory cathode water removal ability as demonstrated in the following sections, this presented blended binder cathode is believed to be a promising candidate for future use. Furthermore, this fuel cell system should be considered as a powerful competitor with promising potential for practical applications.

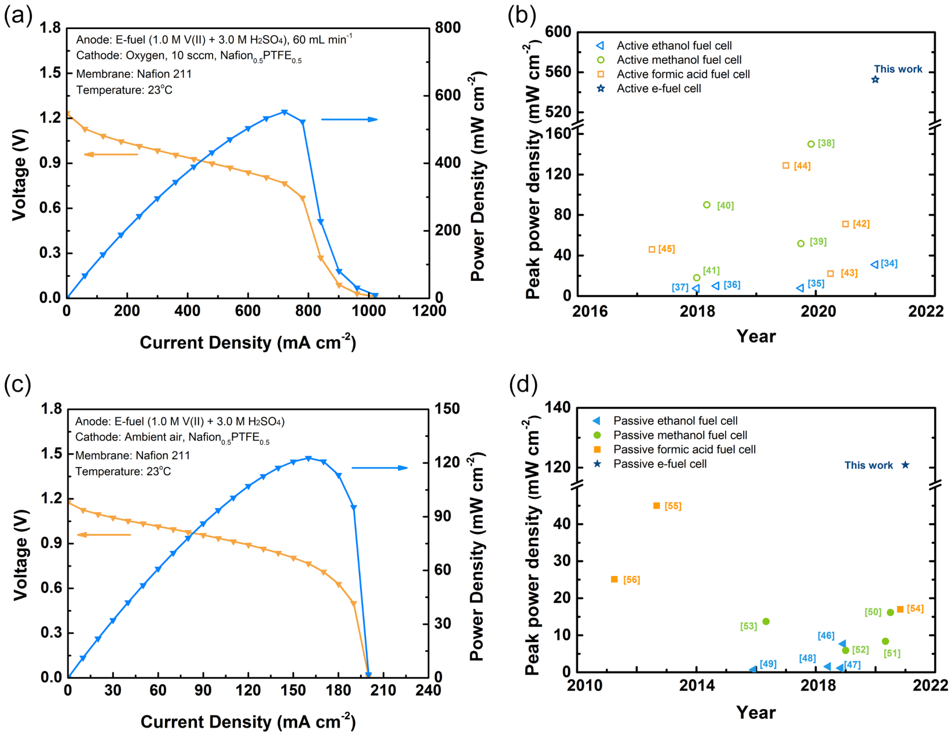

Figure 7.3 General performance and peak power density comparison of (a-b) active and (c-d) passive fuel cells with the data available in the open literature.

7.3.3 Effect of the cathode binder composition

7.3.3.1 Visualization of cathode flow channels

As discussed previously, the water flooding problem at the cathode could severely deteriorate the cell performance. [26] Hence, to evaluate the impact of the prepared cathodes on the cell performance and demonstrate their abilities for water removal, a fuel cell with a transparent cathode flow field has been designed and fabricated (Figure 7.4) to enable the visualizations of the water flooding phenomenon.

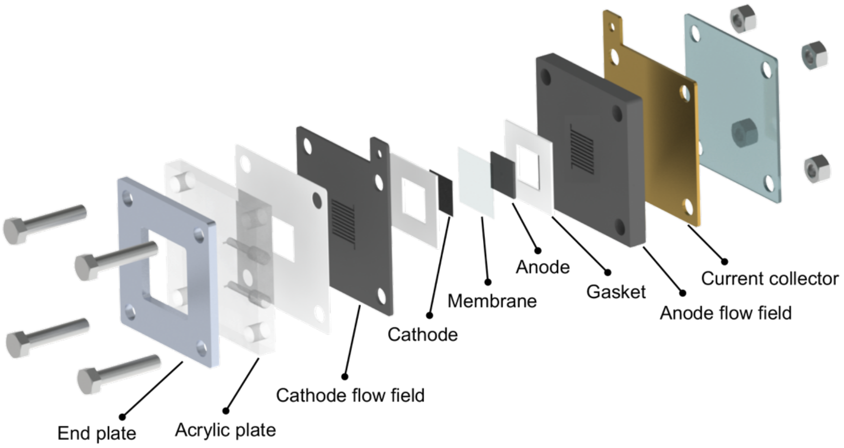

Figure 7.4 Design of a fuel cell with a transparent cathode endplate.

Three cathodes of different binder compositions have been assembled into the cell for the analysis and the results are as shown in Figures 7.5 and 7.6. It can be seen that, when Nafion$_{1.0}$ is tested, the cell can only be operated for ~50 mins before the cell voltage drops to 0.5 V. Such a limited cell performance is mainly caused by the poor water removal ability of the cathode as evidenced in Figure 7.6, where obvious water flooding phenomenon can be seen especially at points A$_4$ and A$_5$. It is attributed to the presence of excessive liquid water which not only covers the active reaction surface, but also impedes the transport of oxygen molecules, resulting in insufficient oxidant feeding and thereby leading to the sudden voltage drop. [27]

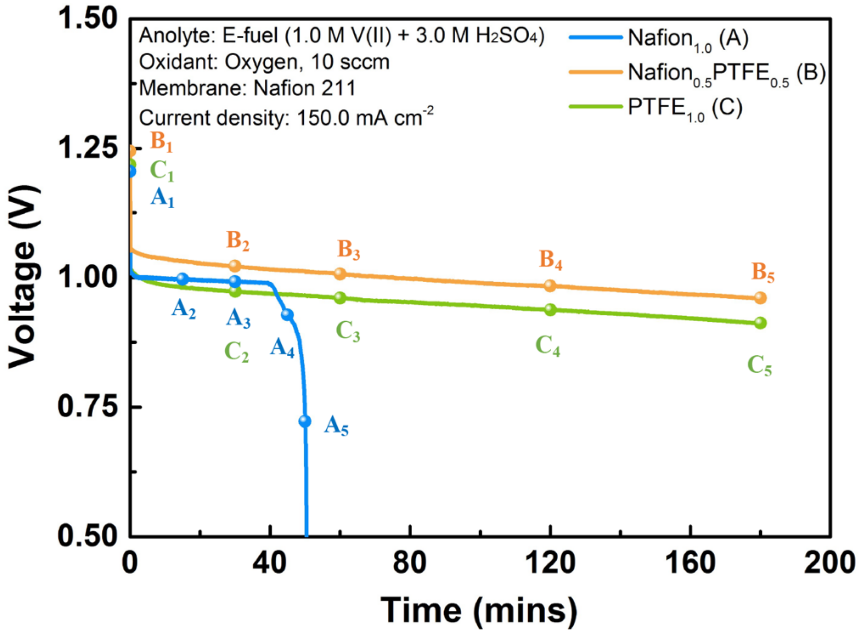

Figure 7.5 Constant-current discharging behaviors of the fuel cell with three cathodes.

In order to further justify this conclusion, immediately after the cell voltage drops to 0.5V the oxygen flow rate has been increased from 10 to 500 sccm and as shown Figure 7.7, a sudden voltage jump can be seen right after the change of the oxygen flow rate and the cell is found to be capable of operating stably thereafter. Such a phenomenon therefore again proves that the limited cell performance using Nafion$_{1.0}$ arises from the poor cathode water removal ability while the high oxygen flow rate can help with the water removal due to the enhanced gas sweeping effect on the liquid water, which thereby alleviate the water flooding issue. [28]

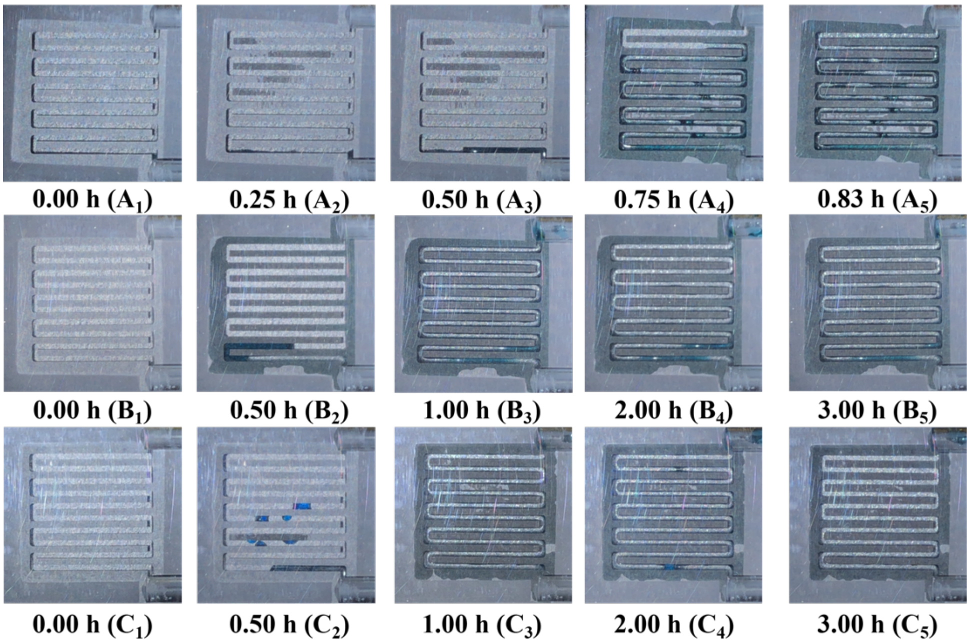
0.00 h (A_1) 0.25 h (A_2) 0.50 h (A_3) 0.75 h (A_4) 0.83 h (A_5)
0.00 h (B_1) 0.50 h (B_2) 1.00 h (B_3) 2.00 h (B_4) 3.00 h (B_5)
0.00 h (C_1) 0.50 h (C_2) 1.00 h (C_3) 2.00 h (C_4) 3.00 h (C_5)

Figure 7.6 Visualization of the flow channel of the fuel cell with three different cathodes.

In contrast, for the fuel cell using $Nafion_{0.5}PTFE_{0.5}$ and $PTFE_{1.0}$ cathodes, the cell is found to be capable of operating stably for three hours under the same operating condition. Furthermore, as shown in the photos (Figure 7.6), the cathode flow channels are also found to be relatively dry during the whole test, which thereby proves the improved water removal ability of the cathode with the addition of PTFE during the electrode fabrication. In summary, water flooding is found to be of critical issue which could influence and limit the cell performance, however, the $Nafion_{0.5}PTFE_{0.5}$ and $PTFE_{1.0}$ cathodes have been proven to ease water removal during the cell operation.

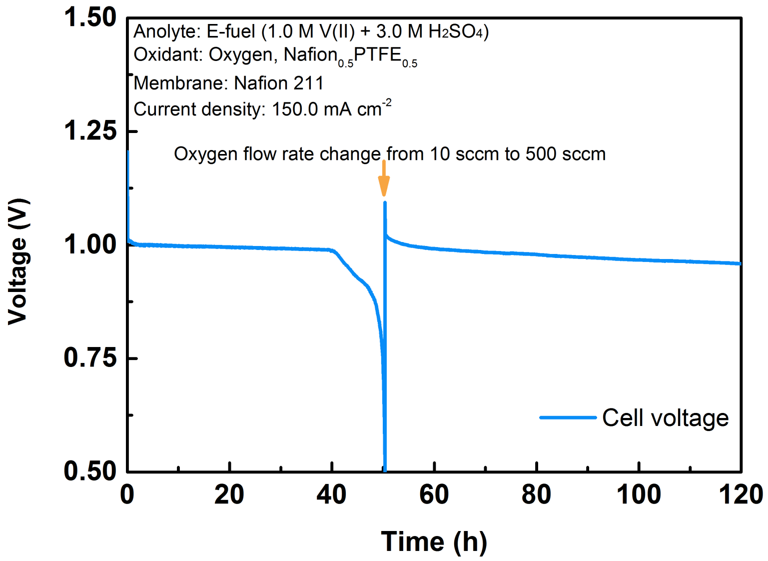

Figure 7.7 Constant-current discharging behavior of the transparent fuel cell assembled with $\text{Nafion}_{1.0}$ cathode.

7.3.3.2 Polarization and power density curves

The wettability of the cathode not only closely relates to its water removal ability but also plays a pivotal role in influencing the membrane hydration level, which further determines the cell performance. [26] Hence, to further evaluate the effects of the binder compositions, the polarization tests have been conducted for cells assembled with three different cathodes, as shown in Figure 7.8. It can be seen that, with both the active (Figures 7.8 (a-b)) and passive (Figures 7.8 (c-d)) fuel cell designs, $\text{Nafion}_{0.5}\text{PTFE}_{0.5}$ cathode is demonstrated to achieve the best cell performance. Such a result is due to that the $\text{Nafion}_{0.5}\text{PTFE}_{0.5}$ cathode can achieve a more balanced membrane hydration level and cathode water removal ability. [29] In comparison to $\text{Nafion}_{0.5}\text{PTFE}_{0.5}$, the $\text{Nafion}_{1.0}$ cathode due to its better wettability can ensure the membrane with higher ionic conductivity and thereby a lower ohmic loss. [19,22] However, it can also result in the difficulty of removing excess water generated during cell operation, which thereafter hampers the oxidant delivery and further deteriorates the cell performance. In contrast, the $PTFE_{1.0}$ cathode, though grants better oxidant delivery, also results in larger ohmic loss and thereby limits the cell performance as it adversely influences the membrane hydration level. [30]

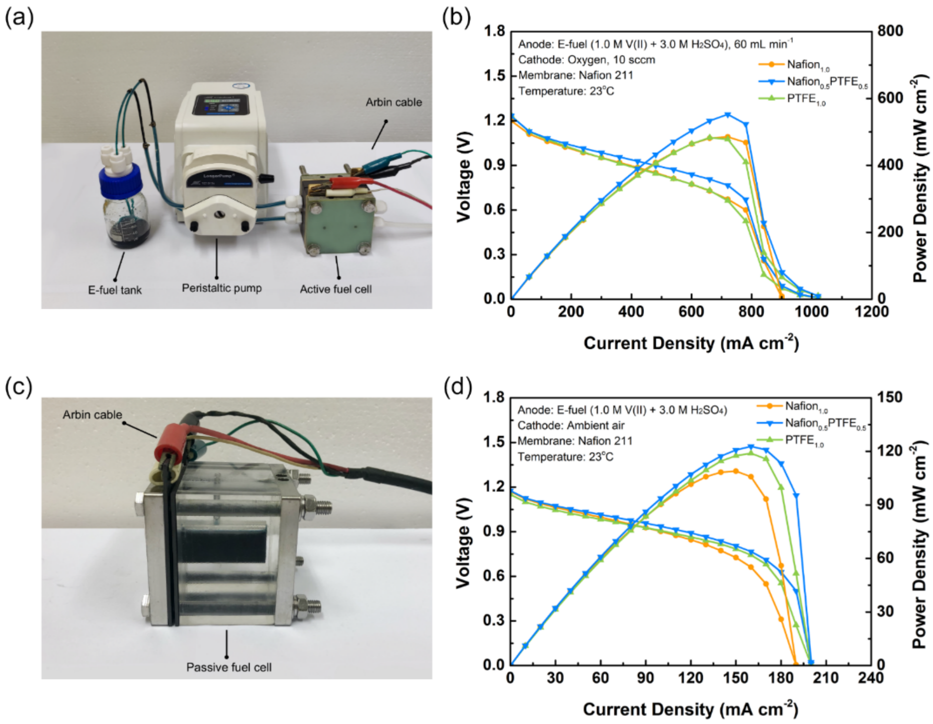

Figure 7.8 Experimental set-up and polarization & power density curves of (a-b) the active and (c-d) the passive fuel cell assembled with three cathodes.

Therefore, overall, the $Nafion_{0.5}PTFE_{0.5}$ cathode with its best performance among all the cathodes tested and lower price than the $Nafion_{1.0}$ cathode, is believed to possess great potential for future applications. It is also worth mentioning that, when tested in the passive fuel cell, the $PTFE_{1.0}$ cathode demonstrate a better and preferable performance in comparison to the

Nafion$_{1.0}$ cathode, which thereby proves the significant effects of water flooding on the passive fuel cell performance.

7.3.4 Lab-scale stack demonstration

7.3.4.1 General performance

As proved in the previous sections, using the Nafion$_{0.5}$PTFE$_{0.5}$ cathode, this presented fuel cell is found to achieve a performance exceeding that of conventional direct liquid fuel cells. Hence, to demonstrate the potential of this fuel cell for real application, in this work, a liquid fuel cell stack consisting of two cells has been designed and fabricated as shown in Figure 7.9.

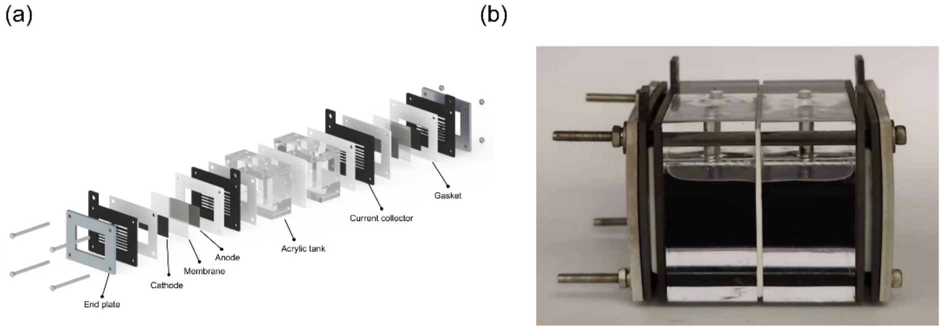

Figure 7.9 (a) Design and (b) fabrication of a fuel cell stack.

To begin with, in order to confirm the performance consistency of individual cell, independent tests have been conducted on both cells under the same operating condition and the results are as presented in Figure 7.10 (a). It is observed that the two individual cells show an excellent performance consistency over the whole tested current range, which thereby proves the good reproducibility of the fabricated cell and justifies its potential for mass production and wide application in future. [9] On top of this, the performance of the whole stack has also been investigated as shown in Figure 7.10 (b). It is found that the whole stack is able to generate an open circuit voltage of 2.37 V, a peak power of 1771.8 mW, and a maximum current of 1441 mA. Such a superior performance, that outperforms the majority of conventional liquid alcohol cell stacks at the same size in the open literatures, [31-33] therefore presents this system to be of great potential in realizing practical applications in the future.

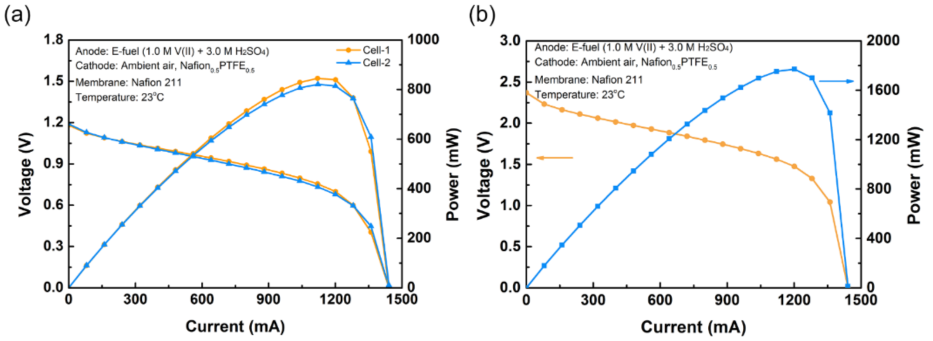

Figure 7.10 (a) The consistency of two individual cells. (b) General performance of this passive fuel cell stack.

7.3.4.2 Stack demonstration for powering a toy car

To further exhibit the application potential of this system, as a prototype demonstration, a home-made toy car powered by the prepared liquid fuel cell stack is designed and then fabricated using the 3D printing technology, as shown in Figures 7.11 (a-b). Before starting, the constant-current discharging test has been first performed for the liquid fuel cell stack and the results are shown in Figure 7.11 (c). During the operation at 20 mA, the stack exhibits a stable operation for ~5 hours indicating the capability of this cell for continuous power generation. Afterwards, when assembled into the toy car, it is found that the stack is capable of generating enough power to drive the toy car stably. Such a result therefore again suggests that this fuel cell stack is of great potential to achieve real application such as powering the future fuel cell electric vehicles. However, it is worth mentioning that, one major limitation of this system is its relatively low energy efficiency of 12.55 %, which may be attributed to the reactive species crossover issue and the undesired side reaction at the anode side as reported before, [16] both of which can result in the loss of fuel capacity. Therefore, it is suggested that future studies are still required to address these problems before realizing the widespread commercialization of this system.

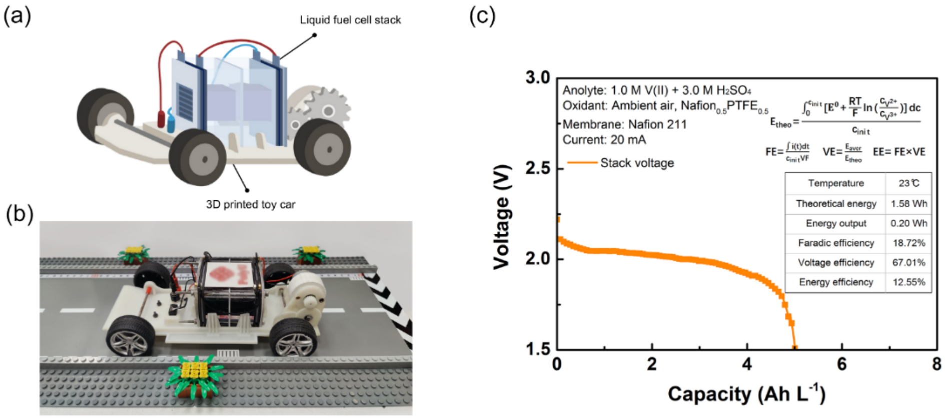

Figure 7.11 (a) Design and (b) fabrication of a fuel cell powered toy car. (c) Constant-current discharging behaviors of the fuel cell stack.

7.4 Summary

In this work, by manipulating the cathode composition, a blended binder PTFE/Nafion cathode is fabricated and examined in an e-fuel cell. It is found that, introducing PTFE during cathode fabrication not only allows a more balanced membrane hydration level and cathode water removal ability, but also reduces the cathode production cost, which thereby grants the cell higher peak power density, better stability, and lower capital cost. Furthermore, to demonstrate the application potential of this system, a liquid fuel cell stack consisting of two individual cells has also been designed and fabricated. This stack is found to exhibit an excellent performance consistency for its two individual cells and is capable of powering a toy car, which therefore presents this system as a promising device feasible for future study and real applications. However, it is also found that the energy efficiency of this stack is still limited, which thereby requires future investigations.

7.5 References

1. J. Liu, Q. Ma, Z. Huang, G. Liu and H. Zhang, Recent Progress in Graphene-based Noble-metal Nanocomposites for Electrocatalytic Applications, Advanced Materials, 2019, 31, 1800696.

2. D. Larcher and J.-M. Tarascon, Towards Greener and More Sustainable Batteries for Electrical Energy Storage, Nature Chemistry, 2015, 7, 19-29.

3. W. Liu, W. Mu, M. Liu, X. Zhang, H. Cai and Y. Deng, Solar-induced Direct Biomass-to-electricity Hybrid Fuel Cell Using Polyoxometalates as Photocatalyst and Charge Carrier, Nature Communications, 2014, 5, 1-8.

4. K. Jiao, J. Xuan, Q. Du, Z. Bao, B. Xie, B. Wang, Y. Zhao, L. Fan, H. Wang and Z. Hou, Designing the Next Generation of Proton-exchange Membrane Fuel Cells, Nature, 2021, 595, 361-369.

5. A. Holewinski, J.-C. Idrobo and S. Linic, High-performance Ag–Co Alloy Catalysts for Electrochemical Oxygen Reduction, Nature Chemistry, 2014, 6, 828-834.

6. T. Tamaki, H. Kuroki, S. Ogura, T. Fuchigami, Y. Kitamoto and T. Yamaguchi, Connected Nanoparticle Catalysts Possessing a Porous, Hollow Capsule Structure as Carbon-free Electrocatalysts for Oxygen Reduction in Polymer Electrolyte Fuel Cells, Energy & Environmental Science, 2015, 8, 3545-3549.

7. X. X. Du, Y. He, X. X. Wang and J. N. Wang, Fine-grained and Fully Ordered Intermetallic PtFe Catalysts with Largely Enhanced Catalytic

Activity and Durability, Energy & Environmental Science, 2016, 9, 2623-2632.

8. Ö. Atlam and G. Dündar, A Practical Equivalent Electrical Circuit Model for Proton Exchange Membrane Fuel Cell (PEMFC) Systems, International Journal of Hydrogen Energy, 2021, 46, 13230-13239.

9. Z. Pan, H. Zhuang, Y. Bi and L. An, A Direct Ethylene Glycol Fuel Cell Stack as Air-independent Power Sources for Underwater and Outer Space Applications, Journal of Power Sources, 2019, 437, 226944.

10. B. Ong, S. Kamarudin and S. Basri, Direct Liquid Fuel Cells: A Review, International Journal of Hydrogen Energy, 2017, 42, 10142-10157.

11. S. Giddey, S. Badwal, A. Kulkarni and C. Munnings, A Comprehensive Review of Direct Carbon Fuel Cell Technology, Progress in Energy and Combustion Science, 2012, 38, 360-399.

12. H. Jiang, L. Wei, X. Fan, J. Xu, W. Shyy and T. Zhao, A Novel Energy Storage System Incorporating Electrically Rechargeable Liquid Fuels as the Storage Medium, Science Bulletin, 2019, 64, 270-280.

13. X. Shi, X. Huo, Y. Ma, Z. Pan and L. An, Energizing Fuel Cells with an Electrically Rechargeable Liquid Fuel, Cell Reports Physical Science, 2020, 1, 100102.

14. X. Shi, X. Huo, O. C. Esan, Y. Ma, L. An and T. Zhao, A Liquid E-fuel Cell Operating at− 20° C, Journal of Power Sources, 2021, 506, 230198.

15. X. Shi, X. Huo, O. C. Esan, L. An and T. Zhao, Performance

Characteristics of a Liquid E-fuel Cell, Applied Energy, 2021, 297, 117145.

16. X. Shi, Y. Dai, O. C. Esan, X. Huo, L. An and T. Zhao, A Passive Fuel Cell Fed with an Electrically Rechargeable Liquid Fuel, ACS Applied Materials & Interfaces, 2021, 13, 48795-48800.

17. O. C. Esan, X. Shi, X. Su, Y. Dai, L. An and T. Zhao, A Computational Model of a Liquid E-fuel Cell, Journal of Power Sources, 2021, 501, 230023.

18. O. C. Esan, X. Shi, Y. Dai, L. An and T. Zhao, Operation of Liquid E-fuel Cells Using Air As Oxidant, Applied Energy, 2022, 311, 118677.

19. P. C. Okonkwo and C. Otor, A Review of Gas Diffusion Layer Properties and Water Management in Proton Exchange Membrane Fuel Cell System, International Journal of Energy Research, 2021, 45, 3780-3800.

20. X. Zhang and P. Shi, Nafion Effect on Dual-bonded Structure Cathode of PEMFC, Electrochemistry Communications, 2006, 8, 1615-1620.

21. Z. Pan, Y. Bi and L. An, A Cost-effective and Chemically Stable Electrode Binder for Alkaline-acid Direct Ethylene Glycol Fuel Cells, Applied Energy, 2020, 258, 114060.

22. P. K. Das, X. Li and Z.-S. Liu, Analysis of Liquid Water Transport in Cathode Catalyst Layer of PEM Fuel Cells, International Journal of Hydrogen Energy, 2010, 35, 2403-2416.

23. J. W. Bae, Y.-H. Cho, Y.-E. Sung, K. Shin and J. Y. Jho, Performance Enhancement of Polymer Electrolyte Membrane Fuel Cell by Employing Line-patterned Nafion Membrane, Journal of Industrial and Engineering

Chemistry, 2012, 18, 876-879.

24. B. Chi, S. Hou, G. Liu, Y. Deng, J. Zeng, H. Song, S. Liao and J. Ren, Tuning Hydrophobic-hydrophilic Balance of Cathode Catalyst Layer to Improve Cell Performance of Proton Exchange Membrane Fuel Cell (PEMFC) by Mixing Polytetrafluoroethylene (PTFE), Electrochimica Acta, 2018, 277, 110-115.

25. K. Lee, S. Ferekh, A. Jo, S. Lee and H. Ju, Effects of Hybrid Catalyst Layer Design on Methanol and Water Transport in a Direct Methanol Fuel Cell, Electrochimica Acta, 2015, 177, 209-216.

26. H. Li, Y. Tang, Z. Wang, Z. Shi, S. Wu, D. Song, J. Zhang, K. Fatih, J. Zhang and H. Wang, A Review of Water Flooding Issues in the Proton Exchange Membrane Fuel Cell, Journal of Power Sources, 2008, 178, 103-117.

27. T. Van Nguyen and G. Lin, Effect of Morphological and Wetting Characteristics of the Gas Diffusion Layers on Electrode Flooding Level in a PEM Fuel Cell, ECS Proceedings Volumes, 2004, 2004, 412.

28. D. Natarajan and T. Van Nguyen, Current Distribution in PEM Fuel Cells. Part 1: Oxygen and Fuel Flow Rate Effects, AIChE Journal, 2005, 51, 2587-2598.

29. G. S. Avcioglu, B. Ficicilar and I. Eroglu, Effect of PTFE Nanoparticles in Catalyst Layer with High Pt Loading on PEM Fuel Cell Performance, International Journal of Hydrogen Energy, 2016, 41, 10010-10020.

30. W. Dai, H. Wang, X.-Z. Yuan, J. Martin, J. Shen, M. Pan and Z. Luo, Measurement of Water Transport Rates across the Gas Diffusion Layer in a Proton Exchange Membrane Fuel Cell, and the Influence of Polytetrafluoroethylene Content and Micro-porous Layer, Journal of Power Sources, 2009, 188, 122-126.

31. Y. S. Li and T. S. Zhao, A Passive Anion-exchange Membrane Direct Ethanol Fuel Cell Stack and its Applications, International journal of hydrogen energy, 2016, 41, 20336-20342.

32. X. Li and A. Faghri, Development of a Direct Methanol Fuel Cell Stack Fed with Pure Methanol, International journal of hydrogen energy, 2012, 37, 14549-14556.

33. D. Chu and R. Jiang, Effect of Operating Conditions on Energy Efficiency for a Small Passive Direct Methanol Fuel Cell, Electrochimica Acta, 2006, 51, 5829-5835.

34 Dresch, M. A., Matos, B. R., Godoi, D. R. M., Linardi, M., Fonseca, F. C., de las Mercedes Villullas, H. and Santiago, E. I. (2021). Advancing direct ethanol fuel cell operation at intermediate temperature by combining Nafion-hybrid electrolyte and well-alloyed PtSn/C electrocatalyst. International Journal of Hydrogen Energy 46, 13252-13264.

35 Choudhary, A. K. and Pramanik, H. (2020). Enhancement of ethanol electrooxidation in half cell and single direct ethanol fuel cell (DEFC) using post-treated polyol synthesized Pt-Ru nano electrocatalysts supported on

HNO3-functionalized acetylene black carbon. International Journal of Hydrogen Energy 45, 574-594.

36 Ma, K.-B., Kwak, D.-H., Han, S.-B., Park, H.-S., Kim, D.-H., Won, J.-E., Kwon, S.-H., Kim, M.-C., Moon, S.-H. and Park, K.-W. (2018). Direct ethanol fuel cells with superior ethanol-tolerant nonprecious metal cathode catalysts for oxygen reduction reaction. ACS Sustainable Chemistry & Engineering 6, 7609-7618.

37 Souza, F. M., Nandenha, J., Batista, B., Oliveira, V., Pinheiro, V., Parreira, L., Neto, A. and Santos, M. (2018). PdxNby electrocatalysts for DEFC in alkaline medium: stability, selectivity and mechanism for EOR. International Journal of Hydrogen Energy 43, 4505-4516.

38 Zhang, X., Xia, Y., Gong, X., Geng, P., Gao, Z. and Wang, Y. (2020). Preparation of sulfonated polysulfone/sulfonated titanium dioxide hybrid membranes for DMFC applications. Journal of Applied Polymer Science 137, 48938.

39 Neelakandan, S., Ramachandran, R., Fang, M. and Wang, L. (2020). Improving the performance of sulfonated polymer membrane by using sulfonic acid functionalized hetero-metallic metal-organic framework for DMFC applications. International Journal of Energy Research 44, 1673-1684.

40 Ranjani, M. and Yoo, D. J. (2018). Sulfonated Fe3O4@ SiO2 nanorods incorporated sPVdF nanocomposite membranes for DMFC applications.

Journal of Membrane Science 555, 497-506.

41 Xu, Q., Zhang, W., Zhao, J., Xing, L., Ma, Q., Xu, L. and Su, H. (2018). Effect of air supply on the performance of an active direct methanol fuel cell (DMFC) fed with neat methanol. International Journal of Green Energy 15, 181-188.

42 Yang, S., Chung, Y., Lee, K.-S. and Kwon, Y. (2020). Enhancements in catalytic activity and duration of PdFe bimetallic catalysts and their use in direct formic acid fuel cells. Journal of Industrial and Engineering Chemistry 90, 351-357.

43 Yan, W., Xiang, Y., Zhang, J., Lu, S. and Jiang, S. P. (2020). Substantially enhanced power output and durability of direct formic acid fuel cells at elevated temperatures. Advanced Sustainable Systems 4, 2000065.

44 Abd Lah Halim, F., Tsujiguchi, T., Osaka, Y. and Kodama, A. (2019). Performance of direct formic acid fuel cell using transition metal-nitrogen-doped carbon nanotubes as cathode catalysts. International Journal of Energy Research 43, 8070-8084.

45 Muthukumar, V. and Chetty, R. (2017). Morphological transformation of electrodeposited Pt and its electrocatalytic activity towards direct formic acid fuel cells. Journal of Applied Electrochemistry 47, 735-745.

46 Zakaria, Z. and Kamarudin, S. (2019). Performance of quaternized poly (vinyl alcohol)-based electrolyte membrane in passive alkaline DEFCs

application: RSM optimization approach. Journal of Applied Polymer Science 136, 47526.

47 Shrivastava, N. K., Chadge, R. B., Ahire, P. and Giri, J. P. (2019). Experimental investigation of a passive direct ethanol fuel cell. Ionics 25, 719-726.

48 Zakaria, Z., Kamarudin, S. K., Timmiati, S. N. and Masdar, M. (2019). New composite membrane poly (vinyl alcohol)/graphene oxide for direct ethanol–proton exchange membrane fuel cell. Journal of Applied Polymer Science 136, 46928.

49 Gharibi, H., Sadeghi, S. and Golmohammadi, F. (2016). Electrooxidation of Ethanol on highly active and stable carbon supported PtSnO2 and its application in passive direct ethanol fuel cell: Effect of tin oxide synthesis method. Electrochimica Acta 190, 1100-1112.

50 Fard, H. F., Khodaverdi, M., Pourfayaz, F. and Ahmadi, M. H. (2020). Application of N-doped carbon nanotube-supported Pt-Ru as electrocatalyst layer in passive direct methanol fuel cell. International Journal of Hydrogen Energy 45, 25307-25316.

51 Zakaria, Z. and Kamarudin, S. K. (2020). Evaluation of Quaternized polyvinyl alcohol/graphene oxide-based membrane towards improving the performance of air-breathing passive direct methanol fuel cell s. International Journal of Energy Research 44, 8988-9000.

52 Munjewar, S. S. and Thombre, S. B. (2019). Effect of current collector

roughness on performance of passive direct methanol fuel cell. Renewable energy 138, 272-283.

53 Ong, B., Kamarudin, S., Masdar, M. and Hasran, U. (2017). Applications of graphene nano-sheets as anode diffusion layers in passive direct methanol fuel cells (DMFC). International Journal of Hydrogen Energy 42, 9252-9261.

54 Nogalska, A., Navarro, A. B. and Garcia-Valls, R. (2020). MEA Preparation for Direct Formate/Formic Acid Fuel Cell—Comparison of Palladium Black and Palladium Supported on Activated Carbon Performance on Power Generation in Passive Fuel Cell. Membranes 10, 355.

55 Cai, W., Liang, L., Zhang, Y., Xing, W. and Liu, C. (2013). Real contribution of formic acid in direct formic acid fuel cell: Investigation of origin and guiding for micro structure design. International journal of hydrogen energy 38, 212-218.

56 Hong, P., Luo, F., Liao, S. and Zeng, J. (2011). Effects of Pt/C, Pd/C and PdPt/C anode catalysts on the performance and stability of air breathing direct formic acid fuel cells. International journal of hydrogen energy 36, 8518-8524.

Table

Table 7-1 Comparison of power densities among various active liquid fuel cells.

Fuel	Year	Anode catalyst	Membrane	Temp	PPD (mW cm^{-2})	Reference
EtOH	2021	PtSn/ C (1.0 mg cm^{-2})	Nafion 115	80 ˚C	31	[34]
	2020	Pt-Ru/C (1.0 mg cm^{-2})	Nafion 117	40 ˚C	7.86	[35]
	2018	PtRu (2.0 mg cm^{-2})	Nafion 117	80 ˚C	10	[36]
	2018	Pd/C (1.0 mg cm^{-2})	Nafion 117	50 ˚C	7.5	[37]
MeOH	2019	Pt-Ru/C (5.0 mg cm^{-2})	Nafion 117	80 ˚C	~ 150	[38]
	2019	Pt-Ru (4.0 mg cm^{-2})	Nafion 212	60 ˚C	51.78	[39]
	2018	Pt-Ru (2.0 mg cm^{-2})	Nafion 117	60 ˚C	~ 90	[40]
	2018	Pt-Ru black (4.0 mg cm^{-2})	Nafion 212	45 ˚C	18	[41]
Formic acid	2020	Pd/C (1.2 mg cm^{-2})	Nafion 117	65 ˚C	71	[42]
	2020	Pt/C (0.5 mg cm^{-2})	Nafion 115	70 ˚C	22	[43]
	2019	Pd/C (2.0 mg cm^{-2})	Nafion 212	60 ˚C	128.9	[44]
	2017	Pt/C (2.0 mg cm^{-2})	Nafion 117	70 ˚C	46	[45]
E-fuel	2021	/	Nafion 211	R.T.	552.68	This work

Table 7-2 Comparison of power densities among various passive liquid fuel cells.

Fuel	Year	Anode catalyst	Membrane	Temp	PPD (mW cm^{-2})	Reference
EtOH	2018	Pt-Ru (4.0 mg cm^{-2})	Nafion 117	30 °C	7.68	[46]
	2018	Pt-Ru (4.0 mg cm^{-2})	Nafion 115	22–25 °C	1.124	[47]
	2018	Pt-Ru (4.0 mg cm^{-2})	Nafion 117	30 °C	1.55	[48]
	2016	Pt/C (4.0 mg cm^{-2})	Nafion 115	R.T.	~0.7	[49]
MeOH	2020	Pt-Ru/C (4.0 mg cm^{-2})	Nafion 117	R.T.	16.133	[50]
	2020	Pt-Ru (2.0 mg cm^{-2})	Nafion 117	30 °C	8.36	[51]
	2019	Pt-Ru/C (4.0 mg cm^{-2})	Nafion 115	25-27 °C	5.865	[52]
	2017	Pt–Ru black (8.0 mg cm^{-2})	Nafion 117	R.T.	13.7	[53]
Formic acid	2020	Pd/C (1.0 mg cm^{-2})	Nafion 117	25	16.99	[54]
	2013	Pd/C (4.0 mg cm^{-2})	Nafion 117	R.T.	45	[55]
	2011	Pd/C (1.0 mg cm^{-2})	Nafion 212	R.T.	25.1	[56]
E-fuel	2021	/	Nafion 211	R.T.	120.90	This work

Chapter 8 Conclusions and future work

Direct liquid fuel cell, a promising power generation device, has attracted great attention with its tremendous superiorities such as high energy density and ease of liquid fuel handling. To achieve the further performance advancement of this technology, this thesis has reported on the experimental and numerical investigations of a liquid fuel cell using a novel electrically rechargeable liquid fuel, and the detailed procedures and finding obtained during the study have been presented in Chapters 2-7. Salient results are summarized as follows:

8.1 Conclusions

i) Fed with a novel liquid e-fuel, a direct liquid fuel cell consists of a catalyst-free graphite-felt anode and a conventional oxygen cathode separated by a proton exchange membrane is developed. The effects of the operating and structural design parameters on the cell performance have been examined. Experimentally, it is found that this liquid fuel cell, operating at 60˚C impressively results in an open-circuit voltage of 1.15 V, a maximum current density of 1980 mA cm^{-2}, a peak power density of 857.0 mW cm^{-2} and an energy efficiency of 41.6 %. These performances are much higher than the conventional alcoholic direct liquid fuel cells and are even comparable to the performance of hydrogen fuel cells reported in the open literature. Moreover, to present its ability for long-term operation, the cell has been refueled for 50 times and achieved a stable operation for ~60 hours, demonstrating its good stability.

ii) To enable the application of the liquid fuel cell for powering portable devices including mobile phones and laptops, a passive liquid fuel cell utilizing the e-fuel for electricity production has been designed and fabricated. Thermodynamically, this passive liquid fuel cell offers a theoretical voltage as high as 1.49 V, which is much higher than those of many conventional liquid alcohol fuel cells. Experimentally, it is found that this passive fuel cell, operating at room temperature, impressively produces an open-circuit voltage of 1.29 V, a maximum current density of 200 mA cm^{-2}, and a peak power density of 116.2 mW cm^{-2}. These performances are much higher than both the conventional passive and active liquid fuel cells reported in the open literature, which hence proves the great potential of this system for future applications. To present the ability of this passive fuel cell for long-term operation, the cell has been refueled 25 times and achieved a stable operation for over 350 hours, demonstrating its good stability. In addition, hydrogen evolution, a side reaction, has also been found to occur at the anode side and been further demonstrated using a transparent cell.

iii) A cold-start-free liquid fuel cell, capable of operating stably under a wide temperature range is designed and fabricated. The fuel cell fed with the liquid e-fuel is found to be able of achieving stable and consistent operation at sub-zero temperatures as low as -20˚C, making it a very promising fuel cell candidate for wide range operating temperature and applications including the electric vehicle industry in the future. To begin with, the effects of operating temperature on the liquid e-fuel, membrane, and electrode are examined. Thereafter, experimentally, this novel liquid fuel cell is found to be able achieving an open-circuit voltage of 1.26 V, a maximum current density of 390 mA cm^{-2}, a peak power density of 76.8 mW cm^{-2}, and an energy efficiency of 25.2 %. Apparently, all these results are higher than the performances achieved by any conventional liquid alcohol fuel cells operating under subzero environment and even at room temperatures. Furthermore, to practically demonstrate the ability of this fuel cell for power generation, the cell along with a set of LEDs has been placed inside a freezing low-temperature chamber, where the LEDs arrangement in form of PolyU (The Hong Kong Polytechnic University) emits a luminous warm yellow light under the freezing environment, proving that the e-fuel cell not only works at -20˚C but can also generate stable electricity to power the LEDs and to brighten the freezing winter during its real application.

iv) For gaining an extensive knowledge of this liquid fuel cell and analyzing the major factors limiting its performance, a two-dimensional transient model has been developed. To begin with, to validate the mathematical model developed, the simulation results have been compared with the experimental data, which shows a good agreement. Thereafter, the effects of various structural parameters such as the anode thickness, anode porosity, and CCL thickness are studied, where their increment are all found to boost the cell performance. Meanwhile, the effect of oxygen concentration is also examined, where the usage of oxidant with a higher oxygen concentration is found to be able of achieving a higher cell voltage while the predominant reason limiting the operational current density range is found to be arising from the anode side due to the slow e-fuel transport. Furthermore, the anodic and cathodic exchange current densities are also demonstrated to influence the cell performance due to the significant roles of electrodes catalytic reactivity in influencing the anode and cathode overpotential.

v) During the operation of this fuel cell, the oxygen reduction reaction at the cathode could lead to water flooding problem, where the accumulated water at the cathode would block the catalyst reactive sites and further impede the mass transfer of reactive species resulting in an unstable cell performance. To address this issue, the hydrophobic PTFE ionomer is blended with the conventional Nafion resin and used as the binding agent to fabricate a blended binder

PTFE/Nafion cathode. It is found that, the blended binder cathodes not only ease the water removal and avoid the water flooding problem, due to its beneficial hydrophobicity, but also help the cell to attain a better performance in comparison to the pure Nafion cathode. Using this blended binder cathode, a fuel cell with an improved cell stability and a higher peak power density in comparison to the cell using pure Nafion for the cathode is demonstrated. Furthermore, a fuel cell stack, using the blended binder cathode, has also been designed and fabricated, of which an excellent performance consistency between its two individual cells is found and is capable of powering a 3D-printed toy car. The significant cell performance and demonstration achieved in this work thus present the fuel cell as a promising device feasible for future real-world applications.

8.2 Future work

Both an active and a passive fuel cell using the liquid e-fuel for power generation have been designed and fabricated, while the effects of various operating conditions on the cell performance have been examined. The application of this fuel cell under sub-zero environment has been addressed by the all-climate fuel cell developed, while a blended binder cathode has been prepared, which not only improved the water management but also demonstrated its application potential inside a fuel cell stack for powering a toy car. There are some future works that will be done:

i) The usage of pure oxygen during cell operation not only increase the system complexity but also restricted its application scenarios. Thus, to enable the application of this fuel cell in air-tight situation such as outer-space and submarine, the hydrogen peroxide will be used to substitute the oxygen.

ii) In addition to the currently used e-fuel containing vanadium ions, the e-fuel can also be attained from other kinds of materials. Hence, novel e-fuels made of other materials will be fabricated to examine their performances and analyze the flexibility of this fuel cell when it is fed with different e-fuels.

iii) As the sluggish oxygen reduction reaction at the cathode side of the fuel cell is the major reason hampering its performance under sub-zero environment, the liquid fuel cell fed with the e-fuels of different compositions at either side will be designed and fabricated to enable a better low-temperature performance.

Appendix I Publications during PhD study at The Hong Kong Polytechnic University

Journal papers:

1. **X. Shi, O.C. Esan, X. Huo, Y. Ma, Z. Pan, L. An, & T.S. Zhao. "Polymer Electrolyte Membranes for Vanadium Redox Flow Batteries: Fundamentals and Applications". *Progress in Energy and Combustion Science*, 2021, 85, 100926.**
2. **X. Shi, X. Huo, O.C. Esan, Y. Dai, L. An, & T.S. Zhao. "Manipulation of Electrode Composition for Effective Water Management in Fuel Cells Fed with an Electrically Rechargeable Liquid Fuel." *ACS Applied Materials & Interfaces*, 2022.**
3. **X. Shi, Y. Dai, O.C. Esan, X. Huo, L. An, & T.S. Zhao. "A Passive Fuel Cell Fed with an Electrically Rechargeable Liquid Fuel." *ACS Applied Materials & Interfaces*, 2022, 13.41: 48795-4880.**
4. **X. Shi, X. Huo, O.C. Esan, L. An, & T.S. Zhao. "Performance characteristics of a liquid e-fuel cell". *Applied Energy*, 2021, 297, 117145.**
5. **X. Shi, X. Huo, O.C. Esan, Y. Ma, L. An, & T.S. Zhao. "A liquid e-fuel cell operating at −20 °C". *Journal of Power Sources*, 2021, 506, 230198.**

6. **O.C. Esan†, X. Shi†, X. Su, Y. Dai, L. An, & T.S. Zhao. "A computational model of a liquid e-fuel cell". *Journal of Power Sources*, 2021, 501, 230023. (Co-first author)**
7. **X. Shi, X. Huo, Y. Ma, Z. Pan, & L. An. "Energizing Fuel Cells with an Electrically Rechargeable Liquid Fuel". *Cell Reports Physical Science*, 2020, 1(7), 100102. (Front Cover)**
8. **X. Shi, Y. Ma, X. Huo, O.C. Esan, & L. An. "Nafion membranes for e-fuel cell applications". *International Journal of Green Energy*, 2021, 1-7.**

Book chapter

1. **X. Shi, Y. Bi, O.C. Esan, L. An. "Membranes for vanadium-air redox flow batteries". *60 Years of the Loeb-Sourirajan Membrane*. Elsevier, 2022, 155-175.**